PHYSICS, MODELING AND DESIGN OF NONLINEAR ELECTROABSORPTION MODULATORS

PHYSICS, MODELING AND DESIGN OF NONLINEAR ELECTROABSORPTION MODULATORS

By

YU CHEN, B. Sc., M. Sc.

A Thesis

Submitted to the School of Graduate Studies

in Partial Fulfillment of the Requirements

for the Degree

Doctor of Philosophy

McMaster University

DOCTOR OF PHILOSOPHY (2007) McMaster University

(Electrical and Computer Engineering) Hamilton, Ontario

TITLE: **Physics, Modeling and Design of Nonlinear Electro-absorption Modulators**

AUTHOR: Yu Chen

B. Sc.

(Nankai University, 1986)

M. Sc.

(University of Waterloo, 1995)

SUPERVISOR: Dr. Wei-Ping Huang

Professor, Department of Electrical and Computer Engineering

B. Sc. (Shandong University)

M. Sc. (University of Science and Technology of China)

Ph. D. (Massachusetts Institute of Technology)

NUMBER OF PAGES: xviii, 180

Abstract

Wavelength division multiplexing (WDM) is the key technology of the current generation fiber-optics network. To build agile and intelligent next generation optical networks, optical wavelength conversion and signal regeneration are crucial new functions under intense research and development. These new functions call for innovative, low cost and high performance optoelectronic devices. One of such enabling devices is quantum-well electroabsorption modulators (EAM) that are appealing in terms of structural simplicity and low noise and are potentially advantageous on high-speed operation and low power consumption. The goal of this thesis is to systematically study EAM for optical signal functions in optical networks from various perspectives, including fundamental device physics, comprehensive models, innovative design, and experimental prototyping.

After the first chapter of introduction, Chapter 2 and 3 are devoted to device models. In Chapter 2, a self-consistent and physics-based model has been developed for two key nonlinear optical mechanisms in quantum-well EAM: exciton saturation and electric field screening. Presented in Chapter 3 is a simplified but efficient model for EAM with a feature of handling strong electric field.

Next, the fundamental physics relevant to nonlinear EAM are studied in Chapter 4 and 5. Exciton state mixing effects on intersubband transitions in quantum well have been investigated in Chapter 4 and a drastic different picture from that of the previous studies has been revealed. Studies have also been done in Chapter 5 on valence band mixing effects in exciton capture and escape in quantum well structures. And it is found that much faster capture and escape processes can be resulted from the band mixing effects.

Then, the two key design issues of nonlinear EAM have been addressed. In Chapter 6, different saturation dynamics of electrons and holes in quantum wells have been thoroughly analyzed and utilized to achieve the best compromise between high-speed and low power consumption of EAM in optical wavelength conversion and signal regeneration. In Chapter 7, the polarization issue of transverse electric (TE) mode and transverse magnetic (TM) mode is addressed from two different perspectives: design for the most effective optical saturation by using TM mode absorption and design for TE and TM polarization insensitive operation.

Finally, Chapter 8 presents the results of experimental prototyping on the design concept to enhance exciton absorption saturation using light-hole excitation through TM optical mode.

Acknowledgements

I would like to express my sincere gratitude to my supervisor, Prof. Wei-Ping Huang, for his constant guidance, support and encouragement throughout the course of my Ph.D program. I also would like to extend my many thanks to Dr. Xun Li, Dr. Shiva Kumar and Dr. Chang-Qing Xu, members of my supervisory committee, for their continuous interest, advices and suggestions.

I am appreciative to Dr. Seyed M. Sadeghi for numerous discussions. I am also grateful to Prof. John Cartledge and Dr. David Krause in Queens' University and Mr. Maxime Poirier and Mr. Don Deptuck at Canadian Photonics Fabrication Center, for their collaborations in fabricating and characterizing EA modulators. In addition, I am indebted to the graduate assistant Ms. Cheryl Gies for her various help during all my years at McMaster.

I would also like to thank Natural Science Engineering Research Council of Canada (NSERC) and McMaster University for financial support.

My special thanks to my wife, Renyu Zhang, for her love, support and understanding. I am also grateful to my daughter, Abigail Xi Chen, for the joy and the laughter she brings in the intense and stressful moments. Finally, I am indebted to my parents and other family members for their lifelong supports and encouragements.

Contents

List of Figures

List of Tables

List of Symbols and Acronyms

Symbol : Description

e : electron charge

m_0 : free electron mass

m_e : effective mass of conduction band electrons

m_h : effective mass of valance band holes

m_r : reduced mass of electron-hole pairs

ε_0 : permittivity of vacuum

n_r : group index

λ : wavelength

k : in-plane crystal vector

c : light velocity in vacuum

α : attenuation constant

α_0 : attenuation constant without saturation

F : electric field

$\mathbf{r}_e$: three dimensional electron coordinate

$\mathbf{r}_h$: three dimensional hole coordinate

z : the growth direction

z_e : electron coordinate along the growth direction

z_h : hole coordinate along the growth direction

$\psi(\mathbf{r_e})$: three dimensional electron wave function

$\psi(\mathbf{r_h})$: three dimensional hole wave function

$f(z_e)$: electron envelop wave function along the growth direction

$g(z_h)$: hole envelop wave function along the growth direction

σ : electron spin index

ν : hole spin index

$\Psi(\mathbf{r_e}, \mathbf{r_h})$: three dimensional exciton wave function

$\boldsymbol{\rho}$: in-plane coordinates of exciton relative movement

$\mathbf{k}$: in-plane momentum of exciton relative movement

$\phi(\boldsymbol{\rho})$: in-plane exciton envelop wave function in real space

$\phi(\mathbf{k})$: in-plane exciton envelop wave function in momentum space

ξ : the first quantum number of exciton

β : the second quantum number of exciton

u_c : Bloch function of conduction band electrons

u_v : Bloch function of valence band holes

$\hat{\mathbf{e}}$: polarization unit vector

$\mathbf{P_{cv}}$: momentum matrix elements of bulk semiconductor

L_W : quantum well width

n : three dimensional electron density

p : three dimensional hole density

J_n : electron current density

J_p : hole current density

n_{2D} : two dimensional electron density

p_{2D} : two dimensional hole density

τ_{cap}^{n} : electron capture time

τ_{esc}^{n} : electron escape time

τ_{cap}^{p} : hole capture time

τ_{esc}^{p} : hole escape time

Acronym : Description

2D : two dimensional

3D : three dimensional

ABC : absorbing boundary condition

EA : electroabsorption

EAM : electroabsorption modulators

FDM : finite-difference method

FEM : finite element method

HH : heavy hole

IBC : infinite barrier boundary condition

IST : inter-subband transitions

LH : light hole

LO : longitudinal optical phonons

MQW : multiple quantum wells

PIN : diode with intrinsic region between P and N regions

PI IST : photo-induced intersubband transition

PML : perfectly matched layer

QCSE : quantum-confined Stark effects

QW : quantum well

SCH : separate confinement hetero-structure

SOA : semiconductor optical amplifier

SQW : single quantum well

TE : transverse electric

TM : transverse magnetic

TMM : transfer matrix method

WDM : wavelength division multiplexing

Chapter 1

Introduction

1.1 Research Background

Semiconductor quantum well (QW) and other low-dimensional quantum structures have been and will continue to be of great interest, both from physics and engineering standpoints [1],[2]. The quantization of electrons states in such structures brings out many physics different from those in bulk semiconductors. And the control of the material compositions and the geometric dimensions enabled by advancing technology allows the engineering of many fundamental properties of semiconductor materials and devices. These structures provide a platform to explore numerous ingenious designs of semiconductor devices for various important applications. One example is quantum well electroabsorption (EA) modulators that are used for optical wavelength convention and signal regeneration in optical networks [3],[4]. Electroabsorption modulators (EAM) in such applications, embodying the richness of physics and the ever-expanding

frontier of applications of semiconductor quantum structures, form the central theme of this thesis.

The quantum-well EA modulators work on quantum-confined Stark effects (QCSE). The energy level in quantum wells can be easily adjusted by electric field. As a result, the optical absorption can be readily controlled by applied bias. This effect has been successfully utilized in signal modulation in optical communication [5]. In signal modulation, the optical intensity inside EA modulators is usually low. When the optical intensity is high, various nonlinear mechanisms will manifest, most noticeably, exciton saturation and electric field screening. Through these mechanisms, the optical absorption of EA modulators will saturate, which enable EAM work as nonlinear devices for optical signal processing. Our main task will be to systematically investigate the various optical saturation mechanisms and how they can be enhanced for optical signal processing, especially, in the applications of optical wavelength conversion and signal regeneration in optical networks [6],[7].

Optical wavelength conversion and signal regeneration are the new functions under intense research and development for next generation optical networks. Fiber optics communication has witnessed tremendous progress in recent years. In particular, wavelength-division-multiplex (WDM) systems have become the backbone of the ever-growing internet. WDM systems opened up the avenue to utilize the wavelength resource inherited in optic fibers. At the same

time, they also pose the challenge how to agilely and effectively manage the wavelength resource in the networks. One of the solutions is to introduce optical wavelength conversion and signal regeneration at the network nodes, making the network more agile and less dependent on costly optic-electronic-optic conversion. Comparing to other alternative components in these applications, an EAM based component has the appeal of structural simplicity, requiring no interferometer configuration as in semiconductor optical amplifiers (SOA) [8] or loop mirror as in nonlinear optic fibers [9]. In addition, it has much less noise and potentially advantageous in high-speed operation and low power consumption. However, how to realize the high speed and low power operation remains a challenge that calls for thorough understanding and innovative design of EA modulators.

1.2 Thesis Objectives

1.2.1 Comprehensive Models

The performance of quantum-well EAM as optical signal processors is critically dependent on the optical absorption saturation. The two most important saturation mechanisms are exciton saturation and electric field screening. Extensive research has been done on these two saturation mechanisms both theoretically and experimentally. On the theoretical side, exciton saturation has been described by

phase-space filling theory [10]-[13] and the electric field screening by Poisson equation [14] or plus drift-diffusion equations [15]. However, the previous research either focused on one mechanism of saturation or integrated the two interrelated saturation processes in a phenomenological manner [16]. As we will show in this thesis, in order to model and design the nonlinear EAM for high speed application, only physics-based models that integrate both exciton saturation and electric field screening in a self-consistent manner will be adequate [17].

Comprehensive models are required not only in the sense of the true integration of the models of two saturation processes. For each saturation mechanism, a comprehensive treatment is also required. For instance, to model exciton saturation, we need to know electron states, exciton states, and optical absorption. In our treatment of these subjects, we will take into full account of advanced physics such as valence band mixing and exciton state mixing. The models less than this complexity, as we will show, may miss the physics that have significant impacts on some critical device characteristics [18],[19].

To develop a comprehensive model for nonlinear EAM, many numerical issues also need to be addressed. The electron states of quantum well under electric field will become quasi-bound states. The solution for leaky wave remains an intrigue mathematical and numerical problem [20]. The exciton equation in momentum space is a singular integral equation, how to remove the singularity

and speed up the solution of equation with multi-fold integration is also a challenge [21],[22]. The drift-diffusion equation of carrier transport is well-known nonlinear problem that is difficult to solve, especially, for the structures with high hetero-junction barriers as those we deal with in quantum well EAM [23]. Finally, the development of model with this complexity itself is quite an engineering endeavor.

1.2.2 Device Physics

First of all, we will systematically study the various physics processes related to optical absorption saturation in the context of their application in optical network. We will study how fast photons can be absorbed by electrons/excitons, how many electrons/excitons can be accommodated in a given space, how long electrons/ excitons can stay in quantum wells, and how the electrons and holes both inside and outside quantum wells screen the electric field in well regions, and most importantly, how these processes influence the characteristics of EA modulators as wavelength converters. Our systematical approach and comprehensive models enable us to study the device physics that have not been thoroughly studied before. For instance, we will study the different saturation dynamics of electron and holes that are important in optimizing EAM design for high-speed operations [17].

Secondly, we will investigate new device physics. It has been recently proposed to use intersubband transitions for wavelength conversion. We will

show that the exciton state mixing effects in intersubband transitions can give a drastically different picture of intersubband transitions from what is previously perceived [18]. Carrier capture and escape in quantum wells will significantly influence the speed and the nonlinearity properties of EAM and other critical characteristics of optoelectronic devices such as laser diodes, photo-detector and solar cells. We will study the excitonic nature of the capture and escape processes and will show that valence band mixing effects can result in much faster exciton capture/escape than what the existing parabolic model predicts [19].

1.2.3 Nonlinear EAM design

The key to design EAM for signal processing applications is to enhance the optical nonlinearity through all possible means. We will explore the possibility to use the exciton absorption associated with light-hole and TM mode instead of the conventional exciton absorption associated with heavy-hole and TE mode. Based on so-called effective mass reversal, the light-hole has heavier in-plane effective mass and heavy-hole has lighter in-plane effective mass, our analysis will show that EAM based LH excitonic absorption of TM mode exhibits much lower optical saturation intensity, which means they will work at much lower optical power [24].

As low optical saturation intensity is often inversely related to operation speed, careful design has to be carried out to reach the best compromise possible.

Our simulation shows the electrons and holes in EAM in commonly-used InGaAs/InGaAsP quantum wells have different saturation dynamics that impair high-speed operation because of the long tail in its response to optical impulse. Also, in such QW structure, holes accommodate more in quantum well than electrons do. Since electrons are easier to get saturated, the more electron concentration will be desired. To overcome these two drawbacks, we propose to use InGaAs/InAlGaAs quantum wells to obtain more favorable dynamics and to achieve low optical saturation intensity without severe sacrifice of the operation speed [17].

We will also design EAM for TE/TM insensitive operation. TE and TM polarization insensitive operation will be considered including valance band mixing and exciton state mixing. The quantum-well structures in which the first HH subband and the first LH subband are well aligned will be studied and designed for TE/TM insensitive operation in optical network applications.

1.2.4 Experimental prototyping of EAM

Through the collaboration with CPFC (Canadian Photonics Fabrication Center) and Prof. Cartledge's group at Queens' University, we have fabricated and characterized the EAM devices based on the design concepts developed in this thesis. We will report the experimental results in the end.

1.3 Outline of the Thesis

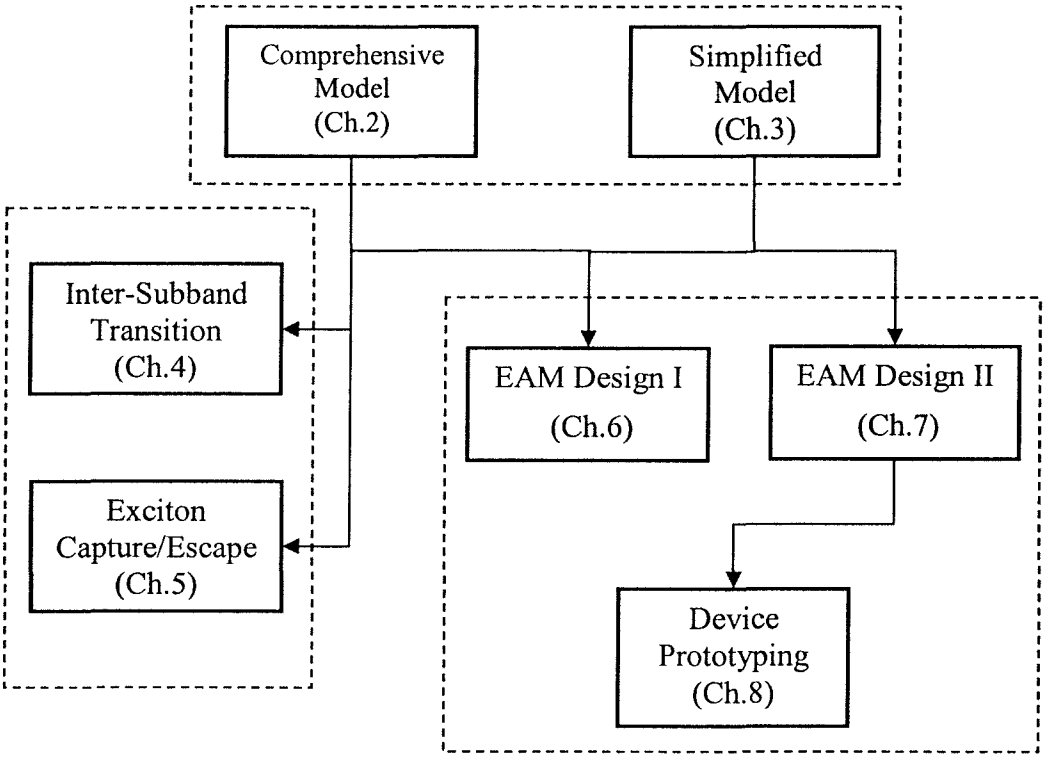

Figure 1-1 Block diagram of the outline of the thesis

This thesis contains nine chapters altogether. Figure 1-1 shows the block diagram how the chapters are connected and organized. The first chapter of introduction and the last chapter of summary are not on the diagram. The chapters in Figure 1-1 can be categorized as three groups as the dashed blocks indicate: modeling, physics and design.

Chapter 2 and Chapter 3 are devoted to the modeling of the EAM. Chapter 2 describes the physics models of nonlinear EAM including both exciton saturation and electric field screening. Some fundamental materials are included to establish the conceptual frameworks of solid-state theory and carrier transport theory, which are the foundation of our theoretical models. Chapter 3 can be considered as a scale-down version of EAM model, which is preferred in the applications where simplicity and efficiency are desired. In Chapter 3 we have also addressed the challenge of modeling strongly tilted quantum well. Perfectly-matched-layer (PML) has been used to model the leaky wave of electrons in quantum wells with shallow barrier potential or under strong electric field.

Chapter 4 and Chapter 5 study two physics effects related to nonlinear EA modulators. In Chapter 4 we investigate the exciton state mixing effects on intersubband transitions in un-doped quantum well structures. Intersubband transitions coupled with interband transition in such structures have been conceived as a new means of wavelength conversion. In Chapter 5 we study exciton capture into and escape out of shallow quantum wells, which can have significant influence over the saturation and other characteristics of the devices based on such structures.

In the last three chapters, we deal with various issues regarding the design and prototyping of nonlinear EA modulators. In Chapter 6 we have carried out systematic simulation and optimization of EA modulators for high-speed network

application. In Chapter 7 we have addressed the issue of TE and TM polarization. Finally, in Chapter 8 we have reported the fabrication and measurement results of the EAM that prototypes some of our design concepts.

Chapter 2

Optical Absorption Saturation in Quantum Wells

In this chapter, we will describe the comprehensive models for the optical absorption saturation in quantum wells. In order to present a complete picture, the basic conceptual frameworks of solid-state theory and carrier transport theory are first laid out as the foundations of our saturation models. And then we go on to describe the saturation model of exciton absorption based on solid-state theory [11],[26] and the saturation model of electric field screening based on the drift-diffusion transport theory [15],[28]. In the end we will discuss the numerical aspects of these models and how the various models are integrated together.

2.1 Solid-State Theory

At fundamental level the key subjects in this thesis are *electrons*, *photons* and *phonons*. We will study the properties of these particles or quasi-particles and the interactions among them in the context of semiconductor quantum-well structures, which are the underlying structures of the EAM devices that we have been

working on for optical network applications. To achieve these objectives we first need to understand the conceptual framework of solid-state theory.

Solids are an assembly of atoms, held together by chemical bond. The particles in solids, electrons and nuclei, can be characterized as two groups: valence electrons and lattice ions. Valence electrons are the electrons in outer shells of atoms. They are shared by neighboring atoms and contribute to chemical bonding. Valence electrons have strong influence on the properties of solids that are critically dependent on the way the individual atoms assemble together. The lattice ions consist of the atomic nuclei and the electrons in the closed inner shells of atoms. The division of the two groups of constituent particles provides an important framework to treat the solid-state problems and can be justified by so-called adiabatic approximation. The approximation is based on the following argument. Since electrons have much smaller mass than ions, the ions can only respond very slowly to any changes in the electron configuration while the electrons respond adiabatically to any changes in the ions positions. In other words, we can first treat lattice ions without considering valence electrons and deal with electrons assuming fixed positions of the ions. The interactions between lattice ions and valence electrons can be later treated as perturbation.

Even after the division of lattice and valence electrons, the solid remains a formidably complex system. It is too complicated for one model to describe the rich physical phenomena in solid-state systems. However, one unifying concept

that can provide a common ground for the physics studied in this thesis is *elementary excitations* [26], which can give physical pictures and at same time simplify mathematics formulation. Phonon is the elementary excitation to describe the lattice ions. From the classic mechanics we know how to describe in simple term the complex modes of oscillation of a system consisted of point masses. For a system with s degree of freedom, we can introduce s new normal coordinates so that the system Hamiltonian can be diagonalized for small oscillations. As a result, the complex equation of motion of the system can be split into s independent equations of free oscillators. We can apply this method in lattice dynamics to describe the oscillation of lattice ions about their equilibrium positions. The normal modes of lattice oscillation can be further quantized and the associated quanta are called phonons.

The concept of normal modes is effective in decoupling interacting many-body system of crystal lattice ions. One-electron approximation is the effective way to describe the interactions of valence electrons. For the system of valence electrons in crystal, the Hamiltonian consists of three terms: the kinetic energy of individual electrons, the interaction energies with the lattice ions, and the interaction energies among electrons. Under adiabatic approximation, the first two terms are sums of corresponding energies of single particles. And thus the system equations can be decoupled into sum over of single particle equation if only these two terms are present. The problem arises when the electron interaction term

couples all the wave function of individual electrons together. One-electron approximation is introduced to decouple the interacting system into the sum over of non-interacting subsystem of single particles. The idea behind one-electron approximation is as follows. If a charged particle move through a "gas" of charged particles, it will be repelled by other particles. However, we can model the particle as original particle accompanied by a compensating cloud of opposite charges. The interaction with other particles can be replaced by the inertia of the charge-cloud. The new quasi-particle behaves as if it is free of the interactions with others. One-electron approximation serves as the basis of electron states description in solid-state crystals. In the quasi-particle sense, one electron actually refers to the collective excitation of a group of electrons and is the elementary excitation of valence electrons in solids.

A considerable portion of the thesis will be devoted to exciton, which is another elementary excitation related to electrons in solid. Excitons are formed by negatively charged conduction-band electrons and positively charged valence-band holes. The valence-band holes are created when electrons on valance band are excited into conduction band. They will have the same momentum but opposite charge as that of original electrons and can also be described by one-electron approximation model.

The solid-state system consisted of lattice ions and valence electrons (or phonon and electron as will be referred later on) can be put under various external

influences. The properties of solid-state material are directly dependent upon how a solid-state system responds to the external influences. Our central task is to study the optical properties of semiconductor quantum-well material. Thus it is essential for us to study how electrons/excitons behave under optical field. This lead to another important elementary excitation: photon. Under the elementary excitation framework, photons can be viewed as electromagnetic excitation of vacuum. For the applications in this thesis, however, we do not need to invoke the whole quantization theory of optical field. The optical field can still be largely described by classical Maxwell theory. More specially, optical field intensity is described by classical electromagnetic field, but optical field interacts with electrons through its quanta (photon) whose energy and momentum are defined by optical field frequency and wavelength.

Among the above three quasi-particles described, electrons will experience profound changes when quantum confinements are presented in semiconductor material. On the other hand, phonons and photons will largely remain their three-dimensional nature. In a large portion of this thesis, we will concentrate on electrons and electron-hole pairs in quantum well structures, and how they interact with photons and phonons.

2.2 Electron states and exciton states in QW

Based on one-electron approximation discussed in the last section, electrons in semiconductor crystal can be described as free particle with effective mass different from that of electrons in vacuum. The one-electron approximation concept was introduced in the context of riding off the interaction among electrons. In real semiconductor crystal, we know there is background potential originated from the lattice ions. If we lump the interactions with other electrons and the ions together, an electron will see a periodic background potential. The state of electron in the periodic potential can be described by Bloch function. And the electron energy-momentum dispersion can be obtained using various methods such as tight-binding, pseudo-potential and $\mathbf{k}\cdot\mathbf{p}$ perturbation. The dispersions or band-structures as more often called can be very complicate. However, at the band edge that is of the most interest in investigating optical properties of semiconductor quantum structures, the dispersion can be approximated as parabolic function, which is the characteristic of a free particle. This suggests that we can replace an electron in crystal by a free electron but with different effective mass. The influence of crystal ions and other electrons have all been incorporated into the effective mass. One of our main tasks is to model electron states in a semiconductor crystal that has quantum confinement along one dimension and is under electric field, which now can be simplified as to model a free electron with an effective mass moves in the electrical potential brought by the quantum-well structure and applied electric field.

In the following sections we will present mathematical equations describing the electrons in QW based EAM. The formulations are based on $\mathbf{k}\cdot\mathbf{p}$ method that is implemented in Luttinger-Kohn Hamiltonian [29].

2.2.1 Electrons in conduction band

The electrons in conduction bands can be described by Schrödinger equation as

$$H^e\psi_i(\mathbf{k},\mathbf{r_e}) = E_i^e\psi_i(\mathbf{k},\mathbf{r_e}) \tag{2.1}$$

With the electron Hamiltonian being

$$H^e = E_c(\mathbf{k}) + V_e(z_e) - eFz_e \tag{2.2}$$

Where E_c is the conduction band dispersion of bulk semiconductor material. V_e is the quantum well potential and the third term in equation (2.2) is the potential caused by electric field F. ψ_i and E_i^e are the eigen function and eigen energy of electrons at i-th subband in quantum wells, respectively. $\mathbf{k}$ is the in-plane crystal momentum and z_e is the electron coordinate along the growth direction.

Function ψ_i in equation (2.1) represents only envelop of electron wave functions. The complete wave functions with periodic Bloch function can be written as

$$\psi_i(\mathbf{k},\mathbf{r_e}) = \frac{1}{2\pi}e^{i\mathbf{k}\cdot\boldsymbol{\rho}_e} f_i(\mathbf{k},z_e)\left|u_c\right\rangle \tag{2.3}$$

In the above equation, the growth direction envelop and the in-plane envelop have been separated, because the quantum well confinement and electric field are just along z direction as shown in equation (2.2). The angular dependence of electron wave function has often been ignored. In fact, it will play an important role in exciton state mixing which will be discussed later. With angular dependence characterized by momentum quantum number σ, the electron wave function can be expressed as

$$\psi_i(\mathbf{k},\mathbf{r}_e) = \frac{1}{2\pi} e^{i\mathbf{k}\cdot\boldsymbol{\rho}_e} f_i(z_e) e^{-\imath\sigma\theta} \left| u_c \right\rangle \tag{2.4}$$

In equation (2.4), the k dependence of envelop function along z direction has been neglected since the bulk dispersion of conduction electrons is very close to parabolic.

2.2.2 Holes in valence band

Holes in valence band can be described by Schrödinger equations as

$$\sum_{\nu'} H^h_{\nu\nu'} \psi_{j\nu'}(\mathbf{k},\mathbf{r}_h) = E^h_j \psi_{j\nu'}(\mathbf{k},\mathbf{r}_h) \tag{2.5}$$

With the hole Hamiltonian being

$$H^h_{\nu\nu'} = H^{LK}_{\nu\nu'} + V_h(z_h) + eFz_h \tag{2.6}$$

Where $H^h_{\nu\nu'}$ is Luttinger-Kohn Hamiltonian with ν being the spin index of the hole. Luttinger-Kohn Hamiltonian is a 4×4 matrix if only the most significant band mixing between heavy-hole and light-hole is considered. $\psi_{j\nu}$ and E^h_j are the eigen function and eigen energy of holes at j-th subband in quantum wells, respectively. z_h is the hole coordinate along the growth direction.

Function $\psi_{j\nu}$ in equation (2.5) represents envelop of wave functions. The complete wave functions with periodic Bloch function can be written as

$$\psi_{j\nu}(\mathbf{k},\mathbf{r_h}) = \frac{1}{2\pi} e^{i\mathbf{k}\cdot\boldsymbol{\rho}_h} g_{j\nu}(\mathbf{k}, z_h)\left|u_\nu\right\rangle \tag{2.7}$$

Where the Bloch functions $\left|u_\nu\right\rangle$ are defined as $\left|l,\nu\right\rangle$

$$\begin{aligned}
u_{hh\uparrow} &= \left|\frac{3}{2},\frac{3}{2}\right\rangle = \frac{-1}{\sqrt{2}}\left|(u_x + iu_y)\uparrow\right\rangle \\
u_{lh\uparrow} &= \left|\frac{3}{2},\frac{1}{2}\right\rangle = \frac{-1}{\sqrt{6}}\left|(u_x + iu_y)\downarrow\right\rangle + \sqrt{\frac{2}{3}}\left|u_z\uparrow\right\rangle \\
u_{lh\downarrow} &= \left|\frac{3}{2},-\frac{1}{2}\right\rangle = \frac{1}{\sqrt{6}}\left|(u_x - iu_y)\uparrow\right\rangle + \sqrt{\frac{2}{3}}\left|u_z\downarrow\right\rangle \\
u_{hh\downarrow} &= \left|\frac{3}{2},-\frac{3}{2}\right\rangle = \frac{1}{\sqrt{2}}\left|(u_x - iu_y)\downarrow\right\rangle
\end{aligned} \tag{2.8}$$

The different Bloch functions have different momentum quantum number ν (-3/2, -1/2, 1/2, 3/2) and therefore different angular dependences. Under axial

approximation, the hole wave functions with angular dependence will be modified as

$$\psi_{j\nu}(\mathbf{k},\mathbf{r}_h) = \frac{1}{2\pi} e^{i\mathbf{k}\cdot\rho_h} g_{j\nu}(k,z_h) e^{-i\nu\theta} |u_\nu\rangle \tag{2.9}$$

2.2.3 Exciton states in QW

The excitons are electron and hole pairs formed through Coulomb attraction between them. The exciton states are obtained by the following Schrödinger equations

$$\left[H^e \delta_{\nu\nu'} - H^h_{\nu\nu'} + V_{Coul}\delta_{\nu\nu'}\right]\Psi(\mathbf{r}_e,\mathbf{r}_h) = E_{ex}\Psi(\mathbf{r}_e,\mathbf{r}_h) \tag{2.10}$$

With

$$V_{Coul} = -\frac{e^2}{4\pi\varepsilon\,|\,\mathbf{r}_e - \mathbf{r}_h\,|} \tag{2.11}$$

Where H_e and $H^h_{\nu\nu'}$ are the electron and hole Hamiltonians in Equations (2.2) and (2.6). V_{Coul} is the Coulomb potential. The vectors $\mathbf{r}_e, \mathbf{r}_h$ are the position vectors of electron and hole, respectively.

Exciton wave functions can be expanded on the base of the electron and hole envelop functions that have been obtained through solving Equations (2.1) and (2.5) as

$$\Psi(\mathbf{r_e},\mathbf{r_h}) = F(\boldsymbol{\rho}, z_e, z_h) = \sum_{ij}\sum_{\mathbf{k}} \phi_{ij}^{\xi\beta}(\mathbf{k}) \frac{e^{i\mathbf{k}\bullet\boldsymbol{\rho}}}{\sqrt{A}} f_i(\mathbf{k}, z_e) \sum_{\nu} g_{j\nu}(\mathbf{k}, z_h) \tag{2.12}$$

The in-plane polar coordinate is given as $\boldsymbol{\rho} = \boldsymbol{\rho}_e - \boldsymbol{\rho}_h$. The in-plane wave functions have been expanded in momentum space, because it is easier to incorporate valence band mixing into exciton formulation in momentum space. We will discuss the real-space model in the next chapter. Based on the expansion in equation (2.12), exciton equation in momentum space can be written as [22]

$$T_{ij}(k)\phi_{ij}^{\xi\beta}(k) + \sum_{i',j'} \int_0^\infty \frac{k'dk'}{2\pi} V_{iji'j'}^{\beta}(k,k')\phi_{i'j'}^{\xi\beta}(k') = E_{ex}^{\xi\beta}\phi_{ij}^{\xi\beta}(k) \tag{2.13}$$

Where the kinetic energy term is

$$T_{ij}(k) = E_i^e(k) + E_j^h(k). \tag{2.14}$$

The non-parabolic dispersions due to valence band mixing have been incorporated into $E_j^h(k)$.

The Coulomb potential energy term is given by

$$V_{ij i'j'}^{\xi}(k,k') = -\frac{e^3}{2\varepsilon}\sum_{\nu}\int dz_e \int dz_h \int_0^{2\pi}\frac{d\theta}{2\pi}\frac{e^{-q|z_e-z_h|}}{q}e^{i(\sigma+\nu-\xi)} f_i^*(z_e) f_{i'}(z_e) g_{j\nu}^*(k,z_h) g_{j'\nu}(k',z_h)$$

(2.15)

With

$$q = (k^2 + k'^2 - 2kk'\cos\theta)^{1/2} \tag{2.16}$$

Where ξ, β are the indexes of exciton states.

2.3 Exciton absorption and saturation in QW

2.3.1 Excitonic absorption in QW

Optical absorption in QW can be described by the perturbation theory of electron-photon interaction [22],[41](Appendix A). Once the exciton wave functions are obtained, we can calculate its matrix elements or related oscillator strength. The oscillator strength per unit area for ξ, β state of exciton is [22]

$$f_{\xi\beta} = \frac{2}{m_0\hbar\omega}\left|\sum_{\nu}(\hat{\mathbf{e}}\cdot\mathbf{P}_{cv}^{\sigma\nu})\int_0^{\infty}\frac{kdk}{2\pi}\phi_{ij}^{\xi\beta}(k) I_{ij}^{\sigma\nu}(k)\delta_{\xi,\sigma+\nu}\right|^2 \tag{2.17}$$

Where $\hat{\mathbf{e}}$ is the polarization unit vector and $\mathbf{P}_{cv}^{\sigma\nu}$ the momentum matrix elements between conduction and valence Bloch functions of bulk semiconductor materials. The overlap integral between conduction and valence subbands are given by

$$I_{ij}^{\sigma\nu}(k) = \int dz f_i(z) g_{j\nu}(k,z) \tag{2.18}$$

The delta function in equation (2.17) means only the contributions from $\xi = \sigma + \nu$ are nonzero.

The excitonic absorption coefficient is finally given by

$$\alpha(\hbar\omega, F) = \frac{\pi e^2 \hbar}{n_r \varepsilon_0 m_0 c L_W} \sum_{\xi\beta} f_{\xi\beta} \frac{\Gamma/\pi}{(\hbar\omega - E_{ex}^{\xi\beta})^2 + \Gamma^2} \tag{2.19}$$

Where c, n_r, L_W and Γ are the speed of light, the quantum well width, the quantum well refractive index, and the linewidth due to various scattering, respectively. To study the electric field screening of EAM, we need to know the electric field dependence of absorption coefficient. F is the electric field in equations (2.2) and (2.6), it is implicitly included in the quantities such as $f_{\xi,\beta}$ and $E_{ex}^{\xi,\beta}$.

2.3.2 Exciton absorption saturation

The exciton absorption saturation is originated from Pauli exclusion. In the case of free carriers generation, an electron in valance band absorbs a photon and transits to conduction band, the state in conduction band occupied by the electron then will not be available to the subsequently transitions of other electrons from

valance band. This is well-known band filling effect. In the case of exciton generation, the situation is more complex and can be described by phase-space filling theory. Although the theory of phase-space filling is elaborate, it gives a simple result that relates the basic exciton parameters to the exciton absorption saturation. The exciton saturation are characterized by exciton saturation density N_S that is given by phase-space filling as [10],[11].

$$\frac{1}{N_S} = 2\pi a_0^2 \frac{E_0}{k_b T} \tag{2.20}$$

Where a_0 is the radius of exciton in quantum well and E_0 the binding energy of the first excitonic state. Equation (2.20) allows an intuitive physics interpretation. After excitons (bound electron-hole pair) are created, they are quickly thermalized with free electron-hole pairs generated through the ionizations of the excitons or non-resonant carrier excitations. Due to Pauli principle, excitons and electrons will exclude each other in the phase space ($\sim 1/a_0$). As the carrier density increases, the probability to further generate excitons will diminish and thus excitonic optical absorption will saturate. Equation (2.20) states that the larger the radius of excitons (or the smaller the corresponding phase space), the smaller the exciton saturation density. The factor $E_0 / k_b T$ means only a fraction of electrons occupy the phase space the exciton shares.

The exciton saturation density is connected to optical absorption saturation through

$$\alpha = \frac{\alpha_0(F)}{1+(N/N_S)} \tag{2.21}$$

Where α_0 is absorption coefficient obtained in equation (2.19). N is the carrier density in quantum well. In equation (2.21) the populations of electron and hole are assumed equal. In the case of different populations of electron and hole, the exciton absorption saturation can be characterized by [12],[13]

$$\frac{N}{N_S} = \frac{N_e}{N_{Se}} + \frac{N_h}{N_{Sh}} \tag{2.22}$$

With

$$N_{Se} = \frac{m_e}{m_r} N_S, \qquad N_{Sh} = \frac{m_h}{m_r} N_S \tag{2.23}$$

Where m_e and m_h are effective mass of electron and holes. And the reduced effective mass m_r is given by $(m_e m_h)/(m_e + m_h)$. Equation (2.23) indicates that electrons are easier to saturate than holes. This is because electrons have smaller effective mass and thus fewer states available at band edge. It also implies that from the standpoint to achieve strong saturation, it is desirable to have more

electrons rather than holes in quantum wells. The different saturation behaviors of electrons and holes will be investigated in details and be utilized to design highly nonlinear EAM later in this thesis.

2.4 General Formulism Carrier Transport

In this section, we will discuss the general formulation of carrier transport in order to pave the way to the carrier transport models we will use in our works, which will be described in the next section.

2.4.1 Conceptual framework

In the previous sections, we start our description of electrons in solid state with a perfect picture. Although an electron see a complex background potential in a crystal, it suffers no scattering when it moves through the structure. We have first considered the eigen states of electrons, and then the electron transition from one state to another through electron-photon interaction. The electrons at different states are considered in equilibrium that is established through various scattering mechanisms. Up to this point, no non-uniformity of any kind has been assumed. In real world environment, however, there is always non-uniformity exists due to external conditions such as electric field, carrier injection, heat conduction and so on. In this chapter we will address the issue how electrons evolve when non-uniformities are present: carrier transport.

The theoretical description of electrons so far has been based on quantum mechanics. But the full quantum mechanics treatment of carrier transport is too complicated for practical applications. Thus semi-classical approach will be employed for carrier transport problem here. According to the uncertainty relation, an electron cannot have well-defined position and momentum at same time. For an electron with wavelength of 10Å in a space region of 1000 Å, at micro-space level it has a well-defined momentum and an arbitrary position. But at macro-space level we can treat the electron as if it has a well-defined position. Figure 2-1 illustrates this semi-classical picture of carrier transport. An electron's trajectory is made up "free flight" and instantaneous scatterings. During the "free flight" the electron is assumed a particle governed by the modified Newton's equations. The path of "free flight" is not necessary straight since electron is subject to external influence such as electric field. In scatterings the electron is assumed waves governed by quantum mechanics. The electron's state will change during the scattering processes. In the following, we will describe the carrier transport processes in terms of Boltzmann transport equation.

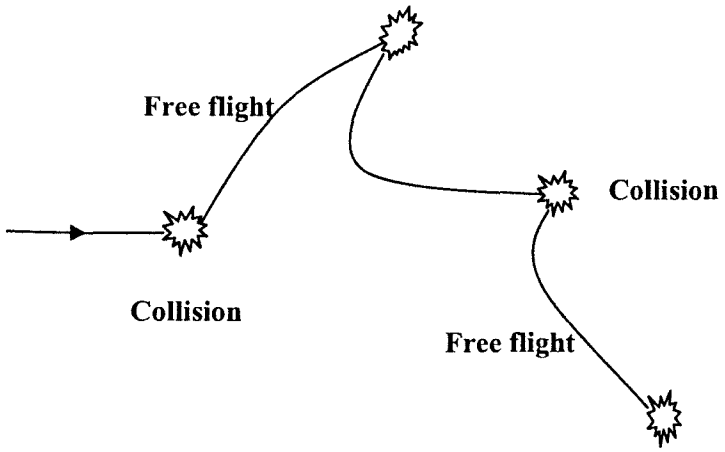

Figure 2-1 Schematic of semi-classical picture of carrier transport

2.4.2 Boltzmann Transport Equation

The electron system with the presence of non-uniformity can be described by distribution function $f(\mathbf{k},\mathbf{r})$. It represents the local occupation of the electrons in the state of $\mathbf{k}$ (crystal momentum) and in the neighborhood of $\mathbf{r}$. Boltzmann transport equation governs how the distribution function changes with time due to the following reasons: 1) electrons move into and out of any volume element around $\mathbf{r}$ (diffusion); 2) electrons change their momentum under the influence of external force like electric field (drift); 3) electrons move from one $\mathbf{k}$ state to

another during scatterings. Mathematically, the Boltzmann transport equation can be written as

$$\frac{\partial f}{\partial t} = \left.\frac{\partial f}{\partial t}\right|_{diffusion} + \left.\frac{\partial f}{\partial t}\right|_{fields} + \left.\frac{\partial f}{\partial t}\right|_{scattering} \tag{2.24}$$

The Boltzmann equation provides a foundation to treat the carrier transport problem. However, it is difficult to solve equation (2.24). For instance, the scattering term in equation (2.24) is integration over $\mathbf{k}$ of an integrand that itself involves the distribution function. The Boltzmann equation can be further written in the form of balance equations, which are more often used in practical calculations.

2.4.3 Balance Equations

To derive the balance equations, we consider a general physical quantity n_g defined by the average value of function $g(\mathbf{k})$ as

$$n_g(\mathbf{r},\mathbf{t}) = \int g(\mathbf{k}) f(\mathbf{r},\mathbf{k},t) \frac{d\mathbf{k}}{(2\pi)^3} \tag{2.25}$$

Multiply the Boltzmann equation (2.24) with $g(\mathbf{k})$ and integrate over k-space, we obtain the balance equation as

$$\frac{\partial n_g(\mathbf{r},t)}{\partial t} = -\nabla \cdot \mathbf{F}_g + G_g + R_g \tag{2.26}$$

Where the first term on the right represents a flux associated with n_g and is given by

$$F_g(\mathbf{r},t) = \int g(\mathbf{k})\mathrm{v} f \frac{d\mathbf{k}}{(2\pi)^3} \tag{2.27}$$

Here v is the group velocity of an electron. The second tern is the generation term given by

$$G_g = e\mathbf{F}\cdot\int f\nabla_p g\frac{d\mathbf{k}}{(2\pi)^3} \tag{2.28}$$

Here p is momentum of an electron. The third tern is the recombination term given by

$$R_g = \frac{1}{\tau_g}[n_g(r,t) - n_g^0(r,t)] \tag{2.29}$$

Where τ_g is the average relaxation time. Here the relaxation time approximation has been used. Under the approximation, the distribution function is not far away from its equilibrium. Therefore, the change rate of the distribution function is proportional to the perturbation of the distribution function. The proportional coefficient is the inverse of the relaxation time.

Now we derive the two most commonly used balance equations.

To obtain the balance equation of the carrier density, we can put $g(\mathbf{k}) = 1$ so that n_g = n, the carrier density. The flux term will be $\mathbf{J}/e$ with **J** being the

electron current density. The generation and recombination terms are zero. The balance equation is

$$\frac{\partial n}{\partial t} = -\frac{1}{e}\nabla \cdot \mathbf{J} \tag{2.30}$$

This is simply the current continuity equation.

The momentum balance equation can be obtained by setting $g(\mathbf{k})$ = p. Substituting this equation into (2.26) and after some mathematical manipulations [28], we can obtain the electron current density as

$$\mathbf{J} = ne\mu\mathbf{F} - eD\nabla n - eS\nabla T \tag{2.31}$$

Where μ is the electron mobility. D is the diffusion coefficient and S is the Soret coefficient. These coefficients are defined as

$$D = \frac{k_B T}{e}\mu, \qquad S = \frac{nk_B}{e}\mu \tag{2.32}$$

Equation (2.31) is the drift-diffusion equation. The current continuity equation (2.30) and the drift-diffusion equation (2.31) form the core the carrier transport model. In the next section, we will apply them to model the carrier sweep-out in quantum-well EA modulators.

2.5 Drift-Diffusion Based Transport Model

As just shown in the above, the carrier transport can be broken down into three components: drift, diffusion and thermal. In our studies, the carrier dynamics in

quantum-well regions is of primary interest. Temperature there can be considered as constant and thus we need consider the drift and diffusion terms only. As shown in equation (2.31), the drift current is determined by electric field. To obtain the electric field, the drift-diffusion equations of electron and hole have to be solved along with Poisson equation. The drift-diffusion equations and Poisson equation are often called semiconductor equations and they have been applied to various semiconductor devices. Here we will use them to describe EAM, which is essentially a PIN diode from the semiconductor device point of view. However, conventional semiconductor equations are only strictly valid for bulk devices. Modification needs to be made for quantum-well devices. In QW devices the electron and holes can be distinguished as 3D carriers (bulk states) and 2D (quantized states) carriers [15],[34],[35]. Two drift-diffusion equations are needed for 3D electrons and holes that are distributed through the whole device. Two Rate equations are needed for 2D electrons and holes in quantum well regions. The 3D carriers and the 2D carriers are connected through capture and escape processes in quantum wells.

In the following, we will discuss these equations one by one.

2.5.1 Bulk Continuity Equations

The 3D electron and hole transport are described by two continuity equations as

$$\frac{\partial n}{\partial t} = \frac{1}{e}\frac{\partial J_n}{\partial x} - R + G_n \tag{2.33}$$

$$\frac{\partial p}{\partial t} = \frac{1}{e}\frac{\partial J_p}{\partial x} + R + G_p \tag{2.34}$$

Where n and p are the density of 3D electrons and holes, and J_n and J_p the current densities of 3D electrons and holes, respectively. R is the recombination term. G_n and G_p are the generation terms which will be defined later. The current densities are further written as drift component and diffusion component as follows

$$J_n = eD_n\frac{dn}{dx} - e\mu_n n\frac{d\phi}{dx} \tag{2.35}$$

$$J_p = -eD_p\frac{dp}{dx} - e\mu_p p\frac{d\phi}{dx} \tag{2.36}$$

with D_n and D_p being the diffusion coefficient and μ_n and μ_p being mobility for electrons and holes, respectively. ϕ is electrical potential. The current density cross hetero-junctions are given by [36]

$$J_n = -e\eta v_{nA}(n_A - n_{A0}) \tag{2.37}$$

$$J_p = -e\eta v_{pA}(p_A - p_{A0}) \tag{2.38}$$

Where v_{nA} and v_{pA} are the thermal velocities of electrons and holes. n_A and p_A are the electron and hole density at A side, and n_{A0} and p_{A0} the would-be electron and hole density at A side if the quasi-Fermi levels at both sides are assumed same. η is the coefficient accounting for the tunneling through the hetero-barriers.

2.5.2 Carrier Transport between well and barriers

The dynamics of 2D electrons and holes in the i-th quantum well can be described by rate equations as

$$\frac{dn_{2D}^{i}}{dt} = -G_n^i + R_{2D}^i + G_{2D}^i \tag{2.39}$$

$$\frac{dp_{2D}^{i}}{dt} = -G_p^i + R_{2D}^i + G_{2D}^i \tag{2.40}$$

Where G_n^i and G_p^i connect equations (2.33) and (2.34) to equations (2.39) and (2.40), representing the exchange between 2D carriers and 3D carriers in quantum well regions. They are given by

$$G_n^i = \frac{1}{L_W}\left(\frac{n_{2D}^i}{\tau_{esc}^n} - \frac{n^i}{\tau_{cap}^n}\right) \tag{2.41}$$

$$G_p^i = \frac{1}{L_W}\left(\frac{p_{2D}^i}{\tau_{esc}^p} - \frac{p^i}{\tau_{cap}^p}\right) \tag{2.42}$$

Where n_{2D}^i and n^i are the densities of 2D and 3D electrons in the i-th well and p_{2D}^i and p^i the densities of 2D and 3D holes in the i-th well. The escape times are defined as [15],[37]

$$\tau_{esc}^n = \left(\frac{2\pi m_e L_W^2}{k_b T}\right)^{1/2} \exp\left(\frac{E_b^c - E_1^c}{k_b T}\right) \tag{2.43}$$

$$\tau_{esc}^p = \left(\frac{2\pi m_h L_W^2}{k_b T}\right)^{1/2} \exp\left(\frac{E_b^v - E_1^v}{k_b T}\right) \tag{2.44}$$

Here E_1^c and E_1^v are the first quantum energy level of electron and holes, E_b^c and E_b^v are the barrier potentials of electron and holes, respectively. The capture times τ_{cap}^n and τ_{cap}^p can be obtained at the condition where the 3D and 2D carriers are in thermal equilibrium. In the dynamic processes we discuss in this thesis, the 3D and 2D carriers actually are away from equilibrium. The use the capture times at thermal equilibrium for these dynamic processes means that we have assumed the capture and escape processes are the linear processes around the equilibrium [34].

The carrier escape formulations in equations (2.43) and (2.44) are based on thermionic emission of electrons. The thermionic emission model [37] has

been widely used to describe the carrier escape out of quantum wells. However, it should be pointed out that the thermionic emission description will break down when the quantum wells become shallow [38]. In principle, the electron escape out of quantum wells is through scattering of optical phonons. Ref. [38] shows that for shallow quantum wells, the first principle model instead of thermonic emission model has to be used. In chapter 5, we further shows that the Coulomb correlation of the electrons and holes has also to be considered in the escape of electrons and holes out of shallow quantum wells. In other word, we need to deal with exciton escape instead of electron escape.

In EAM, the carrier generations are through optical absorption as

$$G_{2D} = \alpha L_W v_g S \tag{2.45}$$

Where α is the material absorption coefficient given by equation (2.19) in the previous section. v_g is the group velocity S is photon density in the i-th well.

2.5.3 Poisson Equations

Finally, Poisson equation that governs the electric field is written as

$$\frac{d}{dx}\left(\varepsilon \frac{d\phi}{dx}\right) = e(p - n + N_D - N_A) \tag{2.46}$$

Where N_D and N_A are the donor and acceptor concentrations. The electron and hole density p and n here refer the summation of 2D and 3D carriers in QW regions and 3D carriers only in other regions. When an optical signal is incident upon EAM, it will generate 2D electrons and holes inside quantum well. Subsequently, these 2D carriers will be swept out of quantum well and become 3D carriers. These 2D and 3D carriers will generate additional electric field that will screen the original electric field in quantum well regions. This electric field screening will modify optical absorption through electro-absorption effects. The electric field screening is one of most important absorption saturation mechanisms to which we will revisit later.

2.6 Numerical Solutions of Model Equations

Many numerical techques have been used to solve the above equations. In the following, the key points of the numerical techques have been summarized. The details of implementations can be found in [20]~[23],[27],[53].

2.6.1 Electron state equations

Electron equations (2.1) and (2.5) are often solved using methods such as transfer matrix method (TMM) [30], shooting method [45], finite difference method (FDM) and finite element method [46]. We have used finite difference method.

FDM has the appeal of straightforward numerical implementation and easy adoption to various geometrical structures. Another advantage is that discretized equation of FDM can be solved through well-developed eigen equation package, eigen value will be fully accounted for. This is contrast to the case of "roots searching" in other methods where some close solutions can be easily missed. The drawback of FDM is that it is not as fast as the methods described in [30] [45].

2.6.2 Exciton state equations

The eigen energy and eigen functions $E_{ex}^{\xi,\beta}$ and $\phi_{nm}^{\xi,\beta}$ of excitons in equation (2.13) can be obtained either variationally [32] or numerically [21][22]. Variational methods are often accurate in eigen energy but could induce inaccuracy in eigen function as much as 30% [33]. For numerical methods, the difficult is to treat the singularity due to Coulomb potential and computation time of multi-fold integrals. In our model, the modified Gaussian quadrature method [21][22] has been employed to remove the singularity and obtain numerical solutions of integral equation (2.13). Some mathematical manipulations are used to speed up the computation.

2.6.3 Drift-diffusion equations

Due to the drastical variation of carrier density in semiconductor devices and the inherent nonlinearity of the equations, drift-diffusion equations are usually difficult to solve, especially for the structure with high hetero-junction barriers as we encounter in our structure. Their solution techniques have been studied extensively [23],[27]. We have adopted a variation of Newton's method, similar to that in Ref. [23]. For 2D electron and hole rate equations, ordinary forward Euler method has been used.

2.6.4 Integration of all model equations

A self-consistent integration of models in this chapter is achieved as follows. The optical absorption is calculated as function of electric field based on the models in Section 2.3 (Equations (2.19) and (2.21)). The carrier transport models in Section 2.5 will self-consistently calculate the electric field inside EAM using the optical absorption obtained in Section 2.3. The optical absorption acts as a generation term in quantum well regions in the rate equations of 2D carrier in quantum wells (Equations (2.39), (2.40) and (2.45)).

Chapter 3

Modeling of Electron States in QW Using PML

3.1 Introduction

As discussed in Chapter 2, the modeling of optical absorption in semiconductor quantum wells requires the consideration of three physics problems: electron states, exciton states and optical transitions. In Chapter 2 these physics have been addressed in a comprehensive manner, including full account of valence band mixing and exciton state mixing. For many engineering applications, however, a simple and efficient approach may be preferable. In this chapter we will develop an optical absorption model based on simple parabolic band structure for both electrons and holes, apply it to practical device structures and compare the simulation results with measured data.

From the modeling point of view, we will also address the issue of electron states in quantum wells with shallow barrier potentials or under strong applied electric field. Leaky waves in such structures are of mathematical and practical interest [39]~[44]. In EA modulators, the electric potentials of the quantum wells

and barriers are tilted due to an applied electric field. Consequently, there are strictly speaking no bound states like those in a quantum well with flat potential barrier. All states are unbound and their energy spectrum continuous. This situation poses a significant challenge for the modeling and analysis for the electron states in the quantum wells under the electric fields, especially for highly tilted and/or shallow quantum well where electron wave leakage is strong.

Several methods have been used to solve this problem [40]~[45]. One of the approaches is based on the discrete state representation of continuous states [45]. Using a potential barrier of infinite height at the edges of the computation window, the continuous unbound states are reduced to a set of discrete states that are bounded in the large domain defined by the infinite potential barriers. This boundary condition has been applied only to cases from weak to moderate electric field where the electron is largely confined by the quantum well barrier potential and the leakage due to the tunneling is small. Under this condition, a bound state of a flat potential well becomes a little leaky and practically can still be approximated by a discrete state obtained through infinite barriers condition (IBC). But can IBC be extended to strong electric field case where electron wave leakage is large? Theoretically speaking, if the number of discrete states is large enough, we can approximate accurately enough continuous unbounded states with discrete states. We will examine if this approach is practical, especially in calculating excitonic absorption.

Another approach is based on the quasi-bound state representation [40]~[42]. Besides the discrete state representation, it has been shown in [47],[48] that in a complex plane continuous unbound states can be represented by a small number of discrete complex quasi-bound states plus a branch integral. For many applications, the branch integral can be neglected. Thus the discrete complex quasi-bound states may serve as a convenient, yet accurate representation of the continuous unbound states. Furthermore, the imaginary parts of the complex energy eigen values of the quasi-bound states can be considered as the electron life time in the quantum wells due to tunneling. The quasi-bound states defined by the complex theory, however, are difficult to deal with numerically as the wave functions diverge beyond a certain distance away from the wells and cannot be readily normalized. The boundary condition employing the perfectly matched layer (PML) has been used to obtain the quasi-bound state numerically.

The PML boundary condition was originally proposed by Berenger [49] for the finite-difference time-domain solution of Maxwell's equations in a finite computation domain without reflection from the numerical boundaries. It was later introduced to solutions of Helmholtz equations in the context of one-way propagation [50] and mode solutions [51]. The application of the PML for Schrödinger equations leads to complex quasi-bound states, similar to the leaky modes in the electromagnetic waveguides. The PML, which is usually terminated by the transparent boundary condition, has been used to analyze the electron states

and was shown to result in reduction of the computation time in order of magnitude over infinite barrier boundary condition and more accurate than the absorbing boundary condition (ABC) by a factor of two [52]. The PML can also be terminated by an infinite potential barrier [53], in this chapter we will focus on this boundary condition and apply it into quasi-state analysis in tilted quantum wells.

The boundary condition of PML backed up with infinite barriers has several advantages. Conceptually, the quasi-bound states are well defined in terms of orthogonality and normalization of the wave functions. This is in contrast to the quasi-bound state in the open structure as obtained using the PML in combination with the transparent boundary condition. In terms of numerical computation efficiency, the computation algorithm does not need the outer iteration loop required for the transparent boundary condition and therefore is more efficient. Finally, an infinite potential barrier means the wave function instead of its derivative will be zero at the very end of the boundary, which makes it easy to extend to the case where multiple electron states such as heavy-hole and light-hole and their band mixing are presented.

In the following sections, first, we will first carry out some fundamental studies on the PML boundary condition, and how it affects the bound, quasi-bound, and unbounded states. It mainly focuses on flat quantum wells where an analytical formulation can be used to facilitate the discussion. Then, we apply the

IBC and PML+IBC to tilted quantum wells. Next, the different electron state representations are incorporated into and compared in the absorption calculation. Finally, the numerical results are compared with experiment data.

3.2 Electron States

In the following, both electrons and holes are assumed to have parabolic dispersion. They differ only in effective mass and potential barrier height.

3.2.1 Electron wave equation with PML

In the presence of the PML, the electron wave equation with tilted quantum well potential can be written as [53]

$$\frac{d}{d\tilde{z}}\left(\frac{1}{m^*}\frac{d\varphi}{d\tilde{z}}\right)-\frac{2}{\hbar^2}\left(V+eFz-E_z\right)\varphi=0. \tag{3.1}$$

Where φ is the wave function, m^* is the effective mass of electrons or holes, F is the applied electric field along z (the growth direction), V is the well potential, and E_z is the electron eigen energy. The spatial variable $\tilde{z}$ is defined as

$$\tilde{z}=\int_0^z \alpha(z')dz' \tag{3.2}$$

And the parameter α is defined as

$$\alpha = \begin{cases} 1 & \text{Non-PML Region} \\ 1+(\kappa-1)f(z)-j\alpha_0 f(z) & \text{PML Region} \end{cases} \tag{3.3}$$

Where κ is the parameter that can adjust the effective PML length and α_0 is the PML attenuation parameter and $f(z)$ is the function for normalized PML profile. Equation (3.1) becomes complex equation due to the presence of the PML region.

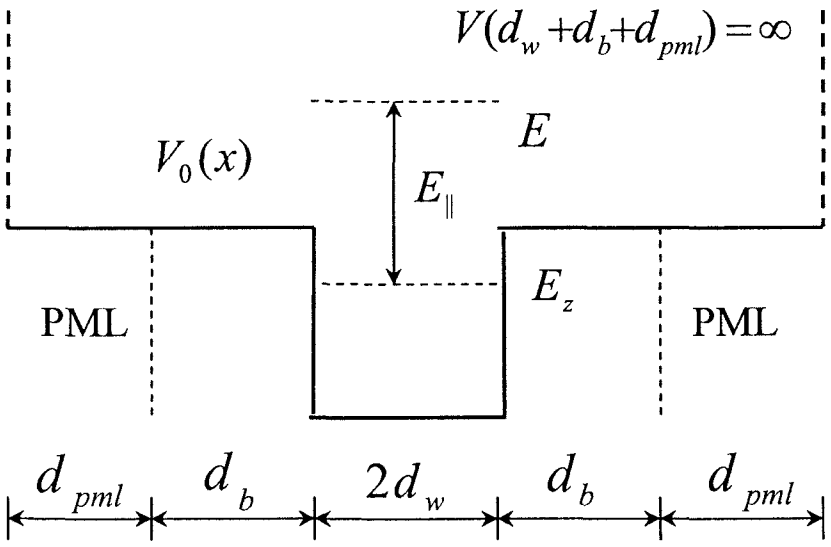

Figure 3-1 Band diagram of quantum well without electric field. The infinite potential barriers are placed at the end of PML

3.2.2 Confined electron states with PML

It is instructive to consider a special case with flat barrier potential where

analytical solutions exist. For the electron states confined in the quantum well with flat potential as shown in Figure 3-1, the analytical solutions for the eigen functions are:

$$\varphi = \varphi_0 \begin{cases} \dfrac{\sin[k_z'(z+d)]}{\sin[k_z'(-d_w+d)]} & -d < z < -d_w \\ \dfrac{\cos(k_z z)}{\cos(k_z d_w)} & |z| < d_w \\ \dfrac{\sin[k_z'(z-d)]}{\sin[k_z'(d_w-d)]} & d > z > d_w \end{cases} \tag{3.4}$$

Where the d is

$$d = d_w + d_b + \tilde{d}_{PML} \tag{3.5}$$

And the complex thickness of the PML is defined as

$$\tilde{d}_{PML} = \int_0^{d_{PML}} \alpha(z')dz' \tag{3.6}$$

or more explicitly if κ and $f(z)$ in equation (3.3) are taken as 1, we have:

$$\tilde{d}_{PML} = \int_0^{d_{PML}} [1 - j\alpha_o]dx = (1 - j\alpha_o)\, d_{PML} \tag{3.7}$$

And the eigen values are obtained from characteristic equation

$$k_z \tan(k_z d_w) = k_z' \cot[k_z'(d_b + \tilde{d}_{PML})] \tag{3.8}$$

Where the wave vectors are

$$k_z^{\,2} = \frac{2m^*}{\hbar^2} E_z = \frac{2m^*}{\hbar^2}(E - E_{\|}) \tag{3.9}$$

$$k_z^{'2} = \frac{2m^*}{\hbar^2}(E_z - V_0) = \frac{2m^*}{\hbar^2}(E - V_0 - E_{\|}) \tag{3.10}$$

The complete set of eigen-states of the quantum well consists of discrete bound and continuous unbound states. To better illustrate how the PML affects the continuous unbound states, we introduce the total energy and the in-plane energy $E_{\|}$ that represents the electron movement in the quantum well plane. Let us first examine the bound states for which $E - E_{\|}$ is positive and $E - V_0 - E_{\|}$ negative (see Figure 3-1)). And then k_z will be real and $k_z^{'}$ be imaginary. Writing $k_z^{'} = j\gamma$, equation (3.8) can be re-written as

$$k_z \tan(k_z d_w) = -\gamma \frac{e^{-\gamma(d_b + d_{PML})} + e^{\gamma(d_b + d_{PML})} e^{-2\gamma\alpha_0 d_{PML})}}{e^{-\gamma(d_b + d_{PML})} - e^{\gamma(d_b + d_{PML})} e^{-2\gamma\alpha_0 d_{PML})}} \tag{3.11}$$

It is noted that, when the PML is placed sufficiently far from the well, the first terms in the dominator and the numerator can be neglected. As a result, equation (3.11) is reduced to

$$k_z \tan(k_z z)\phi = \gamma \tag{3.12}$$

This is the characteristic equation of the quantum well treated as an open structure. We can see that the bound states of the quantum well are not much affected by the presence of the PML.

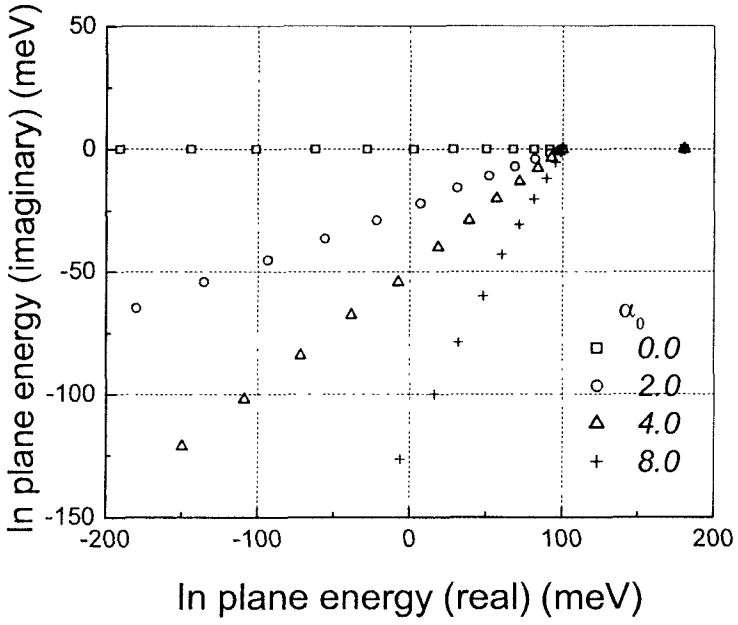

Figure 3-2 Eigen spectrum of electron in quantum well terminated by PML plus infinite barrier

In general, equation (3.8) can be solved by a tracking algorithm for complex roots and the eigen values are shown in Figure 3-2 for different PML parameters. The quantum well of 100.0 meV deep and 12nm wide are simulated. The electron total

energy of 200.0 meV and free electron mass are assumed in the calculation. 3nm PML regions are placed at both side and PML regions are terminated by infinite barriers. The attenuation of the PML is taken as constant 0.0, 2.0, 4.0 and 8.0. In Figure 3-2, the bound state is represented by the point on the real axis above 100meV. When attenuation of PML changes, the positions of the bound states stay fixed and hence not affected by the existence of the PML. When the PML attenuation parameter α_o is zero, the continuous states fall into the range of 0~100 meV, whereas the evanescent states fall below zero. As the PML attenuation increases, the energies become complex with decreasing real parts and increasing imaginary parts.

The wave functions of bound state obtained with and without the PML are plotted in Figure 3-3. For the bound states, we can hardly see any difference with or without the PML in non-PML region. For the unbounded states, we need make some distinctions. One category of un-bounded states may be termed as the PML states as these electrons have significant presence in the PML region and their behaviors are affected strongly by the PML attenuation. Another category is the leaky states primarily concentrate in the non-PML region. In the flat quantum well case, these leaky states correspond to the continuous states with real k vector. In the tilted quantum well, they become the quasi-bound states and will have both real and imaginary parts for the k vector. They are in fact similar in the non-PML

region to the quasi-bound states in the open structure. It should be pointed out that the quasi-bound states in the open structure are mathematically different from these quasi-bound states as they are not orthogonal and normalizable in real space. For the quasi-bound states in the PML closed structure, they are orthogonal and normalizable in real space and form a complete set of base functions.

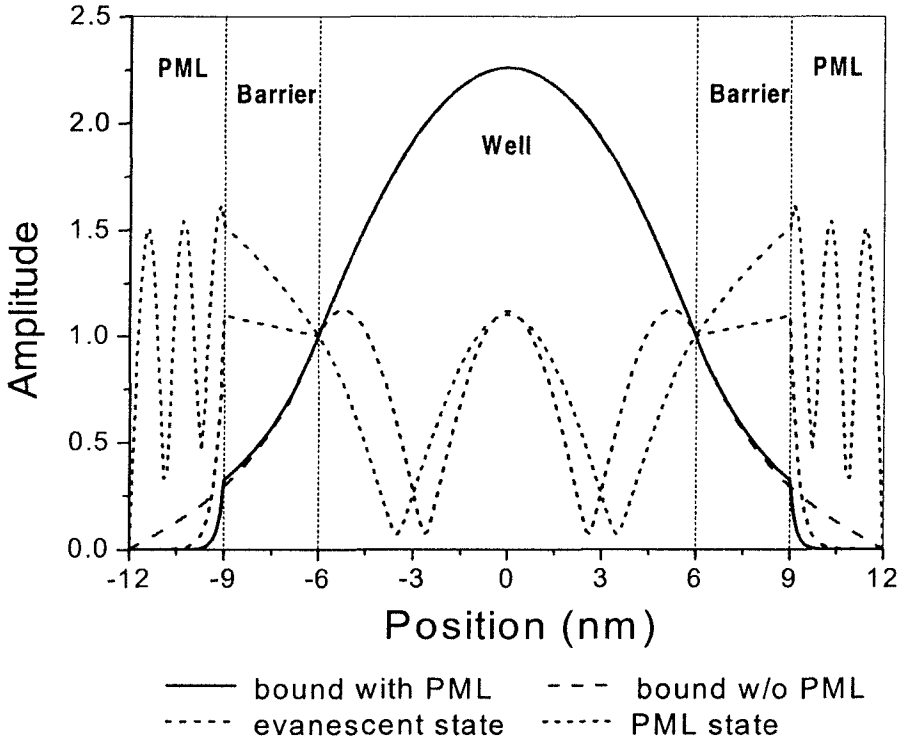

Figure 3-3 Wave functions of various electron states in quantum well without applied electrical field

3.2.3 Electron states under electric field

For the electron states of the quantum well in the presence of the external electric fields, analytical solutions are difficult to obtain when the PML layer is included and we will have to resort to numerical solutions. Equation (3.1) can be solved numerically using the finite-difference method. The attenuation in the PML is chosen as

$$\alpha = -j\alpha_0 f(z) = -j\alpha_0 (\frac{z}{d_{PML}})^m \tag{3.13}$$

Where z is measured from the start of PML region. The extent of attenuation is determined by α_0 and the profile function. $f(z)$ is chosen such that the amplitude of the wave function decays to a value sufficiently small at the PML boundary. The profile function $f(z)$ is usually taken as power function of order m. Comparing equation (3.13) with equation (3.3), the parameter κ in equation (3.3) has been taken as 1. In general, κ term can adjust the effective PML length and therefore may improve the efficiency of PML for some applications. For the tilted quantum well case, we have found that the attenuation in equation (3.13) works sufficiently well. For the sake of simplicity, this effective length term has been dropped by setting κ as 1.

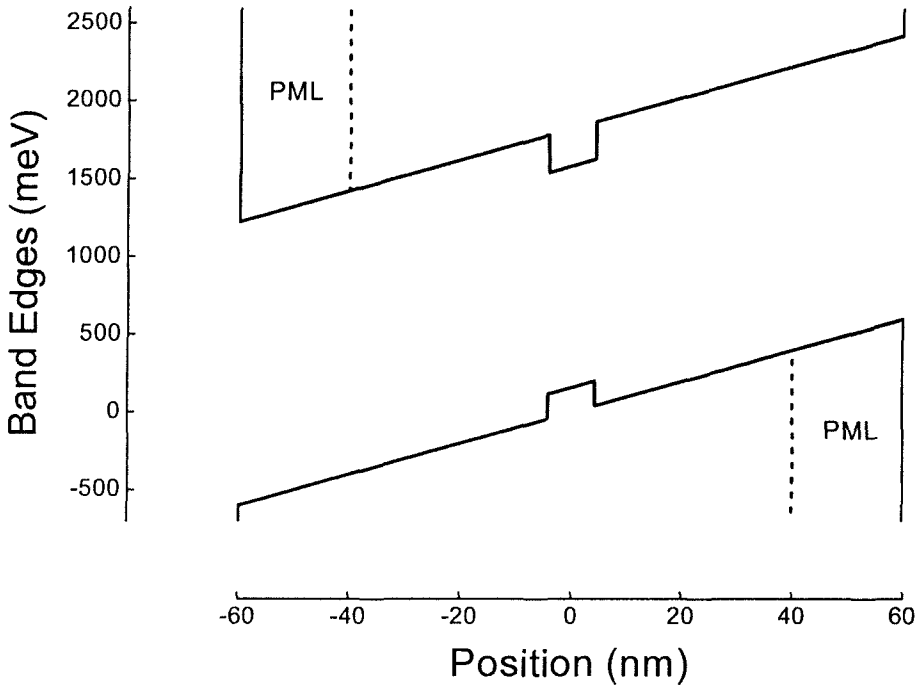

Figure 3-4 Band diagram of quantum well with applied electric field 100kV/cm. The infinite potential barriers are placed at both end and PML region in last 30nm

A quantum well of $Al_{0.7}Ga_{0.3}As/GaAs$ is numerically solved for the cases with the presence of the applied electric field. The quantum well width is 8.5nm. The band diagram is shown in Figure 3-4 for the case of field 100 kV/cm. The PML is placed at the left side for electrons and the right side for holes. Infinite potentials are used at the edges of the computation window on both sides. For moderate electric field (i.e., 100 kV/cm) the wave functions of electron calculated with and

without PML are plotted in Figure 3-5. We can hardly see any difference between the wave functions obtained for different boundary conditions. For strong electric field of 200 kV/cm, the boundary with PML yields only one quasi-bound state (Figure 3-6b), yet the boundary with the infinite barrier only produces several discrete states. The state with strongest confinement is plotted in Figure 3-6a. We have computed this state assuming slightly different window sizes, i.e., 119.2nm, 120.0nm and 120.8nm, respectively. We note that the wave functions produced by the infinite barrier boundary condition are highly sensitive to the computation window sizes, a phenomenon not observed for that obtained by the use of PML.

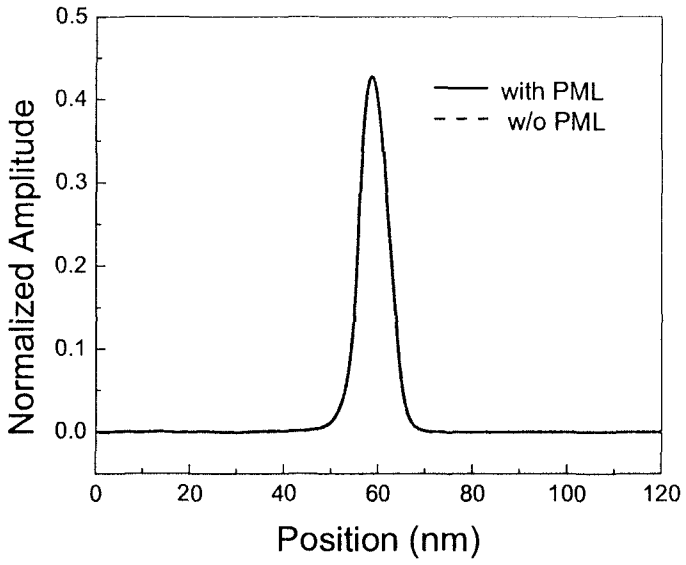

Figure 3-5 Wave function for moderate electric field 100 kV/cm

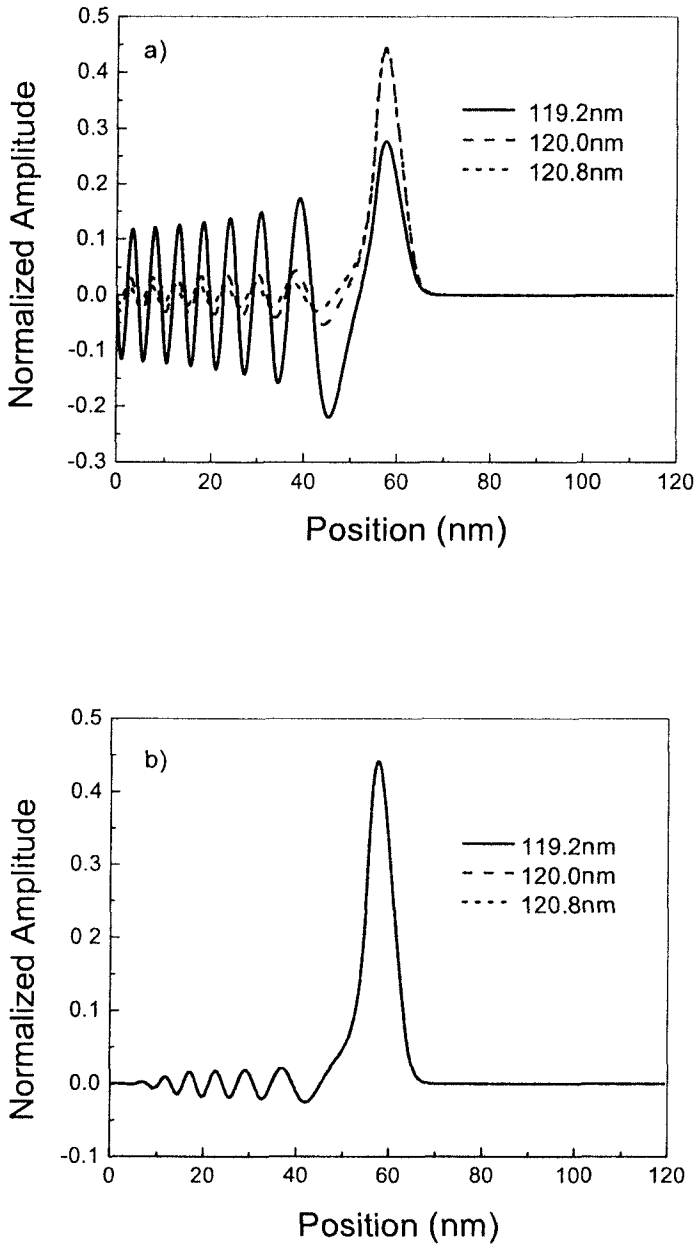

Figure 3-6 Wave function for high field 200 kV/cm. a. infinite barrier alone; b infinite barrier + PML.

The dependence of eigen-values on the window size is also examined in Figure 3-7 for two different boundary conditions. The electric field is 200 kV/cm. The solid line represents the eigen energy obtained by the infinite barrier and exhibits under-damped oscillation as the window size increases. The PML solution gives complex energy $\widetilde{E} = E_r - jE_i$. The real part stands for the center position of the energy level and the imaginary part represents the broadening of the energy level of the titled quantum wells due to tunneling of electrons/holes. $2E_i$ is the full width of half maximum of energy broadening and can be further related to electron lifetime by $\tau = \hbar / 2E_i$. The complex energy calculated using different computation window size has been plotted in Figure 3-7. The dash line represents the real part of the eigen energy for the quasi bound state calculated by the addition of the PML, which shows very little variations with the change of window size. The small variation of dash line is due to various numerical factors and is much less than the energy broadening which is represented by imaginary energy: the dotted line in Figure 3-7. Note that the energy levels obtained from the solutions without PML are always real and therefore the energy broadening effects may not be readily modeled.

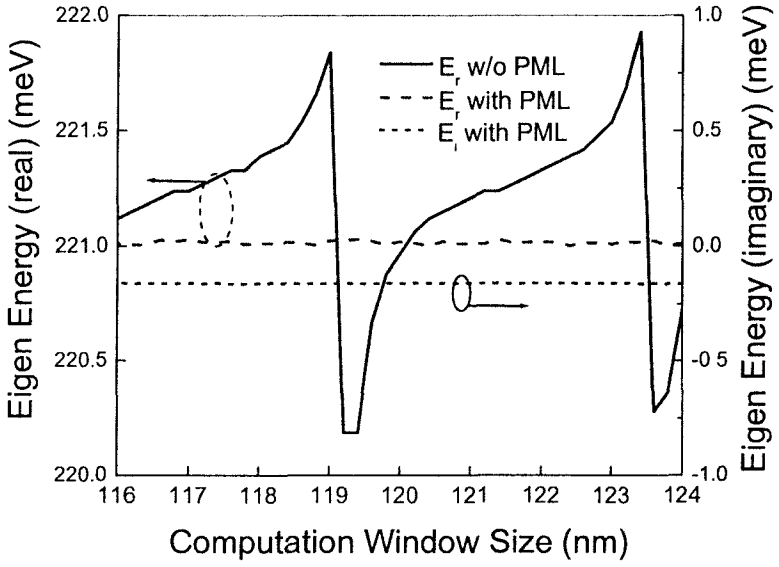

Figure 3-7 Eigen energies as function of computation window size

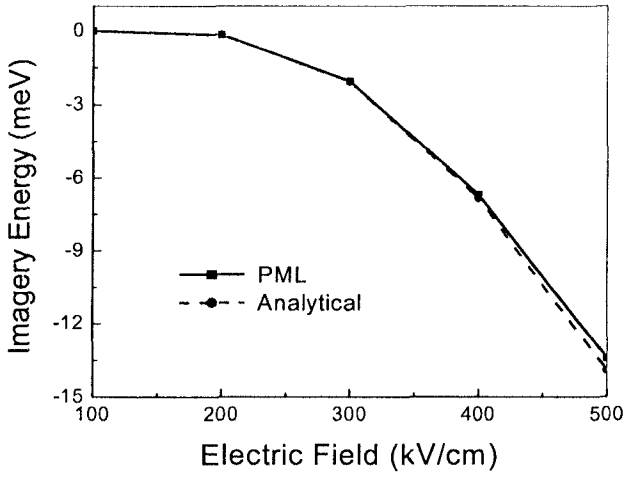

Figure 3-8 Energy level broadening calculated from PML+IP model and analytical model

To validate the model based on PML plus infinite potential barrier boundary condition, we have compared the complex energy eigen values obtained by other methods, quasi-bound states in open structures calculated by the Airy functions [40],[41]. The imaginary energies obtained by Airy functions method and by PML method are shown in Figure 3-8 and very good agreement has been found for the two models.

3.3 States of Exciton

The excitons formed through Coulomb attraction of conduction electrons and valence holes are governed by the following Schrödinger equations

$$\left[H_e - H_h + E_g - \frac{e^2}{4\pi\varepsilon\,|\,\mathbf{r}_e - \mathbf{r}_h\,|}\right]\Phi(\mathbf{r}_e,\mathbf{r}_h) = E\,\Phi(\mathbf{r}_e,\mathbf{r}_h) \tag{3.14}$$

Where H_e and H_h are the conduction band and valence band Hamiltonians in equation (3.1). The vectors $\mathbf{r}_e, \mathbf{r}_k$ are the position vectors of electron and hole, respectively.

After solving equation (3.1) for electrons and holes, exciton wave functions can then be expanded on the base of the quantum well envelop functions as

$$\Phi(\mathbf{r}_e, \mathbf{r}_h) = F(\boldsymbol{\rho}, z_e, z_h) = \sum_{i,j} \phi_{ij}(\boldsymbol{\rho}) f_i(z_e) g_j(z_h) \tag{3.15}$$

The z_e, z_k are the longitudinal coordinates along growth direction. The in-plane coordinate is given by $\boldsymbol{\rho} = \boldsymbol{\rho}_e - \boldsymbol{\rho}_h$. Index i, j are for subbands of conduction electrons and valence holes.

Substitute equation (3.15) into equation (3.14), multiply $f_i^*(z_e)$ and $g_j^*(z_h)$, and integrate over z_e and z_h. We obtain the exciton equation in the real-space as

$$[-\frac{\hbar^2}{2m_r}\nabla_\rho^2 - V_{ij}^{ij}(\boldsymbol{\rho})]\phi_{ij}(\boldsymbol{\rho}) - \sum_{i\neq i', j\neq j'} V_{ij}^{i'j'}(\boldsymbol{\rho})\phi_{i'j'}(\boldsymbol{\rho}) = E_{ex}\phi_{ij}(\boldsymbol{\rho}) \tag{3.16}$$

with

$$\frac{1}{m_r} = \frac{1}{m_{e//}^*} + \frac{1}{m_{h//}^*} \tag{3.17}$$

$$E_{ex} = E - (E_g + E_{en} - E_{hm}) \tag{3.18}$$

$$V_{ij}^{i'j'}(\rho) = \int dz_e f_i^*(z_e) f_{i'}(z_e) \int dz_h g_j^*(z_h) g_{j'}(z_h) \frac{e^2}{4\pi\varepsilon\sqrt{\rho^2 + |z_e - z_h|^2}} \tag{3.19}$$

$m^*_{e//}$ and $m^*_{h//}$ are the in-plane effective masses of electrons and holes, different from the longitudinal effective masses in equation (3.1). E_{ex} is the exciton binding energy.

In equation (3.16), the terms in the summation represent the coupling between the sub-bands due to Coulomb potential. They normally can be ignored when the differences of the sub-bands are much larger than the exciton binding energy. In the case where the infinite potential barrier is used as the boundary condition for a strongly tilted quantum well, one normal sub-band will be represented by a number of discrete states. The summation terms may represent the coupling between these discrete states.

The variational method is often used to solve equation (3.16) [32]. For instance, in the case where the coupling terms in equation (3.16) can be dropped, we only need to solve for the exciton state associated with one conduction subband and one valence subband. For the ground state 1s, a simple trial function is chosen as [54]

$$\phi_{ij}(\boldsymbol{\rho}) = \sqrt{\frac{2}{\pi}}\frac{1}{\lambda}e^{-\rho/\lambda} \tag{3.20}$$

where

$$\lambda = \frac{a_0}{\beta}, \qquad a_0 = \frac{4\pi\varepsilon\hbar^2}{e^2 m_r} \tag{3.21}$$

β is obtained through minimizing

$$\varepsilon_{ex} = \beta^2 - 4\beta \int_{-\infty}^{+\infty} dz_e \left| f_i(z_e) \right|^2 \int_{-\infty}^{+\infty} dz_h \left| g_j(z_h) \right|^2 G\left(\frac{2\beta |z_e - z_h|}{a_0} \right) \tag{3.22}$$

where ε_{ex} is the normalized exciton binding energy $\varepsilon_{ex} = E_{ex} / R_y$. $R_y = m_r e^4 / 2\hbar^2 (4\pi\varepsilon_s)^2$. The function $G(x)$ is an integral defined as

$$G(x) = \int_0^\infty dt \frac{te^{-t}}{(t^2 + x^2)^{1/2}} \tag{3.23}$$

3.4 Optical absorption

Based on the formulation of optical absorption of semiconductor quantum wells in Appendix A, the optical absorption coefficient can be expressed as [54]

$$\alpha(\omega) = \frac{C_0 M_b^2}{\pi\hbar^2 L_w} \sum_{ij} I_{ij}^2 \frac{k_0^2}{R_y} \left[4 \sum_{x=\text{discrete states}} M(0) \left| a_0 \phi_{ij}^x(0) \right|^2 \frac{R_y \Gamma}{(E_x - \hbar\omega)^2 + \Gamma^2} + \int_0^\infty dE_t M(E_t) \left| \phi^x(0) \right|^2 \frac{\Gamma/\pi}{(E_x - \hbar\omega)^2 + \Gamma^2} \right] \tag{3.24}$$

where $\phi^x(0)$ is the wave function at the center which represents the probability to find the electron and hole in the same cell. I_{ij} is the overlap between electron and hole wave functions along z direction. $\phi^x(0)$ is solution of equation (3.16) and I_{ij} is of equation (3.1). Other parameters have their normal meanings.

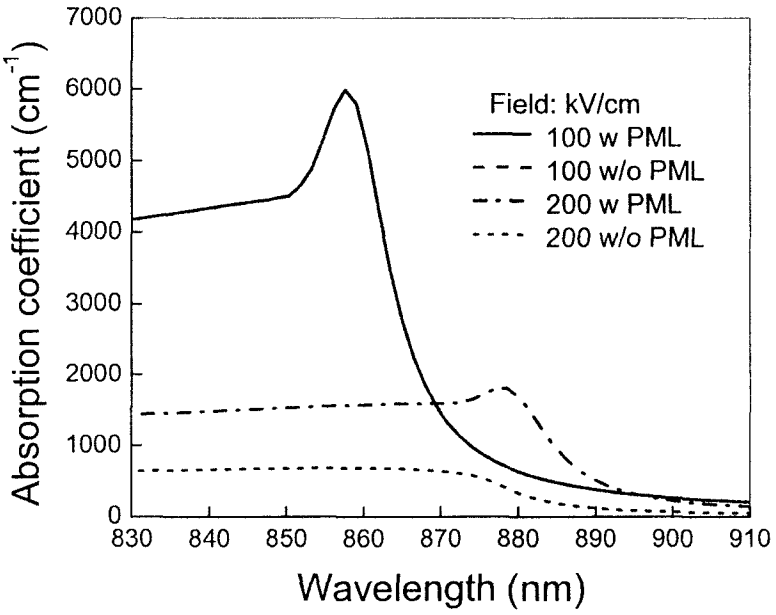

Figure 3-9 Optical absorption calculated using electron wave functions from PML plus infinite barriers and from infinite barrier only for different electric field strength

We first calculate the exciton absorption based on the states in Figure 3-5 and Figure 3-6 and the results are shown in Figure 3-9. For moderate electric field of 100.0 kV/cm, there is little difference between the states with and without PML

as shown in Figure 3-5. Consequently, their spectra match well as shown by solid and dash lines in Figure 3-9. For strong electric field of 200kV/cm, the complex quasi-bound state from PML yields one absorption curve (dash-dot line) whereas the states without PML will give a range of solution for the different computation window sizes. The dotted curve in Figure 3-9 is calculated using the state in Figure 3-6a that from 119.2nm window size (solid line in Figure 3-6a). The dotted curve is far away from the PML result. The problem is inherited for the states obtaining by infinite potential boundary condition. In the following, we will have a close examination of this problem.

An infinite potential is fully reflective and will make the continuous states of tilted quantum wells discrete. The energy spacing between discrete neighboring states is roughly inversely proportional to the square of computation domain size. For the field of 200kV//cm, we have calculated the energy spreading of quasi bound state is about 0.2meV. For normal window size of hundred nanometers for a quantum well at the size of 10nm, the energy space between two neighboring discrete states will be a few meV. Thus for accurate description of 0.2meV energy spreading using discrete states, we need a window size of 10^6 nm. The huge window size is practically impossible for numerical implementation. In addition, to obtain the optical absorption formula equation (3.24), it has been assumed that the domain of the electron wave is much smaller than the optical wavelength ($\sim 10^3$ nm) so that the optical vector potential in photon-electron interaction can be

considered as constant. If the electron waves spread in a domain of size 10^6 nm, the optical absorption formulation will not be valid anymore. In other words, from a pure state expansion point of view, the continuous states in a tilted quantum well can be either represented by quasi-bound states of PML or a set of discrete states of an infinite potential. But the discrete states cannot be used for absorption calculation for the strong field case.

We have also calculated the exciton electro-absorption of a quantum well based on GaAsInP/GaAsInP material system. The structure is taken from reference [44], which is an InGaAsP quantum well of 1.2% compressive strain with 1.1um InGaAsP barrier. The well width is 10nm. In general, the well depths are shallower in InP material system than in GaAs system. An electric field of 150 kV/cm can be considered strong for InP system. We have also calculated the absorption under various electric fields from 0.0 to 150.0 (kV/cm). The sub-bands considered include CB1, HH1, HH2 and LH1, which are relevant to the absorption of interest around the 1.55 um wavelength range. The calculation is done for the quasi-bound state representation only. The results are compared with those in [44]. The absorption has been calculated using Landau's model and also experimentally measured in [44]. Our simulation results (solid lines) and the theoretical results (dashed lines) from [44] are shown in Figure 3-10a and the experimental measurements in Figure 3-10b. Good agreement is achieved between our simulation and the theoretical/experimental results in the said reference. The

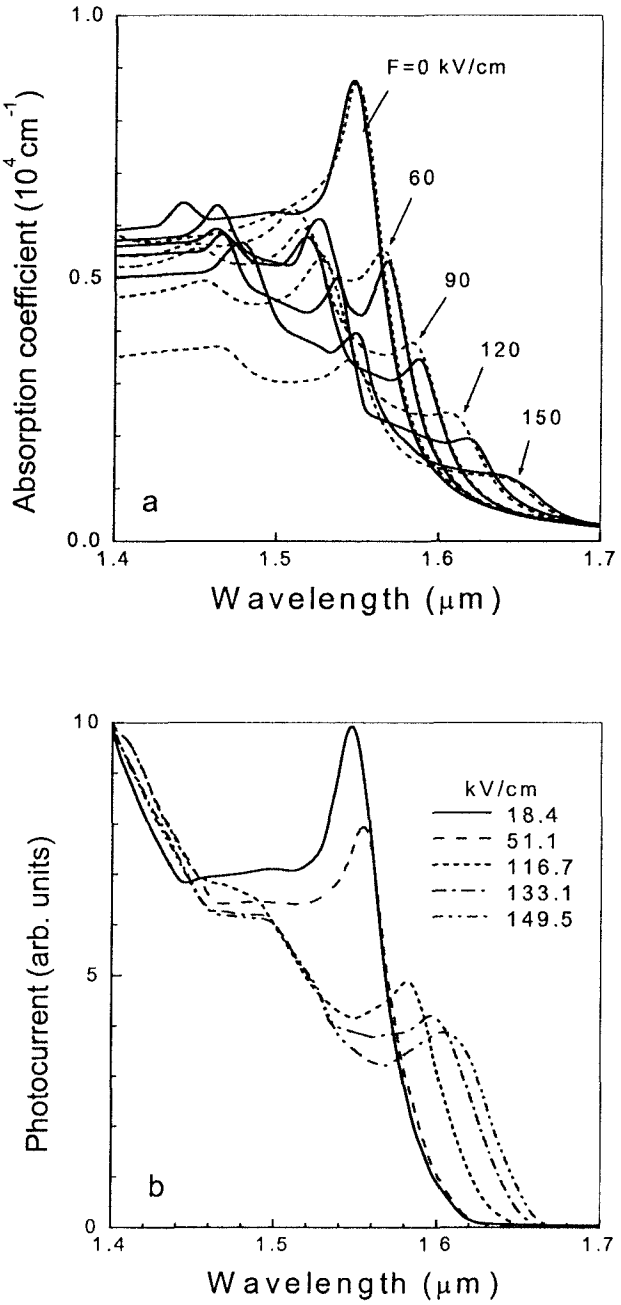

Figure 3-10 Exciton absorption spectra. a. calculated spectra of Ref. 44 and the PML model. b. measured spectra.

PML parameters are 10nm of d_{PML} at 0.5 of α_0 for the calculation. The exciton peaks shift towards longer wavelength and the exciton broadenings under strong fields appear to be larger in the calculated spectra which may be attributed to a lack of accuracy for the band gap parameters of the strained material and the uncertainty of the ratio between the conduction band and valence band discontinuities.

3.5 Conclusions

The boundary condition of the perfect matched layer terminated by the infinite potential is used for the state analysis of electron waves in tilted quantum wells. The quasi-bound quantum well under strong electric field can be fast and accurately solved using numerical methods such as FDM and are readily normalized in real space. The quasi-bound states can be conveniently incorporated into the exciton absorption model of quantum wells, and the imaginary part of the eigen energy of the quasi-bound state also gives the energy level broadening. The boundary condition used here can also be applied to the electron state analysis of other nanostructures [56].

Chapter 4

Exciton-State Mixing Effects on Optical Transitions

4.1 Introduction

The wavelength converters used in optical networks are often based on optical nonlinearity of interband transitions. Recently, the idea to enhance the optical nonlinearity in undoped semiconductor QW by coupling interband transition and intersubband transitions (IST) has been proposed [57]. By utilizing the intersubband transition, higher-order nonlinearity becomes accessible and this opens up the potential of ultra-fast optical nonlinearity. To realize such novel devices, we need to study photo-induced intersubband transitions (PI IST). In n-type QWs an infrared light can lead to excitation of electrons from the heavily populated conduction ground subband to an upper one. In undoped QWs, however, such a process requires simultaneous application of an interband optical field to excite electrons (and holes). This is called photo-induced intersubband transitions [58]. In contrast to the ISTs in n-doped QWs, PI ISTs happen in the presence of the photo-excited holes that are simultaneously generated by the

interband optical field. Therefore, as shown in [59], Coulomb interaction between the photo-excited electrons and holes can drastically influence such transitions. In other words, Coulomb interaction makes PI ISTs strongly excitonic in nature. In this chapter, we will consider the excitonic nature of PI ISTs.

In the previous studies [59],[60], the effects of excitonic states on PI ISTs were studied considering only excitation of s-state excitons. Just the transitions between the 1s and 2s states of the excitons associated with e1 and e2 were included (Figure 4-1). It is known, however, that when two valence subbands are close tegother, exciton states are no longer pure, i.e., they cannot be described by a single orbital angular momentum (m). Under such a condition the interband selection rules that only allow formation of excitons with zero orbital angular momentum (m=0) are relaxed. Therefore, depending on the QW parameters, an exciton state can be a mixture of various m (s, p, d, etc.) [61]. Our objective in this chapter is to study how such an excitonic angular mixing process influences the PI ISTs and discuss how it can characteristically determine the physical nature of the interaction between intense infrared laser fields and un-doped QWs. We show that when such a mixing process occurs an infrared laser nearly resonant with e1 and e2 can in fact lead to intersubband excitations with different angular momentum attributions, imitating the electronic transitions in quantum dots [62]. Under this condition, the IST between e1 and e2 can be translated into transitions between s, p or d states of the excitons associated and e1 with those of the excitons associated

with e2. It will be shown in the following how the presence of non s-state components will affect the oscillator strengths of the PI ISTs and how they can be engineered by the strain in QWs.

4.2 Formulations

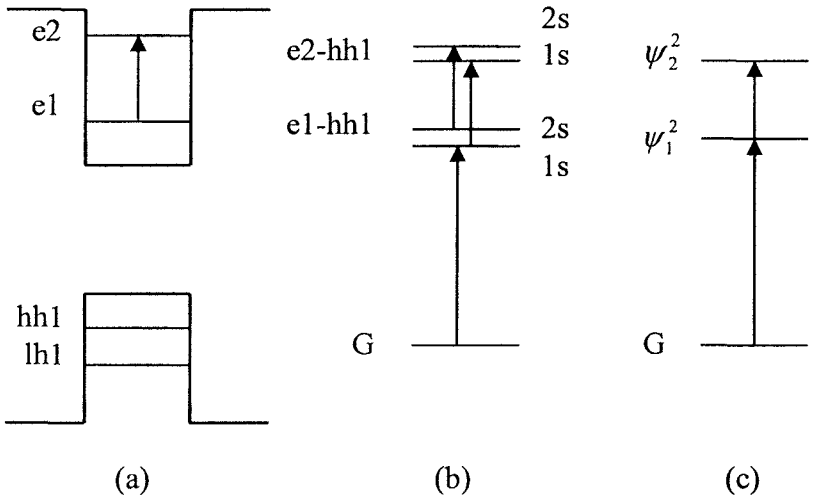

Figure 4-1 Schematic diagram of the intersubband transitions in an un-doped QW. (a) The electronic e1-e2 transition, (b) The transitions between pure s states of the excitons associated with e1 and e2, (c) The transition between mixed exciton states.

As demonstrated in [59], an important feature of PI ISTs in un-doped QWs is that although they happen as electrons are excited from one conduction subband (e1) to anther (e2) (Figure 4-1a), they are in fact the transitions between exciton states

associated with these subbands (e.g., from 1s, 2s of the e1-hh1 exciton to 1s, 2s of the e2-hh1 exciton, Figure 4-1b). In Figure 4-1b, however, the exciton states are associated with only one conduction subband and one valence subband. This is valid only when the valence subbands are well separated from each other. When the valence subbands are close to each other, for instance, in the cases of wide or properly strained QWs, the exciton states associated with individual valence subbands may mix together [61]. In the presence of such a mixing process the exciton states associated with the i th conduction subband will be represented as [61],[63]

$$\Psi_i^{\xi}(\mathbf{r}_e,\mathbf{r}_h)=\sum_j \Psi_{i,j}^{\xi,\beta}=\sum_{j,\mathbf{k}} \phi_{i,j}^{\xi,\beta}(\mathbf{k})\psi_i(\mathbf{k},\mathbf{r}_e)\psi_j(-\mathbf{k},\mathbf{r}_h), \qquad (4.1)$$

where $\Psi_{i,j}^{\xi,\beta}$ is the two-band exciton state associated with the i th conduction subband and j th valence subband. ξ is the total angular momentum along z direction (the growth direction) and β is the exciton index, i.e., 1s, 2p, and 3d. The mixed exciton state Ψ_i^{ξ} is characterized by the i th conduction subband and ξ. In contrast to $\Psi_{i,j}^{\xi,\beta}$ that represents pure s states or p states, etc. and has been discussed in Ref. [59], Ψ_i^{ξ} describes mixed states of s, p or d states associated with different valence subbands. Under the condition of state mixing, the PI ISTs associated with e1 and e2 (Figure 4-1a) are in fact happening between mixed states associated with these two subbands, i.e., from Ψ_1^2 to Ψ_2^2 (Figure 4-1c).

The exciton wave functions can be further written as product of three functions as the second equation in (4.1). $\psi_i(\mathbf{k},\mathbf{r}_e)$ and $\psi_j(-\mathbf{k},\mathbf{r}_h)$ are the electron and hole wave functions in quantum wells without Coulomb interaction. $\phi_{i,j}^{\xi,\beta}(\mathbf{k})$ is the exciton state function in momentum space that describes the relative movement between electrons and holes due to Coulomb attraction. The wave functions $\phi_{i,\mathbf{k}}(\mathbf{r}_e)$ and $\phi_{j,-\mathbf{k}}(\mathbf{r}_h)$ have been studied extensively before [30],[31]. As shown in equations (2.4) and (2.9), they can be expressed as product of the envelope function and Bloch function of electrons and holes. And as equation (2.5) shows that the wave function of one valence subband can have components of different spinors ν. The extent of spinor mixing in a subband can be characterized by the valence band mixing factor (VBMF) defined as

$$\Gamma_j^{\nu}(k) = \int dz g_{j,\nu}(k,z) g_{j,\nu}^{*}(k,z) \tag{4.2}$$

To study the effect of hole Coulomb mixing effects in the PI IST, we need to calculate the dipole moment associated with such transitions:

$$\mu_{ii'}^{\xi} = e\left\langle \Psi_i^{\xi} \middle| z \middle| \Psi_{i'}^{\xi} \right\rangle \tag{4.3}$$

To proceed with this calculation, we note that in (2.4) and (2.9), the azimuthally angular dependences of electron and hole wave functions are separated out and their envelope functions become function of scalar k only. Similarly, we can write the exciton envelope function as

$$\phi_{i,j}^{\xi,\beta}(\mathbf{k}) = e^{i\xi\theta}\varphi_{i,j}^{\xi,\beta}(k) \tag{4.4}$$

This allows us to write exciton states as

$$\Psi_i^{\xi} = \sum_j \Psi_{i,j}^{\xi,\beta} = \sum_j \sum_{\nu} F_{i,j,\nu}^{\xi,\beta}, \tag{4.5}$$

where

$$F_{i,j,\nu}^{\xi,\beta} = \int \frac{d\mathbf{k}}{(2\pi)^{3/2}} \varphi_{i,j}^{\xi,\beta} e^{i\mathbf{k}\cdot(\boldsymbol{\rho}_e - \boldsymbol{\rho}_h)} e^{i(\xi-\sigma-\nu)} f_i(z_e) u_c g_{j,\nu}(k, z_h) u_\nu \tag{4.6}$$

This equation shows $m = \xi - \sigma - \nu$. An exciton state as described by equation (4.1) can potentially has electron spinor of σ = –1/2, 1/2 and hole spinor of ν = –3/2, –1/2, 1/2, 3/2. Because of the total angular momentum conservation, however, only the combination giving the same ξ will be allowed. In fact in the presence of the hole Coulomb mixing effect, ξ is the only well-defined quantum number that can describe exciton states. We are interested in two representative states: ξ=2 state and ξ=0 state. We use the designation that at k = 0 heavy-hole subband HH1 has only ν=3/2 component and light-hole subband LH1 has only ν = –1/2 component, and choose σ as 1/2. Thus ξ=2 state associated with conduction subband e1 (i =1) can be written as

$$\Psi_1^2 = a\Psi_{1HH_1}^{2,s} + b\Psi_{1LH_2}^{2,p+}. \tag{4.7}$$

It consists of s state associated with HH1 and p^+ state associated with LH2. Similarly, ξ=0 state associated with conduction subband e1 (i=1) can be written as

$$\Psi_1^0 = a\Psi_{1LH_1}^{0,s} + b\Psi_{1HH_1}^{0,d-} + c\Psi_{1HH_2}^{0,p+} \tag{4.8}$$

This state consists of s state of LH1, d_- state of HH1, and p^+ state of HH2. Here a, b and c are the coefficients representing the contributions from different angular momentum components and will be determined by the quantum well structures.

Based on equations (4.3) and (4.5), the dipole moment associated with the PI ISTs can be written as follows:

$$\mu_{ii'}^{\xi} = \sum_{jj',\nu} \mu_{ii',jj',\nu}^{\xi,\beta} \tag{4.9}$$

where

$$\mu_{ii',jj',\nu}^{\xi,\beta} = e\left\langle F_{ij\nu}^{\xi,\beta} \middle| z_e \middle| F_{i'j'\nu}^{\xi,\beta} \right\rangle . \tag{4.10}$$

Here i,i' and j,j' are conduction and valence subbands indexes, respectively. Here i and i' have to be different to yield nonzero value. j and j', however, can be the same or different. For $j = j'$, we will obtain intersubband transitions between exciton states of same angular momentum such as s-s, p-p and d-d (diagonal components). For $j \neq j'$, however, the intersubband transitions can happen between exciton states with different angular momentum such as s-p, p-s, s-d and d-s (off-diagonal components). As discussed in the following, such

diagonal and non-diagonal components can happen simultaneously when a single infrared field near resonant with the transition between i and i' interacts with the QW structure. Compared to those considered previously, this could lead to a quite different picture for interaction of intense laser fields with quantum well structures.

4.3 From valance-band mixing to exciton-state mixing

As studied in [59],[60], the PI ISTs can be influenced by the dispersion of the valence subbands. In these references, however, this was studied considering s-states of the excitons only. In this chapter, we will show how the valence band structure affects PI ISTs through the mixed exciton states. The effects of the valence band mixing on the exciton states have already been studied before [22],[61]. Here we only give a brief account to illustrate their impacts on the PI ISTs.

Strong valence band mixing is the precondition for exciton state mixing to happen. At the band-edge (k=0), there is no band mixing. Here one valence subband can be characterized by a single spinor index ν, i.e., the first heavy-hole subband (hh1) by $\nu = 3/2$ and the first light-hole subband (lh1) by $\nu = -1/2$. Away from band-edge, both $\nu = \pm 3/2$ and $\nu = \pm 1/2$ spinors will be present in one subband. The degree of mixing of different spinors will be determined by how close the subbands are. The subband positions are characterized by band-edge

energies and can be effectively engineered through the introduction of strain by varying material composition. To study the PI ISTs, we focus on subbands hh1 and lh1 and examine how they interact with each other and with hh2 and lh2. The band-edge of these four subbands (k=0) of a 12-nm wide $In_{1-x}Ga_xAs/InP$ QW are plotted as a function of Ga composition (x) in Figure 4-2. Ga composition varies from 0.35 to 0.75, corresponding to compressive strain of 0.9% and tensile strain of 1.9%, respectively. (The range 0.35~0.75 is chosen for better illustration of the exciton mixing effects). Figure 4-2 shows that three crossovers happen for hh1 and lh1. At x=0.52 hh1 (solid line) crosses over with lh1 (dashed line), at x=0.68 with lh2 (dotted line). At x=0.47 lh1 crosses over with hh2 (short dashed line). Strong valence band mixings will happen around these crossovers.

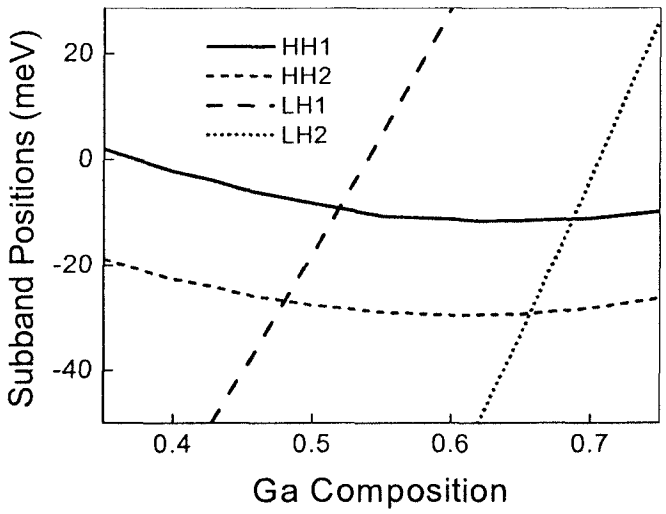

Figure 4-2 Subband positions of a 12 nm-wide $In_{1-x}Ga_xAs/InP$ QW for various Ga compositions

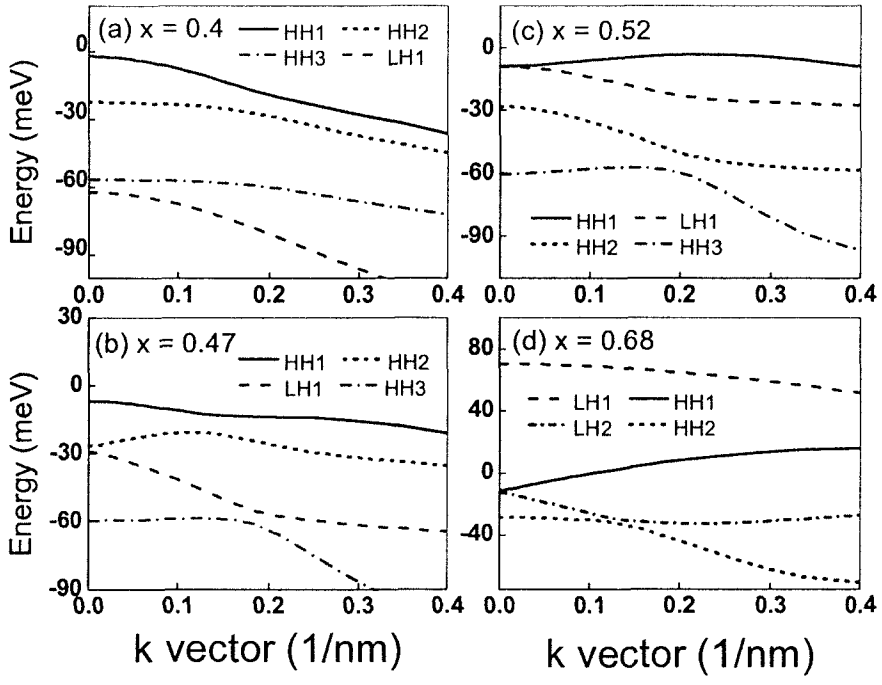

Figure 4-3 Valence band structure of 12nm InGaAs/InP quantum wells. (a) x = 0.4; (b) x = 0.47; (c) x = 0.52; (d) x = 0.68.

The dispersions of holes at these three compositions along with a non-crossover composition x = 0.4 are shown in Figure 4-3 ((a) x=0.4, (b) x=0.47, (c) x=0.52, (d) x=0.68). At x = 0.4, two neighboring subbands are far from each other and the dispersion curves are mainly parabolic (Figure 4-3a). This shows that valence band mixing is weak. At x = 0.47, 0.52, 0.68, the subbands of interest, hh2 and lh1 in Figure 4-3b, hh1 and lh1 in Figure 4-3c, hh1 and lh2 in Figure 4-3d, are very close to each other. The dispersion curves of these subbands

become strongly nonparabolic and nearly degenerate around the zero in k-space. This demonstrates that strong valence band mixings happen around these values.

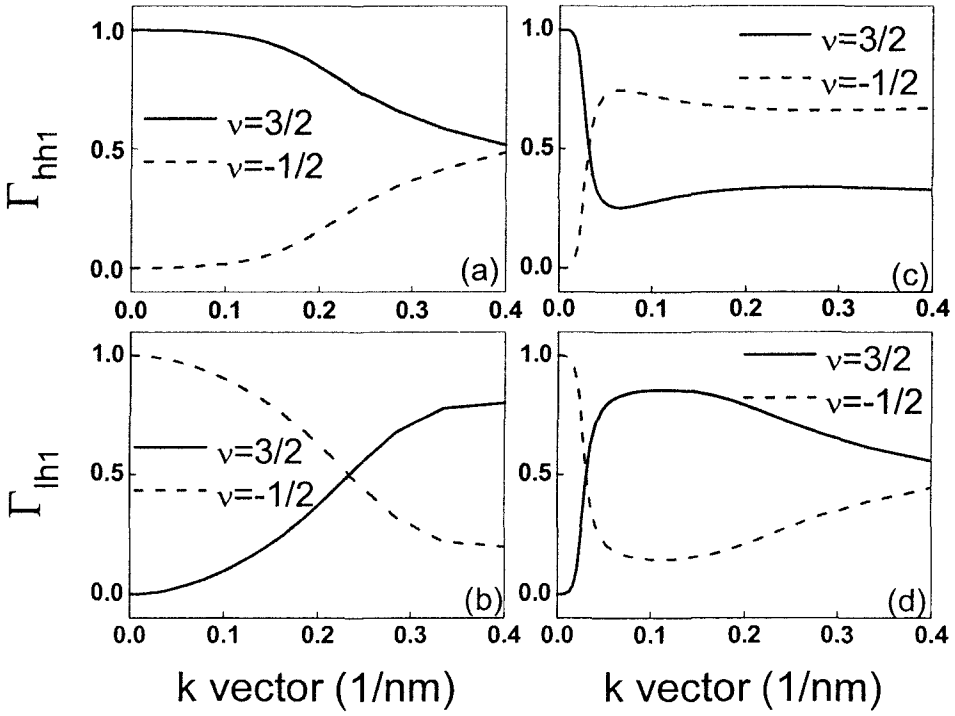

Figure 4-4 Valence band mixing factor of 12nm InGaAs/InP quantum wells. (a) x = 0.4, hh1; (b) x = 0.4, lh1; (c) x = 0.52, hh1; (b) x = 0.52, lh1.

Nonparabolic dispersions can be related to spinor mixing of the valence bands that is characterized by the valence band mixing factor Γ_j^{ν} defined in (4.2). The VBMF at x = 0.4 are shown in Figure 4-4a for hh1 and Figure 4-4b for lh1 (solid line: ν=3/2; dashed line: ν = –1/2). VBMF at x = 0.52 are shown in Figure

4-4c for hh1 and Figure 4-4d for lh1 (solid line: $\nu = 3/2$; dashed line: $\nu = -1/2$). We are interested in the region close to zero in k-space, where the exciton wave functions are mostly extended. For x = 0.4, the region is dominated by the contribution of $\nu = 3/2$ for hh1 and $\nu = -1/2$ for lh1, respectively. For x = 0.52, the contributions of $\nu = 3/2$ and $\nu = -1/2$ are both present in hh1 and lh1. In other words, the valence bands are strongly mixed. We will show in the following that such a mixing plays a crucial role in PI ISTs.

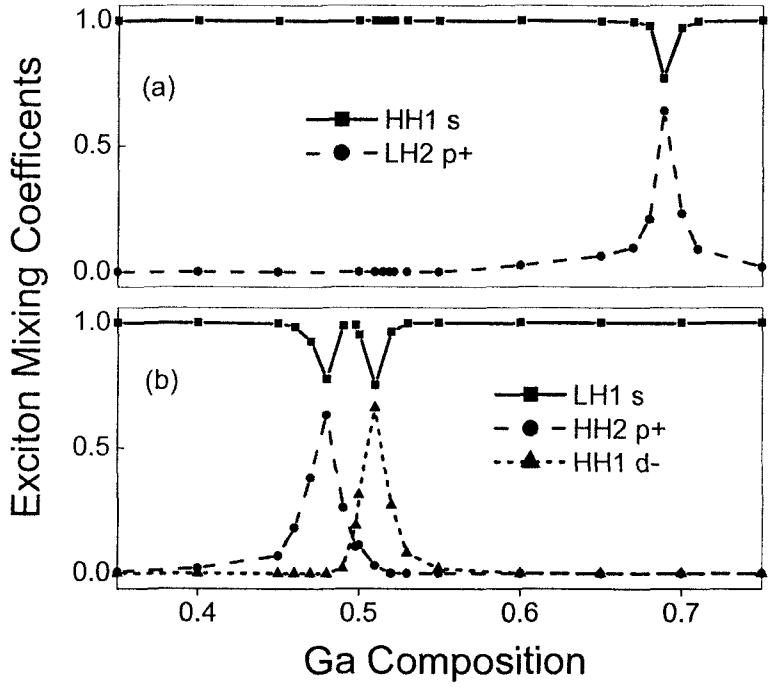

Figure 4-5 Exciton state mixing coefficients: a. ξ=2, i=1; b. ξ=0, i=1

To quantitatively study how such valence band mixings influence the exciton states, we calculate the exciton state mixing coefficients in equations (4.7) and (4.8). The coefficients for the first state of ξ=2 and i=1 (Ψ_1^2) are plotted as function of Ga composition in Figure 4-5a. For x away from 0.68, the exciton state is mostly s state associated with hh1 subband, and around x=0.68 exciton states are mixture of s state of hh1 (squares) and p^+ state of lh2 (filled circles). As shown in Figure 4-2, x=0.68 is the crossover point of hh1 and lh2, demonstrating that strong exciton state mixing occurs under the condition of strong valence band mixing. It is also interesting to note that there is no exciton state mixing around crossover x=0.52 even though strong band mixing of hh1 and lh1 happens there. This is because the exciton state mixing also requires the conservation of total angular momentum of exciton states (ξ). For the ξ=2 state, s state of hh1 cannot mix with any excitonic states of lh1 due to the angular momentum conservation. Similarly, the exciton state mixing coefficients of the first state of ξ=0 and i =1 (Ψ_1^0) are calculated as a function of Ga composition and plotted in Figure 4-5b. For x<0.47 and x>0.52, the exciton states are primarily s states associated with lh1 (squares). Around x=0.47 exciton states are strong mixture of s state of lh1 and p^+ state of hh2 (filled circles). And around x=0.52 exciton states are strong mixture of s state of lh1 and d_- state of hh1 (filled triangles). Around 0.49~0.50, the center region between x=0.47 and x=0.52, the exciton states can be viewed as

the mixture s state of lh1, d_- state of hh1, d and p^+ states of hh2 although the last two components are small.

4.4 Exciton-state mixing in intersubband transitions

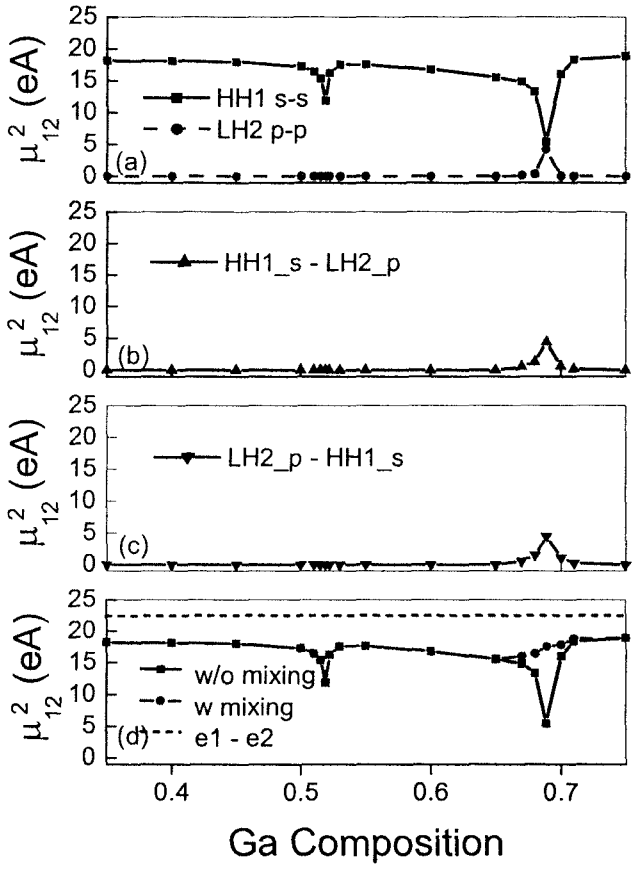

Figure 4-6 Dipole moments associated with the transitions between Ψ_1^2 and Ψ_2^2. (a) represents the s-s, p-p; (b) the s-p and (c) the p-s transitions. (d) with and without exciton state mixing

To investigate the photo-induced conduction intersubband transitions under exciton state mixing, the dipole moment contributions of various angular momentum components have been calculated for the 12-nm $In_{1-x}Ga_xAs/InP$ QW. In Figure 4-6, the dipole moments of PI ISTs from the first state of Ψ_1^2 to the first state of Ψ_2^2 are plotted as functions of Ga composition. Here squares correspond to the s-s (Figure 4-6a); circles to the p-p (Figure 4-6a); up-triangles to the s-p (Figure 4-6b), and down-triangles to the p-s transitions (Figure 4-6c). The overall dipole momentums obtained from the models without and with exciton state mixing are compared in Figure 4-6d. Here squares correspond to that without exciton mixing which is essentially the s-s transition in Figure 4-6a and circles to that with exciton mixing which is the summation of all angular momentum contributions. Away from x=0.52 and x=0.68, the dipole moment is primarily the contribution from s to s transition (see squares and circles in Figure 4-6d). At x=0.52 and x= 0.68 the s-s transition is suppressed. This is because the strong valence band mixings around these two points result in the reduction of $\nu = 3/2$ components in hh1 that are associated with s states of e1-hh1 and e2-hh1. The suppression has been discussed in [59]. But our results show that, accompanying with the suppression of s component at x=0.68, there are contributions from the p state and its cross terms with s state. These transitions have not been previously accounted for and make up the loss of transition strength due to the reduction of s component at this x composition. We can also notice that the non s-s terms do not

appear at x=0.52, because there is no mixing for the s states of exciton associated with hh1 due to the requirement of angular momentum conservation, as explained before. Finally, the dipole moments of the electron transitions between conduction subbands e1 and e2 are also plotted in Figure 4-6d (dashed lines). Such transitions occur in n-doped QWs in the absence of photo-excited holes. We can see here that the exciton dipole moment is a little off from the electron dipole moment in most of regions. Around x=0.52, the PI ISTs strength will be significantly overestimated if the electron transition model is used.

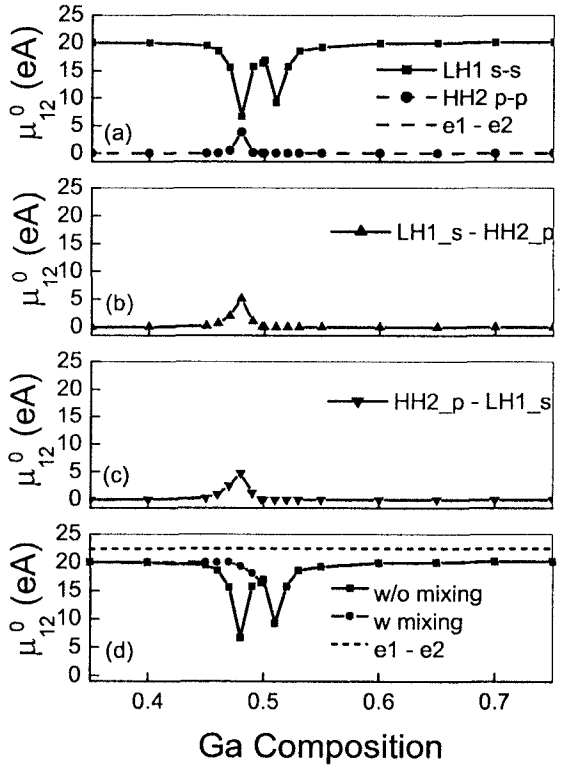

Figure 4-7 Dipole moments associated with the transitions between Ψ_1^0 and Ψ_2^0. (a) represents the s-s, p-p; (b) the s-p and (c) the p-s transitions. (d) with and without exciton state mixing

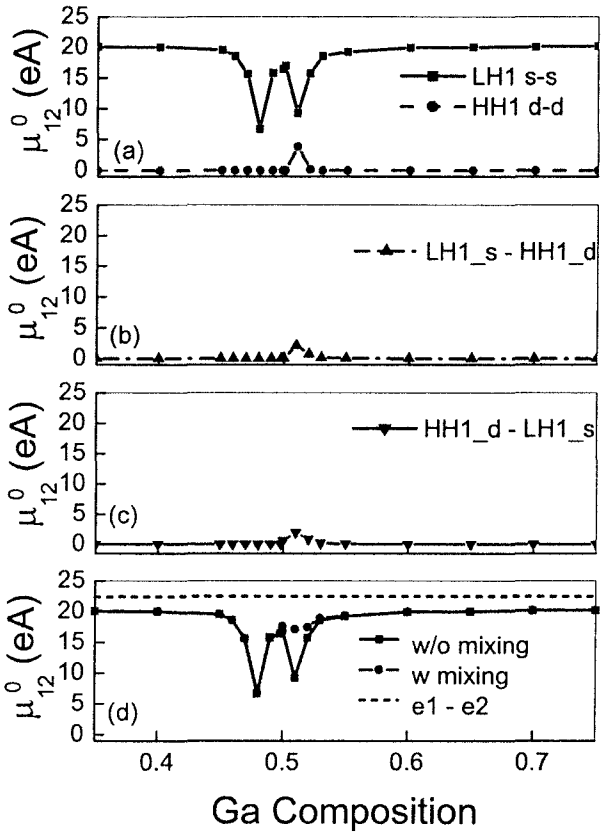

Figure 4-8 Dipole moments associated with the transitions between Ψ_1^0 and Ψ_2^0. (a) represents the s-s, d-d; (b) the s-d and (c) the d-s transitions. (d) with and without exciton state mixing

The dipole momentums of PI ISTs from the first state of Ψ_1^0 to the first state of Ψ_2^0 are plotted in Figure 4-7 and Figure 4-8 as a function of Ga

composition. These figures show, respectively, the results of s-p and s-d mixing in the dipole moments of the PI ISTs. and comparisons between the dipole moments without and with exciton state mixing are shown in Figure 4-7d and Figure 4-8d. Similar to the case of ξ=2 excitons, away from the two strong valence band mixing points x=0.47 and x= 0.52, the dipole moment has primarily contribution from s-s transitions. At x=0.47 the p-p, p-s, and s-p transitions and at x=0.52 the d-d, d-s and s-d transitions become significant. At x=0.47 and x=0.52, the model without exciton mixing will significantly underestimate the PI ISTs strength. The dipole moments of the electron transitions are also plotted in Figure 4-7d and Figure 4-8d (dashed line) as a comparison.

4.5 Conclusions

In summary, we have shown that, when the exciton state mixing occurs, an infrared laser near resonant with conduction subbands e1 and e2 can in fact lead to intersubband excitations with different angular momentum attributions. This may lead to drastically different picture for interaction of intense infrared lasers with QWs from that when no exciton effects or only s states excitons are considered. We have also shown that the dipole moments of PI ISTs could be drastically suppressed when strong valence band mixing happens but the exciton ground states remain pure s states. Our results also show that much of the drastic

suppression previously predicted considering only the s states of excitons, however, will be compensated by the contributions of other orbital angular momenta.

The above results are important for the design of optical wavelength converters [57],[64],[65] that utilize intersubband transition to enhance the interband optical nonlinearity. Since intersubband transitions are also the backbone of mid- and far-infrared lasers [66], modulators [67], detectors [68], etc., an accurate model to account for the transition strength can be also useful in the design of those devices.

In addition, the exciton mixing effects discussed in this chapter can have impacts on the way PI ISTs are being used to interpret various physical processes in QWs. In general, intersubband transitions between quantized states of low-dimensional quantum structures have been widely used to study relaxation processes, electronic states, carrier-carrier scattering, etc. in quantum wells (QWs), wires, and dots. They are particularly appealing for investigation of coherent optical processes. Some of these effects include electromagnetically-induced transparency [65], coherent population trapping [69], gain without inversion [70], and Rabi flopping [71]. Moreover, characteristic properties, such as relaxation processes, electron-hole interaction, and carrier multiplication in nanocrystals have been widely investigated using intersubband transitions. [72].

Chapter 5

Exciton Capture and Escape in Quantum Wells

5.1 Introduction

The carrier capture and escape processes in quantum wells are important to the speed and optical nonlinearity of EA modulators. In general, the electron and hole transports into and out of semiconductor quantum well (QW) structures are the fundamental physical processes that define many critical characteristics of optoelectronic devices. The carrier capture into such structures determines the efficiency and operation speed of QW lasers and amplifiers [73]. The carrier escape out, on the other hand, affects absorption saturation of the electro-absorption (EA) based nonlinear devices such as optical switches and wavelength converters [3]. Such a process also determines the dark current of QW infrared photo-detectors [68] and the short circuit current of QW solar cells [74].

The carrier capture and escape in QWs have been studied extensively using various experimental techniques and theoretical models [75]~[78]. Excitonic nature of these processes has also been investigated [76]~[78]. It has been shown that the Coulomb correlation between electrons and holes plays an important role in the time scales of these processes. The previous studies, however, are based on the hole band structure model that do not include valence band mixing [76]. In other words, the hole subband dispersions are simply assumed to be parabolic functions characterized by the effective masses defined by the Luttinger parameters. It is well known that, however, valence band mixing may introduce a considerable modification to the hole band structure. Thus one expects that valence band mixing may have impacts on the exciton capture (or escape) processes. In this chapter we will address this issue and show that the inclusion of such mixing can lead to exciton capture and escape times significantly different from those obtained assuming simple parabolic dispersions. Quantitatively our results show that the capture and escape times can be one order of magnitude smaller than previously reported. We will also discuss the impacts of the much faster capture and escape processes due to band mixing on various device characteristics.

To study band mixing effects on exciton capture and escape we consider here shallow QWs with separate confinement hetero-structures. Such structures are important for ultra-fast optoelectronic device applications [79]. Additionally,

since valence band mixing can also happen in other quantum structures, including deep quantum wells, quantum wires and quantum dots, the results presented in this chapter can also be useful for understanding the exciton-phonon scattering processes in such structures [80],[81].

In the following, we will start with the formulations of the exciton states under band mixing and the exciton capture and escape in the QW. And then present and discuss the simulation results.

5.2 Hole Effective Mass in Excitons

The QW structure considered here is schematically shown in Fig. 1. A single quantum well with width l_{QW} is sandwiched in two separate confinement hetero-structure (SCH) layers with the total width of the QW and two SCH regions l_{SCH}. The material system is $GaAs/Al_xGa_{1-x}As$. Al composition is a few percent so that barrier height is comparable to the longitudinal optical (LO) phonon energy (~36 meV). The excitons in the QW will be confined along the QW growth direction and are quasi two-dimensional (2D). The SCH width l_{SCH} will be considerably larger than Bohr radius of $Al_xGa_{1-x}As$ bulk material. Thus the excitons in SCH regions can be treated as three-dimensional (3D) bulk excitons. We will consider the exciton capture from SCH to QW and the escape from QW

to SCH. The capture and escape are through interaction with LO phonons, which are assumed 3D phonons in our analysis.

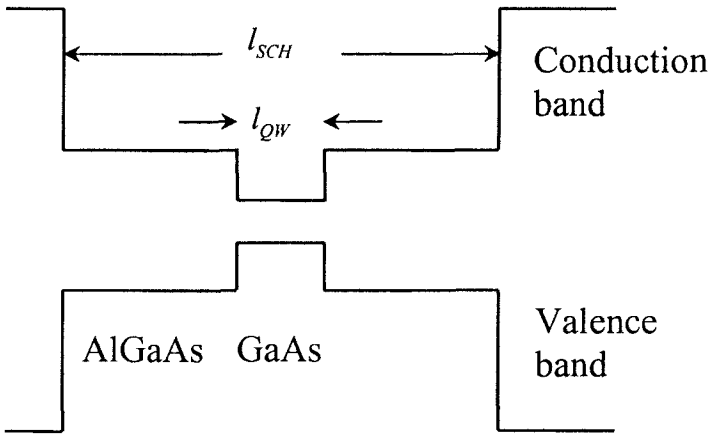

Figure 5-1 Band-edges of the separate confinement hetero-structure quantum well

The exciton states in the QW can be expressed as

$$\Psi_{ij}^{\xi} = f_i(z_e)g_j(z_h)\phi_{ij}^{\xi}(\mathbf{K},\mathbf{k}), \tag{5.1}$$

where f_i and g_j are the wave functions along the growth direction (z) for the i th conduction subband and the j th valence subband, respectively. $\phi_{ij}^{\xi}(\mathbf{K},\mathbf{k})$ is the exciton state function in momentum space, representing the exciton wave functions in the plane perpendicular to the growth direction. $\mathbf{K}$ is the wave vector associated with the center-of-mass of excitons and $\mathbf{k}$ is the wave vector associated with the relative movement of excitons. ξ is the exciton state index,

i.e., 1s, 2p, and 3d. In momentum space representation valence band mixing can be naturally incorporated into the exciton state equation.

Most significant band mixing happens between the heavy-hole and light-hole subbands, which can be described by Luttinger-Kohn Hamiltonian in the QW as [30]

$$H = \frac{\hbar^2}{2m_0}\begin{pmatrix} (\gamma_1+\gamma_2)k^2 - (\gamma_1-2\gamma_2)\nabla_z^2 & \widetilde{R} \\ \widetilde{R}^{+} & (\gamma_1-\gamma_2)k^2 - (\gamma_1+2\gamma_2)\nabla_z^2 \end{pmatrix}. \qquad (5.2)$$

Here γ_1, γ_2 are the Luttinger parameters. k is the in-plane wave vector. The off-diagonal term $\widetilde{R}$ represents the band mixing and its detail expressions can be found in [30]. Equation (5.2) shows that, without band mixing, the in-plane energy-momentum dispersions of the heavy-hole and light-hole subbands will be the parabolic functions characterized by effective masses $1/(\gamma_1+\gamma_2)$ and $1/(\gamma_1-\gamma_2)$, respectively. It also indicates that, with band mixing, the energy-momentum dispersions can be modified considerably.

The exciton states function $\phi_{ij}^{\xi}(\mathbf{K},\mathbf{k})$ can be obtained solving the equation as follows [81]

$$[E_i^e(\mathbf{k}_e) + E_j^h(\mathbf{k}_h) - E_{ij}^{\xi}(\mathbf{K})]\phi_{ij}^{\xi}(\mathbf{K},\mathbf{k}) + \int d\mathbf{k}' V_{ij}^{\mathrm{K}}(\mathbf{k},\mathbf{k}')\phi_{ij}^{\xi}(\mathbf{K},\mathbf{k}') = 0. \qquad (5.3)$$

Here V_{ij}^{K} refers to the Coulomb potential between the i th conduction subband electrons and the j th valence subband holes. E_{ij}^{ξ} is the exciton energies. E_i^e is

the energies of conduction band electrons and E_j^h those of valence band holes. Strictly speaking, exciton state mixing will occur when valence band mixing is present. However, Equation (5.3) does not include exciton state mixing because its effect will be very small in the situations we will consider such as the ground state asscocaited with HH1 [82].

Equation (5.3) is different equation (2.13) in Chapter 2. To study the optical absorption of exciton or exciton-photon interaction, the total momenta of the excitons are usually considered as zero due to the relatively small photon momentum. As a result, we only need to solve the exciton equation governing the relative part of the exciton wave functions. In considering the exciton-phonon interaction, the total exciton momentum cannot be ignored. Thus in principle, Equation (5.3) needs to be solved for every $\mathbf{K}$. But we can first solve Equation (5.3) for the case of $\mathbf{K} = 0$ and define the effective mass of the hole in an exciton at the ground state as [82]

$$\frac{1}{m_h^g} = \frac{1}{\hbar^2} \int d\mathbf{k} \left|\phi_{ij}^g(0,\mathbf{k})\right|^2 \frac{d^2 E_j^h(\mathbf{k})}{d\mathbf{k}^2}. \tag{5.4}$$

Here ϕ_{ij}^g is the ground state envelope function of the exciton. At $\mathbf{K} = 0$, $\mathbf{k}_e = -\mathbf{k}_h = \mathbf{k}$, so we have only one wave vector in equation (5.4). Based on equation (5.4), the effective masses are weighted averages of the second derivative of the energy-momentum dispersion over the square of the exciton state

function in momentum space. Using this equation we can in fact approximate the non-parabolic hole dispersion under band mixing with a parabolic one. Note that such an effective mass is different from that defined by the Luttinger parameters, i.e., $1/(\gamma_1+\gamma_2)$ for the heavy hole.

It is well known that when holes have parabolic dispersion the exciton state functions can be written as separable functions of the center-of-mass and relative coodinates. Similarly, based on equation (5.4), effective masses of the holes are considered here k-independent. This allows us to write the exciton state function under band mixing as:

$$\Psi_{ij}^{\xi} = \Phi(\mathbf{K})\phi_{ij}^{\xi}(\mathbf{k})f_i(z_e)g_j(z_h). \tag{5.5}$$

For convenience, we convert momentum space function into real space function through two-dimensional Fourier transform as [76]

$$\Psi_{ij}^{\xi} = \frac{1}{l_{\|}} e^{i\mathbf{K}\mathbf{R}}\phi_{ij}^{\xi}(\boldsymbol{\rho})f_i(z_e)g_j(z_h). \tag{5.6}$$

Here $\mathbf{R}$ is the coordinate of the center-of-mass of excitons and $\boldsymbol{\rho}$ is the coordinate of the relative movement of excitons. $l_{\|}$ is the in-plane sample length.

Equation (5.6) describes the bound states of the excitons in the QW. For the continuous states of excitons, if we neglect the Coulomb correlation between

electrons and holes, they can be described as free in-plane electron-hole pairs, confined along z direction as

$$\Psi_{ij}^{cont} = \frac{1}{l_{\|}} e^{i\mathbf{k}_e \boldsymbol{\rho}_e} \frac{1}{l_{\|}} e^{i\mathbf{k}_h \boldsymbol{\rho}_h} f_i(z_e) g_j(z_h). \tag{5.7}$$

The excitons in SCH regions will be of three-dimensional nature and the ground state of 3D excitons can be represented by

$$\Psi_{3D}^{1s} = N_{3D} \phi_{3D}^{1s}(r_{3D}) \frac{1}{l_{\|}} e^{i\mathbf{K}\mathbf{R}} \cos(\frac{\pi Z}{l_{SCH}}) \tag{5.8}$$

Where $\phi_{3D}^{1s}(r_{3D})$ represent the 1s state envelope functions of bulk excitons. The in-plane movement of center-of-mass is described by a plane wave. And the confinement of SCH along the z-direction is described by the cosine term. The subscript 3D is used to differentiate the coordinate r_{3D} from $\mathbf{R}, \boldsymbol{\rho}$ that are defined in 2D plane. N_{3D} is the normalization constant. The initial states in equation (5.8) do not take into consideration the potential discontinuity in the QW region and therefore only apply to shallow QW structures. Unlike the case of 2D excitons, here we do not consider the continuous states of 3D excitons. 3D Excitons in the continuous state are equivalent to free 3D electrons and holes. The simultaneous capture from (or escape to) free 3D electrons and holes are much slower processes than those related to the states described above in equations (5.6) and (5.7).

5.3 Exciton Capture and Escape

The transition rates of the 3D exciton states and 2D exciton states can be calculated based on the Fröhlich Hamiltonian of exciton-phonon interaction and Fermi's Golden rule. The transition rates between the bound states of 3D excitons and the bound states of 2D excitons can be given by [76]

$$P = \frac{e^2\hbar\omega_{LO}M_{\parallel}(n_q + \frac{1}{2} \pm \frac{1}{2})}{4\hbar^3\varepsilon_0\varepsilon_p q_{\parallel}} |\Gamma_e I_e(q_{\parallel}) - \Gamma_h I_h(q_{\parallel})|^2 \tag{5.9}$$

Here $1/\varepsilon_p = 1/\varepsilon_\infty - 1/\varepsilon_0$ with $\varepsilon_\infty, \varepsilon_0$ dielectric constants at very high and very low frequencies, respectively. n_q is the phonon occupation number given by $n_q = [e^{\hbar\omega_{LO}/k_BT} - 1]^{-1}$. The plus sign is for the capture from the 3D excitons (equation (5.8)) to 2D excitons (equation (5.6)) and the minus is for the reverse exciton escape. The in-plane integral factors are given by

$$I_{e,h}(q_{\parallel}) = 2\pi \int_0^{\infty} \rho\phi_{3D}^{1s}(\rho,0)\phi_{ij}^{\xi}(\rho)J_0(a_{h,e}q_{\parallel}\rho)d\rho, \tag{5.10}$$

$$M_{\parallel} = m_{\parallel}^{e} + m_{\parallel}^{h}, \quad a_{e,h} = \frac{m_{\parallel}^{h,e}}{M_{\parallel}}. \tag{5.11}$$

Where $m_{\parallel}^{e,h}$ is the in-plane effective mass of electrons and holes. For the electrons it is simply their bulk effective mass. For the holes it is given by equation (5.4). The effects of band mixing on exciton capture and escape will be incorporated through the effective masses and the ratios in equation (5.11). In

equation (5.10), the in-plane distributions of 3D exciton wave functions $\phi_{3D}^{1s}(r_{3D})$ in the QW region are considered as its distribution at z = 0 plane $\phi_{3D}^{1s}(\rho,0)$. Strictly speaking this is only valid when the 3D Bohr radius is much larger than the QW width. For structures considered here, however, the 3D exciton wave function in the quantum well region may fall off to 50% of this peak value at z = 0. Therefore, considering the in-plane distribution in the QW region as same as that at z = 0 will overestimate the integral in equation (5.10) by about 20~30%. Note that the same approximation has been utilized in the previous treatments [76] in which valence band mixing is not included. With the same approximation here we study how valence band mixing relatively influences the capture/escape rate. Also, the relative difference of capture/escape rates is quite large as will be shown later. The above approximation should be justifiable. $q_{\|}$ is the in-plane phonon momentum and is given by

$$\frac{\hbar^2 q_{\|}^2}{2M_{\|}} = (E_{3D}^{1s} - E_{2D}^{1s}) - \hbar\omega_{LO}. \tag{5.12}$$

Here we have considered the initial states with zero kinetic energy. $\hbar\omega_{LO}$ is the LO phonon energy and can be taken as constant. E_{3D}^{1s} and E_{2D}^{1s} are the energy of 3D excitons and 2D excitons, respectively. $q_{\|}$ will be determined by the difference of E_{3D}^{1s} and E_{2D}^{1s} which in turn are determined by the QW width and the barrier height. The barrier height is determined by Al composition of $Al_xGa_{1-x}As$.

The dependence of the capture and escape rates on the QW width and barrier composition are studied through the phonon momentum $q_{\parallel}$. The z-direction integral factors $\Gamma_{e,h}$ are given by

$$\Gamma_{e,h} = \int_0^{\infty} dz_{e,h} \Psi_{3D}^{1s}(z_{e,h}) \chi_{e,h}(z_{e,h}) e^{iq_z z_{e,h}}, \tag{5.13}$$

where $\chi_{e,h}$ represents f_i and g_j in equation (5.1).

The capture rates between the bound states of 3D excitons (equation (5.8)) and the continuous states of 2D excitons (equation (5.7)) are given by [76]

$$P = \frac{e^2 \hbar \omega_{LO} m_{\parallel}^h (n_q + 1)}{4\hbar^3 \varepsilon_0 \varepsilon_p} \int_0^{k_e^{\max}} \frac{k_e}{k_e + k_h} K\left(\frac{4k_e k_h}{(k_e + k_h)^2}\right) \left|\Gamma_e I_e(k_h) - \Gamma_h I_h(k_e)\right|^2 dk_e \tag{5.14}$$

Where K is the complete elliptic integral of the first kind. The in-plane integral factors are given by

$$I_{e,h}(k_{e,h}) = \frac{\lambda_{3D}}{[1 + (\lambda_{3D} k_{e,h})^2]^{3/2}}, \tag{5.15}$$

where λ_{3D} is the effective Bohr radius of the 3D excitons. k_e, k_h are the in-plane momenta of the electrons and holes, respectively. They are given by

$$\frac{\hbar^2 k_e^2}{2m_e} + \frac{\hbar^2 k_h^2}{2m_h} = E_{3D}^{1s} - (E_{gap}^{QW} + E_e + E_h) - \hbar\omega_{LO}. \tag{5.16}$$

Where E_e and E_h are the first energy levels of the electron and the hole in quantum well, respectively. Given a quantum well structure, E_e and E_h will be fixed and so is the total kinetic energy. But unlike in equation (5.12) where one

kinetic energy corresponds one in-plane momentum of bound excitons ($q_{\|}$), one kinetic energy here in equation (5.16) corresponds to a set of combination of electron and hole momentum. This is why we have an integration over electron momentum in equation (5.14).

5.4 Results and Discussions

To investigate valence band mixing effects in exciton capture and escape, we first study how variation of the Al content of the GaAs/$Al_xGa_{1-x}As$ QW structure considered here affects valence band mixing and, therefore, the effective masses of the holes in the excitons. We then calculate the capture and escape times.

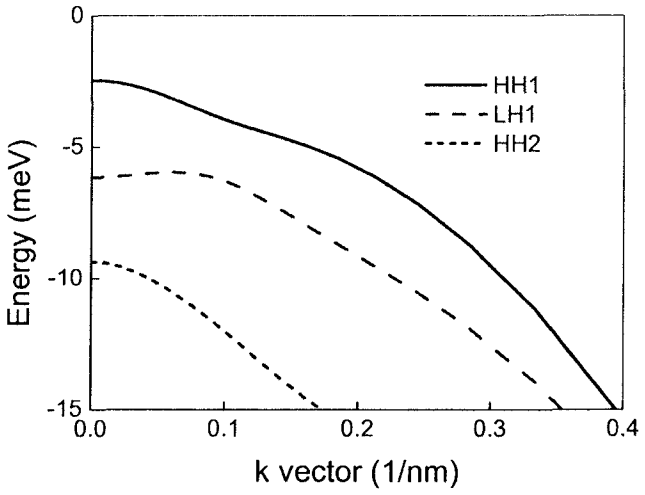

Figure 5-2 Valence band structure: 15nm, 4%Al, GaAs/ $Al_xGa_{1-x}As$ quantum well

The valence band structures of a typical shallow $GaAs/Al_xGa_{1-x}As$ quantum well with 15-nm width and 4% Al composition have been calculated (Figure 5-2). Since the ground state is of most interest, we will study the 1s state of the exciton associated with HH1.

The heavy-hole effective masses associated with the 1s states of HH1 excitons are calculated for a narrow (L=5 nm) and a wide (L=15 nm) QW. The results are plotted in Figure 5-3 as function of Al composition. The dashed line is for the 5-nm wide QW and the dotted line for the 15-nm wide QW. Solid line is $1/(\gamma_1+\gamma_2)$, the effective mass without band mixing considered by others [76]. Figure 5-3 clearly shows that band mixing results in larger effective mass. We can see the smaller the Al composition, the shallower the QW, and eventually the larger the hole effective mass. We can also see the wider well, the larger effective masses. This can be related to the fact that in both of these cases, the shallower and wider QW, the heavy-hole and light-hole subbands are closer to each other, resulting in stronger band mixing.

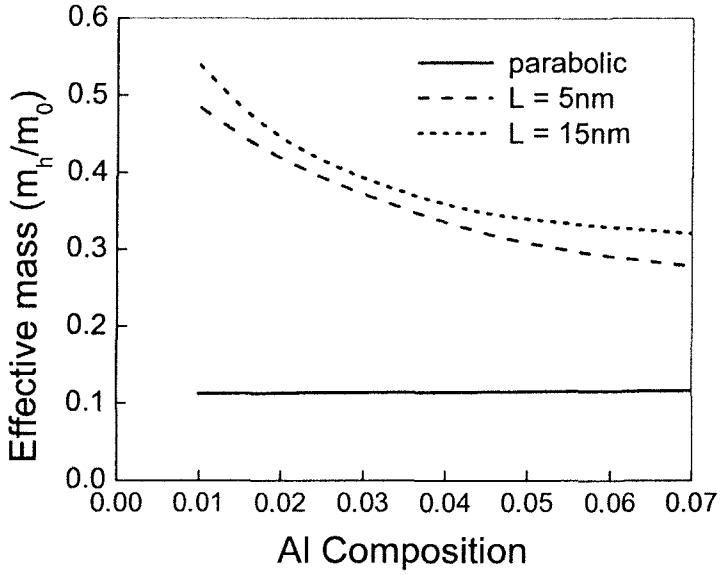

Figure 5-3 Effective mass of holes under band mixing (in unit of free electron mass). The solid line refers to the case where band mixing is ignored.

To see the impacts of the effective mass on exciton capture, we calculate the capture time using both the parabolic (Luttinger parameters based effective mass) and the band mixing models (equation (5.4) based effective mass) for the 15-nm wide QW at temperature 150 K. Two types of capture have been considered: one is from 1s state of 3D HH exciton into 1s state of the HH1 exciton and another from 1s state of 3D HH exciton into the continuous states of the HH1 exciton. The results are shown in Figure 5-4 as function of Al composition. The solid line (parabolic model) and dashed line (mixing model) are for the 1s state capture. The dotted line (parabolic model) and dot-dashed line

(mixing model) are for the continuous state capture. We first observe that, compared to the parabolic model, the capture time for 1s-1s capture is one order of magnitude faster when band mixing is included. This is a significant result that can be understood by considering the physical mechanism of the phonon-exciton scattering process. The strength of such scattering processes is determined by equation (5.9). There are three terms in equation (5.9) that vary with the QW structure or depend on the calculation model. In the following we will examine these terms one by one, especially their relationship with the effective mass of the hole.

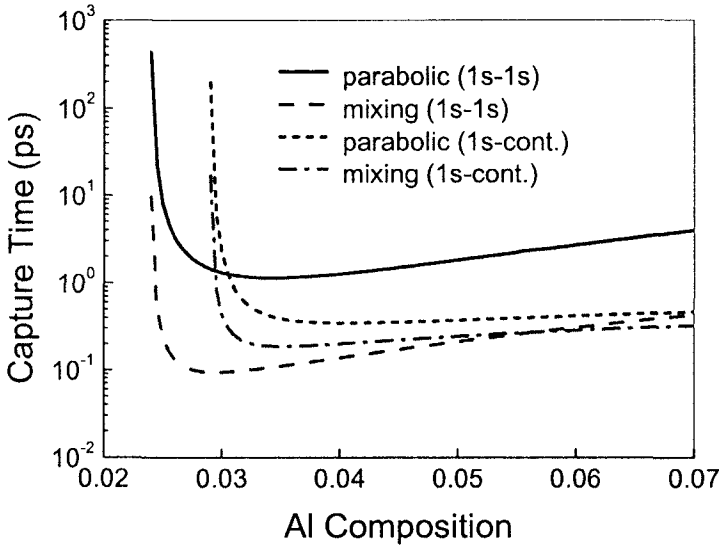

Figure 5-4 Capture times from 3D 1s state to 2D 1s state and to 2D continuous states

The first term is the interaction matrix element that is represented by the integral terms in equation (5.9). It is determined by the square of the difference between the electron and hole integrals in the equation. To better illustrate the role played by the matrix element, we have calculated $I_e - I_h$, ignoring the difference of Γ_e and Γ_h. The results are plotted as functions of the normalized $q_{\parallel}$ in Figure 5-5. For a typical shallow quantum well with 15-nm width and 4% Al composition in the barrier, the value of the normalized $q_{\parallel}$ will be 3.8 for the parabolic model and 5.8 for the band mixing model. We can see the value of the integral difference of the band mixing model (marked as diamond in Figure 5-5b) is about 3 times of that of parabolic model (marked as diamond in Figure 5-5a). For the 15-nm wide and 4% Al QW structure, however, the hole effective mass of the band mixing model is 3 times that of the parabolic model. Therefore roughly speak, the matrix elements is quadratically dependent on hole effective mass ($\propto m_h^2$). We also note for a given structure $q_{\parallel}$ is smaller for the parabolic model than for the band mixing model. This leads us to consider the second term in equation (5.9) that represents the role of phonon momentum in exciton capture. Equation (5.9) states that the capture rate is inversely proportional to in-plane phonon momentum ($1/q_{\parallel}$). From equation (5.12) we know that $q_{\parallel} \propto M_{\parallel}^{1/2}$, where $M_{\parallel} = m_{\parallel}^e + m_{\parallel}^h$ with $m_{\parallel}^e < m_{\parallel}^h$. Thus we can infer approximately that the dependence of capture rate on hole effective mass through the phonon momentum

term goes as $\propto m_h^{-1/2}$. Finally we note that there is a term $M_{\|}$ in equation (5.9). Combining all these three terms together, we can conclude that the capture rate is critically dependent on hole effective mass as $\propto m_h^{2.5}$. Therefore, band mixing can significantly change the capture rate by modifying the hole effective mass.

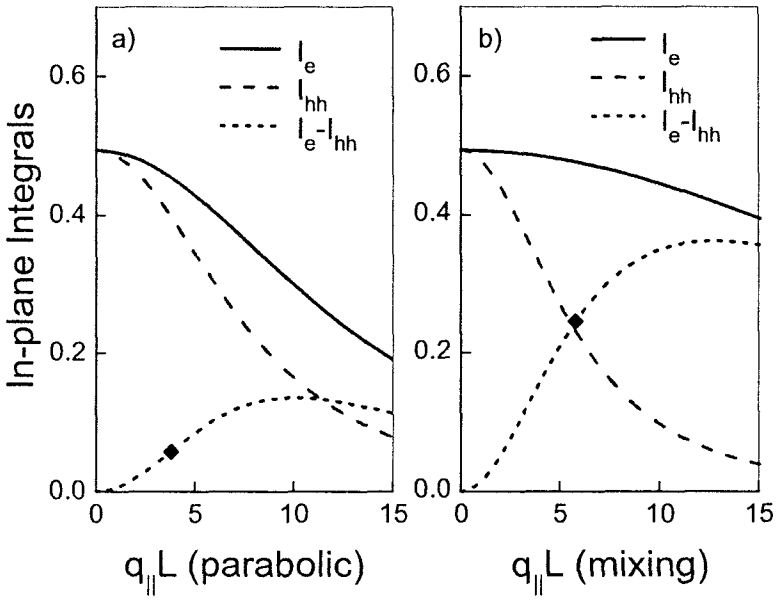

Figure 5-5 In-plane interaction integrals as functions of normalized in-plane phonon momentum for the 15-nm wide QW. The diamonds marks the integral values of 4% Al quantum well. They correspond to different normalized momentum values in parabolic model and band mixing model due to different effective mass of hole

Regarding the capture times of the 1s states of the 3D excitons into the continuous states of the HH1 excitons (dotted line for parabolic model and dot-

dashed line for mixing model in Fig.4), we found that the times obtained by the mixing model are smaller than those calculated using the parabolic model. The difference, however, is much less than the case of the 1s-1s capture. In the 1s-1s capture, electrons and holes are bound together by the Coulomb interaction and therefore they coherently interact with lattice/phonons. The net strength of the interaction critically depends on the ratio of effective masses as just discussed. In the case of the continuous states capture, however, the final state electron and hole do not need to move together. The impacts of effective mass will manifest through other factors such as the density of states and the partition of the total kinetic energy that are implicitly included in equation (5.14) and are not as significant as in the case of 1s-1s capture. When band mixing is not included, continuous state capture is more efficient than 1s-1s capture [76]. The reason is that, given the QW structure, for 1s-1s capture, the final 1s state exciton has to have a specific momentum, and for the continuous state capture the final electron-hole pairs can have a range of momentum. In other words, more final states are available in the latter case. As the capture time is significantly reduced by band mixing, the 1s-1s capture becomes more efficient.

The escape time from 1s state of HH1 exciton to 1s state of 3D exciton has also been calculated. And the results are shown in Figure 5-6. The solid line is from the parabolic model and the dashed line from the mixing model. We see here characteristics similar to those in the capture processes. Band mixing has a

significant influence on the exciton escape. The escape time becomes one order of magnitude smaller when band mixing is included.

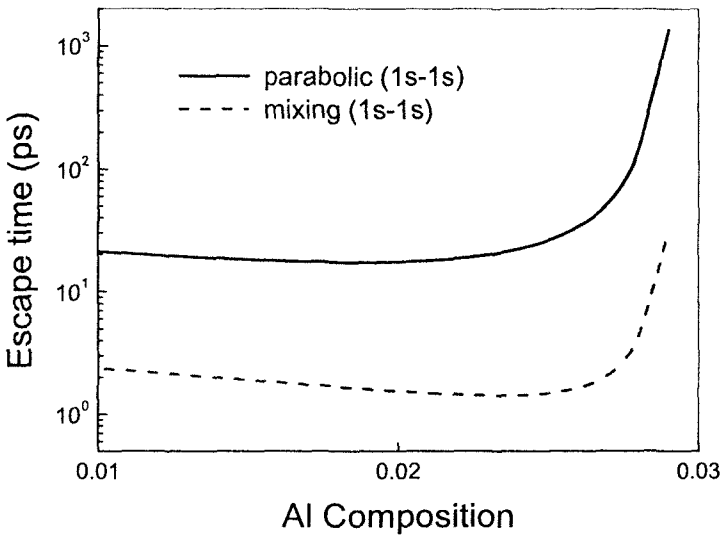

Figure 5-6 Escape times from 2D 1s state to 3D 1s state

5.5 Conclusions

We have studied band mixing effects in exciton capture/escape in shallow quantum wells. We have shown that band mixing can result in one order of magnitude smaller capture and escape times than the previous results that do not include such effects. These results will be useful in interpreting the device physics and in designing optoelectronic devices where exciton capture/escape plays an important role. For instance, they could have significant implications on

functionalities of optoelectronic devices such as EA modulators, QW based photo-detectors and solar cells. Faster capture and escape result directly in higher speed of devices. They also indirectly affect other characteristics, i.e., most noticeably the optical nonlinearity of EA modulators which is of central interest for this thesis. The shorter the time for excitons to escape from quantum wells, the less concentration of carriers will accumulate in the QW structures. This will lead to smaller absorption saturation and therefore less optical nonlinearity in EA devices. The capture and escape time also influence the thermalization of 3D and 2D excitons and thus the dark current and noise of photo-detectors and the short circuit current of solar cells.

The results may also be helpful for understanding exciton-phonon scattering processes in other quantum structures such as deep quantum wells, quantum wires and quantum dots where valence band mixing could be significant.

Chapter 6

EAM Design: High speed and High Saturation

6.1 Introduction

As we discussed before, the electro-absorption modulators (EAM) are expected to play important roles in optical signal processing such as wavelength conversion [3][4] and signal regeneration [7]. Compared to other alternative components such as SOA [8] and nonlinear optical fiber [9] in these applications, an EAM based component has simpler architecture and less noise. In addition it is also potentially advantageous in high-speed operation and low power consumption. The last two characteristics are critically dependent on the optical absorption saturation mechanisms inside the EAM, which in turn are determined by the process of carrier sweep-out in quantum wells. In the following we will exam the sweep-out process in detail.

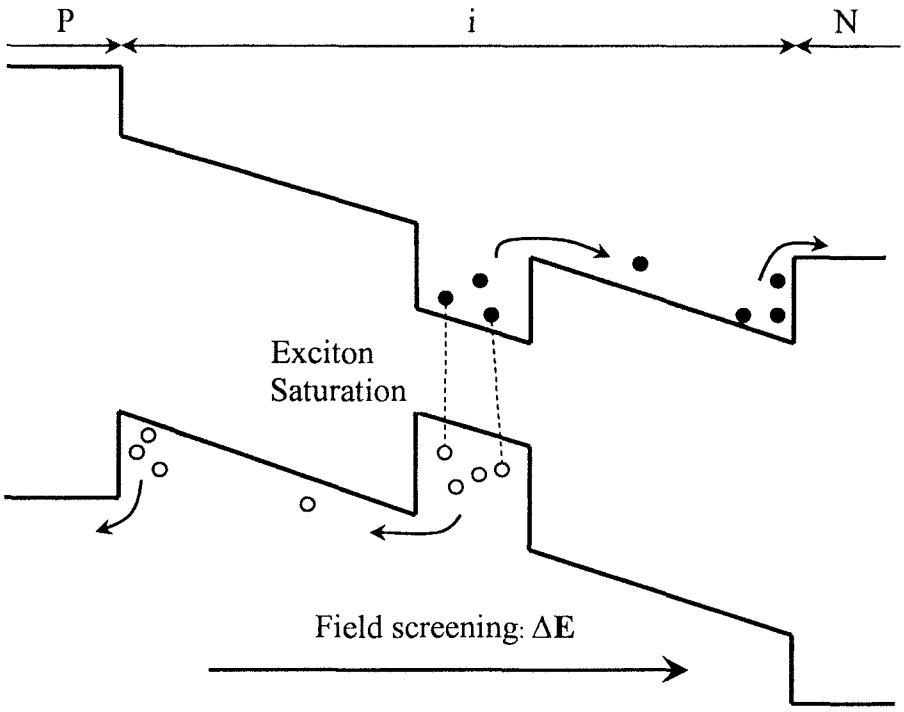

Figure 6-1 Carrier sweep-out in quantum well and optical absorption saturation: exciton saturation and electric field screening

As illustrated in Figure 6-1, an incident optical pulse creates excitons in quantum well, which will subsequently be ionized. The resulting electrons and holes will escape out of the quantum well and move through the intrinsic region of a p-i-n diode and finally be absorbed in P or N region. For a high intensity optical pulse, the excessive electrons and holes in the quantum well will cause exciton saturation through the blocking mechanisms originated from Pauli exclusion. In addition, the photo-generated electrons and holes both inside and outside the quantum well can screen the electric field in the quantum well region

and thus cause absorption reduction, equivalently, absorption saturation. Extensive research has been done on these two saturation mechanisms both theoretically and experimentally. On the theoretical side, the exciton saturation has been described by phase-space filling theory [10]~[13] and the electric field screening by Poisson equation [14] or plus drift-diffusion models [15]. However, the integration of these two interrelated saturation processes is still modeled in a phenomenological manner [16]. To overcome this drawback, in Chapter 2 we have developed a self-consistent, physics-based model that includes both exciton saturation and electric field screening. Here we will demonstrate the importance of the comprehensive model in designing a high-speed and nonlinear EAM.

High speed (fast carrier sweep-out from quantum well) and high optical saturation (or high optical nonlinearity) are often closely and inversely related. In contrast to the linear application of EAM such as modulation where high speed often co-occurs with high optical linearity, for the nonlinear applications of EAM such as wavelength conversion, high speed has to compromise with strong optical saturation. To achieve the best trade-off, high optical saturation at the highest possible speed, accurate modeling of the saturation dynamics is essential. More importantly, a physics based model can help us to gain insights into the underlying physical processes. In this chapter, we will show how the different dynamic responses of electrons and holes in a quantum-well EAM under an optical pulse excitation can harm or help in achieving high speed and high optical

saturation. We will also show that, by carefully considering the different dynamic behaviors of electrons and holes, we can enhance the optical saturation while keep avoiding severe reduction of device operation speed. High speed is essential for applications in 40GHz and above optical network, and high optical saturation results in to low power consumption.

In the following sections, we will first stimulate the basic characteristics of EA modulators, and then focus on the different saturation dynamics of electrons and holes. In the end, we will optimize the quantum well structure to improve device performance.

6.2 Basic characteristics

6.2.1 EA modulators in wavelength conversion

Figure 6-2 illustrates the basic principle of EA modulators working as wavelength converters. Two optical beams of different wavelength are incident upon the EA modulator: one is a probe and the other is the signal. When the power of the signal is at off level, the probe will be fully absorbed. When the power of the signal is at on level, if the power is high enough to cause optical absorption saturation, the probe will not be fully absorbed, and thus the pattern of the signal at one wavelength will transfer to the probe at another wavelength. To understand this process, we are most interested in absorption saturation dynamics. In this

chapter we will study in detail the dynamic change of optical absorption under a strong optical pulse excitation. How much absorption change can be obtained and how fast it can happen. However, to understand these two characteristics, their underlying physics and their relationship to device structure and material parameters, we need to start with some basic characteristics of EA modulators.

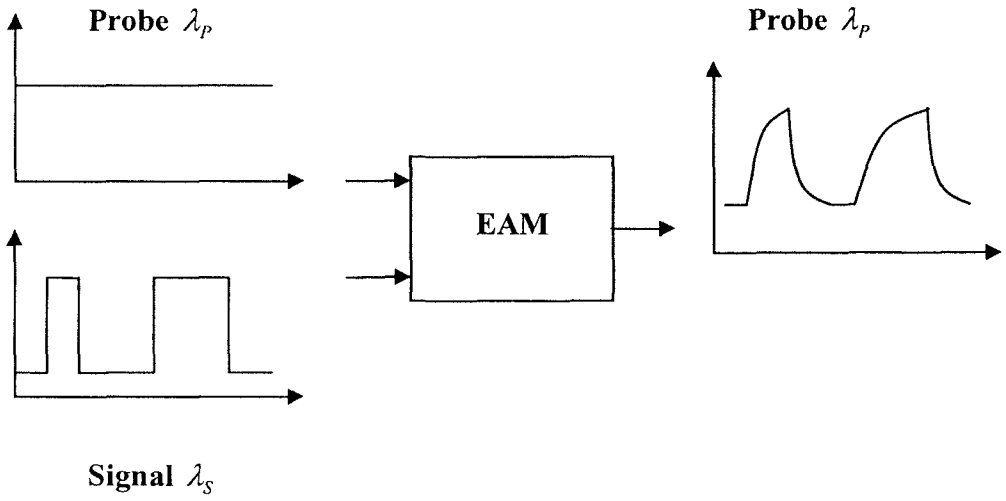

Figure 6-2 Wavelength conversion based on cross absorption modulation in EAM

The fundamental mechanism that EAM works on is electro-absorption effects. The optical absorption can be easily controlled through changing the voltage bias. Figure 6-3 shows the optical absorption coefficients for different electric fields for a typical $In_{0.53}Ga_{0.47}As$ / $In_{1-x}Ga_xAs_yP_{1-y}$ quantum well. Here the quantum well width is 8 nm, and both the well layer $In_{0.53}Ga_{0.47}As$ and the

barrier layer $In_{0.8}Ga_{0.2}As_{0.44}P_{0.56}$ are lattice-matched to InP. The excitonic peak is around 1570nm for zero electric field. Above this wavelength the absorption decreases as the electric field decreases. In our following simulations, we choose optical pulses at wavelength 1590nm. To use an EAM as wavelength converter, the EAM is usually reversely biased and works under certain electrical field. As shown later, when excessive electrons and holes are generated by a high intensity optical impulse, the electric field in the quantum well region will be screened by the photo-generated carriers. The screening will reduce the electric field and therefore the absorption. This is equivalent to optical absorption saturation.

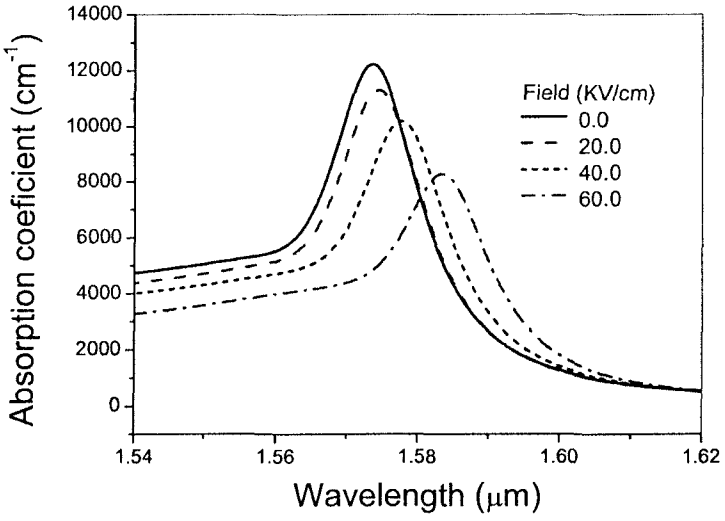

Figure 6-3: Optical absorption of 8-nm wide $In_{0.53}Ga_{0.47}As$/ $In_{1-x}Ga_xAs_yP_{1-y}$ quantum well under different electric fields

6.2.2 Exciton saturation

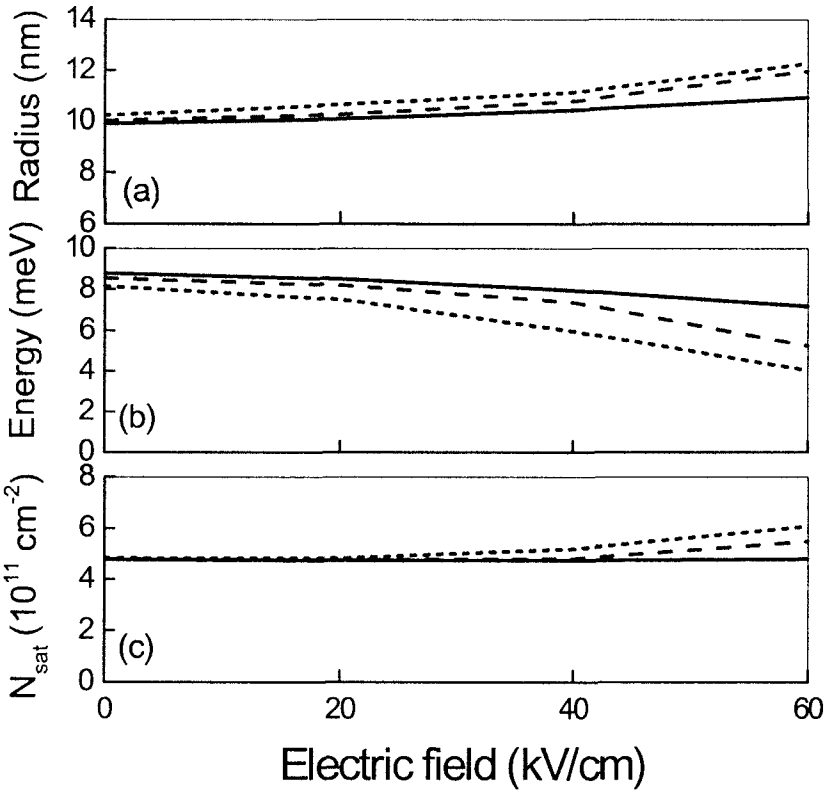

Figure 6-4 Exciton saturation as function of electric field in an 8-nm wide $In_{0.53}Ga_{0.47}As/In_{1-x}Ga_xAs_yP_{1-y}$ quantum well. a) exciton radius; b) exciton binding energy; c) exciton saturation density. Barrier layer composition: Solid line x = 0.2; dashed line: x = 0.25 and dotted line x = 0.3.

Another saturation mechanism that is more intrinsic is exciton saturation. As discussed before, thermalized excitons (bound electron-hole pairs) and unbound electrons and holes in the quantum well are governed by Pauli exclusion

principle. When there are excessive carriers in the quantum wells, the electron states will be occupied and not available for the creation of new excitons. As a result exciton absorption will decrease. Mathematically the exciton saturation is characterized by the exciton saturation density defined in equation (2.20). We have calculated the exciton saturation density for an 8-nm wide $In_{0.53}Ga_{0\,47}As / In_{1-x}Ga_xAs_yP_{1-y}$ quantum well as a function of electric field for different heights of barrier potential and the results are plotted in Figure 6-4. The solid lines are for Ga composition x = 0.2; the dashed lines x = 0.25; the dotted lines x = 0.3. They correspond to the barrier heights for electron and hole of 123/164, 95/125, and 69/91. (in meV), respectively. Figure 6-4a and Figure 6-4b show the radius and the binding energies of excitons in a QW as function of electric field. It can be observed the radius decreases as the electric field decreases or the barrier height increases. The opposite is true for the binding energy. Equation (2.20) states that the saturation density is determined by exciton radius and binding energy. As a result of the oppositely changing behaviors of the exciton radius and the binding energy, the saturation density remains relatively unchanged as shown in Figure 6-4c.

6.3 Saturation dynamics

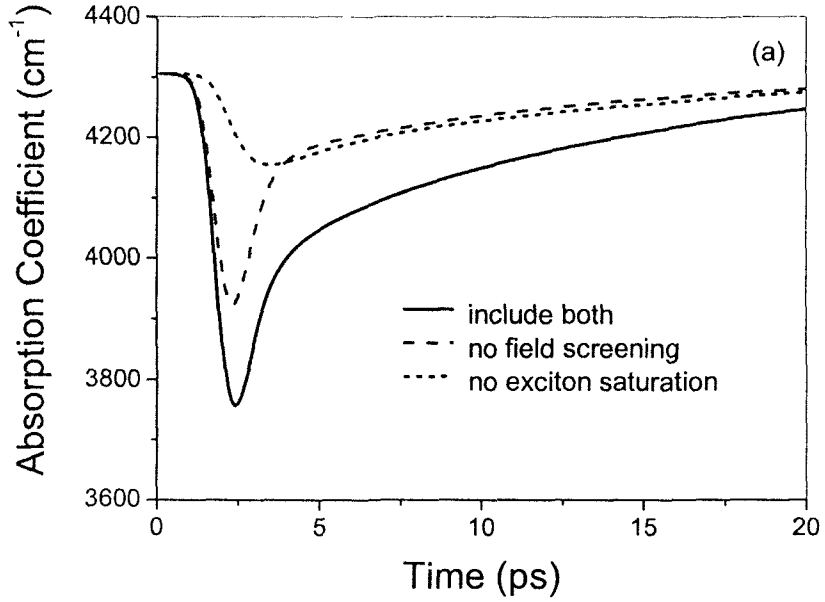
Absorption Coefficient (cm^{-1})
4400
4200
4000
3800
3600
0
5
10
15
20
Time (ps)
(a)
include both
no field screening
no exciton saturation

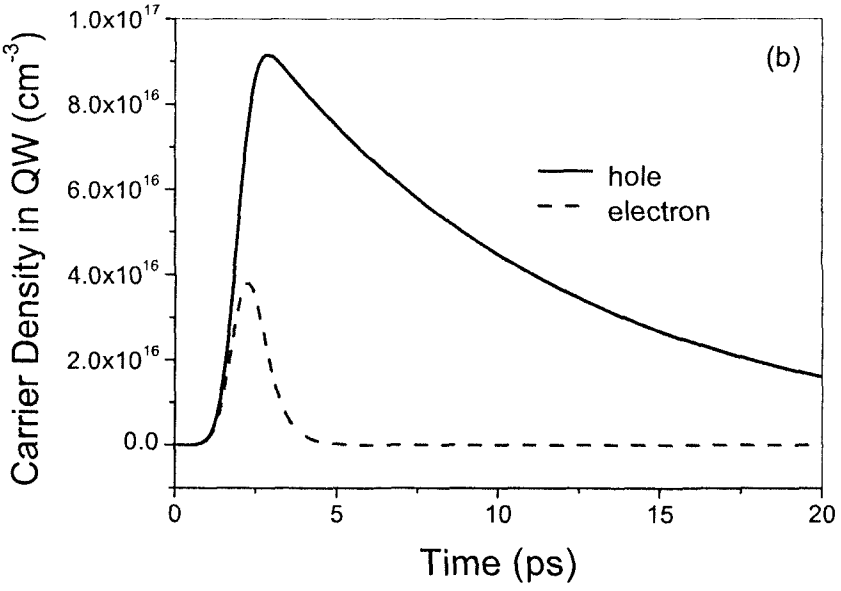
Carrier Density in QW (cm^{-3})
1.0x10^{17}
8.0x10^{16}
6.0x10^{16}
4.0x10^{16}
2.0x10^{16}
0.0
0
5
10
15
20
Time (ps)
(b)
hole
electron

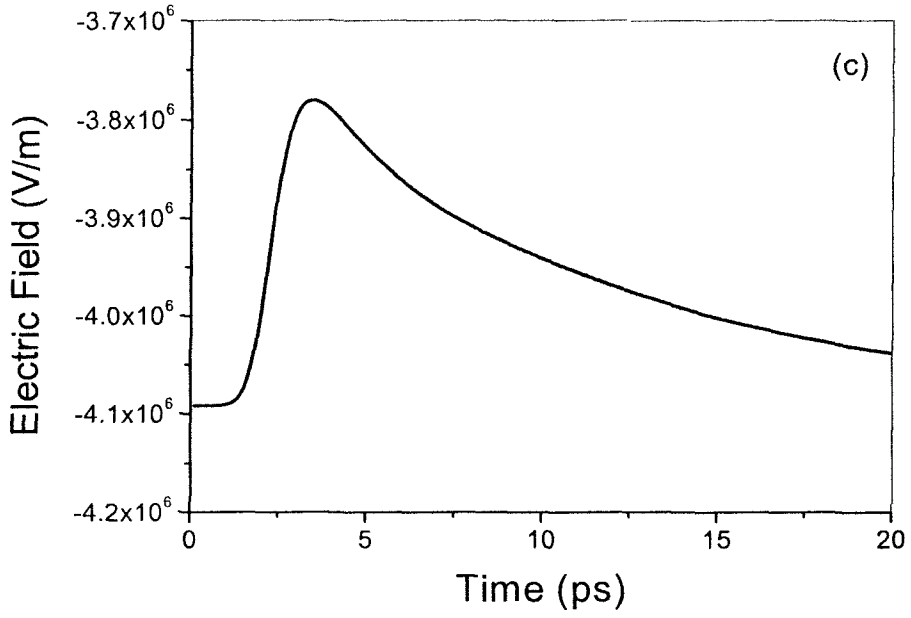

Figure 6-5 a) Absorption coefficient changes under an optical pulse excitation of 8-nm wide $In_{0.53}Ga_{0.47}As/In_{1-x}Ga_xAs_yP_{1-y}$ quantum well. Layer Ga composition x = 0.25; b) electron and hole concentrations in quantum well; c) electric field in the quantum well region.

Now we turn to the dynamics. We simulate the time response of an EAM under a strong optical pulse excitation. The pulse is a Gaussian pulse with 1.0 ps FWHM (full-width at half maximum) and energy 0.3 pJ. It arrives at t = 2.0 ps. The structure simulated is a single 8-nm wide $In_{0.53}Ga_{0.47}As$ / $In_{1-x}Ga_xAs_yP_{1-y}$ quantum well sandwiched by two SCH with typical thickness of 0.15-um. The barrier Ga composition is x = 0.25. The optical absorption coefficient changes are shown in Figure 6-5a. The two sources of saturation are clearly demonstrated in

Figure 6-5a. The dashed line is obtained when the electric field screening is turned off, i.e., $\alpha = \alpha_0(F_0)/(1+N/N_S)$ with a constant background electric field. This case corresponds to exciton saturation induced by excess carriers/excitons in the quantum well only. The dotted line is obtained by setting the carrier density in equation (2.21) to zero, i.e., $\alpha = \alpha_0(F)$. This case corresponds to the saturation induced by electric field screening only. The electron and hole densities in the QW are also plotted in Figure 6-5b. They are correlated with the exciton saturation behavior in Figure 6-5a. For instance, both the exciton saturation and electron dynamic responses (dashed lines in Figure 6-5a and in Figure 6-5b) show relatively sharp peaks at the beginning of the time response. Similarly, the electric field change in the QW is plotted in Figure 6-5c and is also correlated to the saturation behavior (dotted line in Figure 6-5a).

We have also performed the simulation varying the optical pulse energy. The minimum absorption coefficient (the minimum point of the solid line in Figure 6-5a) as a function of pulse energy is plotted in Figure 6-6. It demonstrates saturation behavior, i.e., that the absorption coefficient decreases as the pulse energy increases.

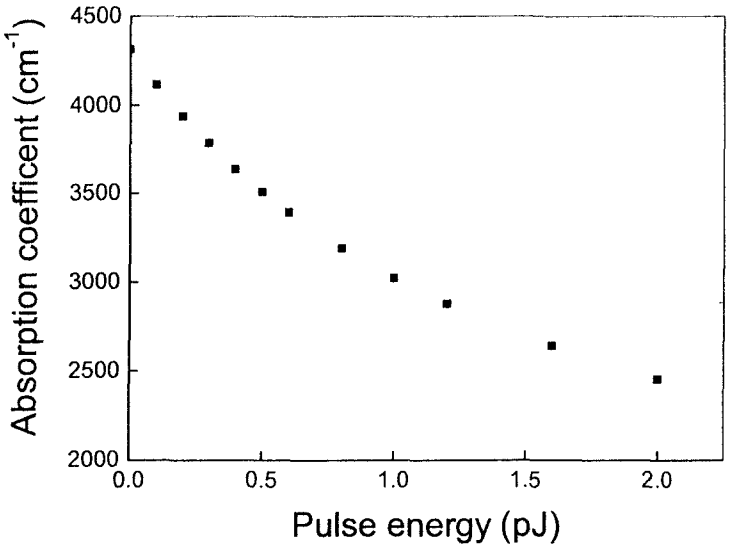

Figure 6-6 Minimum absorption coefficient versus pulse energy of input light

6.4 Design Optimization of EAM

6.4.1 Optimization of SQW

For the quantum well simulated in the above, we observed that electron and hole responses are unbalanced as shown in Figure 6-5b. There are many more holes than electrons in the quantum well. This is caused by several reasons. First, the quantum well barrier potential is higher for holes than for electrons. The splitting between the conduction band offset and the valence band offset is about 43/67 for the $In_{0.53}Ga_{0.47}As / In_{1-x}Ga_xAs_yP_{1-y}$ quantum well. Second, the effective mass of a

hole is larger than that of an electron. Third, the electron mobility is much larger than the hole mobility and thus moves away fast after escape out of the quantum well. Consequently, there are more holes accumulated in the quantum well as shown in Figure 6-5b. The responses in Figure 6-5b are undesirable from the standpoint of designing a nonlinear EAM. It has a long time tail due to slow hole escape. Furthermore, it is predominately holes that accumulate in quantum well. As we know from equation (2.23). Electrons have smaller density of states and thus easier to saturate. A larger electron concentration will enhance optical saturation. These two characteristics work against our goal of high speed and high nonlinearity of the EAM.

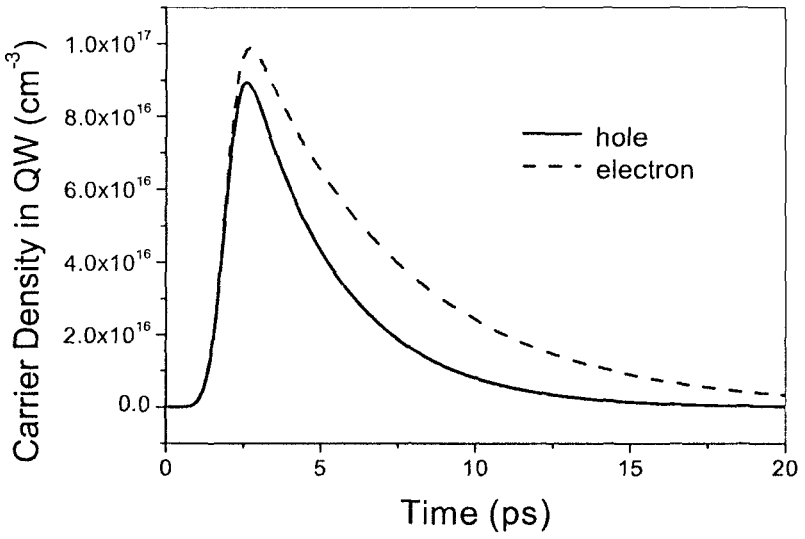

Figure 6-7 Electron and hole responses in $In_{0.53}Ga_{0.47}As/In_{1-x-y}Ga_xAl_yAs$ quantum well

These characteristics of $In_{0.53}Ga_{0.47}As$ / $In_{1-x}Ga_xAs_yP_{1-y}$ quantum wells lead us to search for other material systems for fast and highly nonlinear EAMs. Basically, we need a material system with a higher barrier potential for electrons than for holes. This can be achieved by replacing $In_{1-x}Ga_xAs_yP_{1-y}$ with $In_{1-x-y}Ga_xAl_yAs$ as the barrier material. For the $In_{0.53}Ga_{0.47}As / In_{1-x-y}Ga_xAl_yAs$ system, the conduction band and valence band ratio is around 70/30 (In our actual simulation, we have used the lineup theory in [54] to align the band edges of all material layers. The lineup theory gives ratios ranging from (66~68)/(34~32) for the material compositions used in our simulation). In Figure 6-7 we have plotted the electron and hole responses under a Gaussian optical pulse with FWHM 1.0 ps and energy 0.3 pJ for a $In_{0.53}Ga_{0.47}As / In_{1-x-y}Ga_xAl_yAs$ quantum well. Here we have used unstrained $In_{1-x-y}Ga_xAl_yAs$, which is the combination of lattice-matched $In_{0.52}Al_{0.48}As$ and $In_{0.53}Ga_{0.47}As$. The latticed matched $In_{1-x-y}Ga_xAl_yAs$ is usually labeled as $(In_{0.52}Al_{0.48})_z(In_{0.53}Al_{0.47})_{1-z}As$. In Figure 6-7 z = 0.5 structure is simulated. We see that the responses of the electrons and holes are basically balanced with slightly more electron concentration. As we will show shortly, this characteristic is beneficial in designing high speed and highly nonlinear EAM.

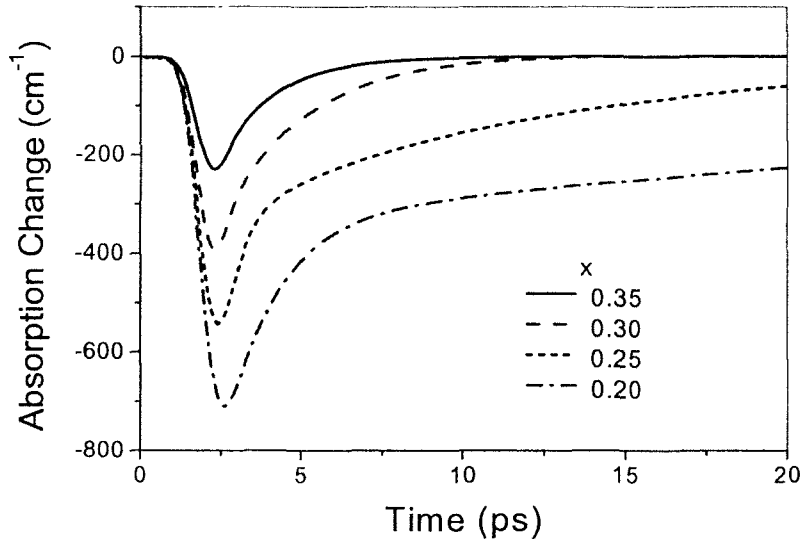

Figure 6-8 Optimization for maximum absorption change for $In_{0.53}Ga_{0.47}As/In_{1-x}Ga_xAs_yP_{1-y}$ SQW

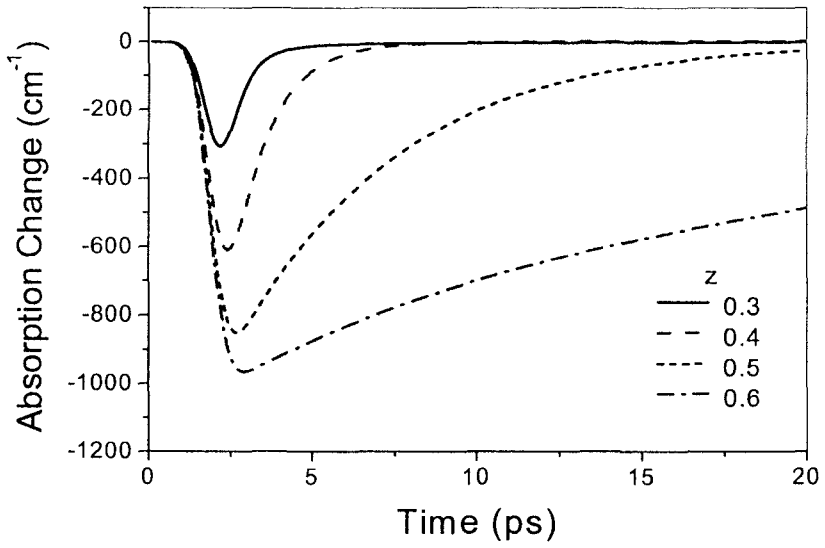

Figure 6-9 Optimization for maximum absorption change for $In_{0.53}Ga_{0.47}As/ In_{1-x-y}Ga_xAl_yAs$ SQW

Now we optimize both $In_{0.53}Ga_{0.47}As$ / $In_{1-x}Ga_xAs_yP_{1-y}$ and $In_{0.53}Ga_{0.47}As$ / $In_{1-x-y}Ga_xAl_yAs$ quantum well structure for maximum absorption changes. In Figure 6-8 we have plotted the absorption coefficient changes for 8-nm wide $In_{0.53}Ga_{0.47}As$ / $In_{1-x}Ga_xAs_yP_{1-y}$ wells with different x composition. The barrier height increases as x decreases. We observe that the absorption change increases as the barrier becomes higher, but beyond certain point, i.e., x = 0.25 in this example, long tails appear. In other words, beyond this point the absorption change increase will come at the price of very slow device operation, making it unsuitable for application of 40GHz and above. In this example, the maximum absorption change we can obtain without severely reducing the speed is about 400 cm^{-1} and the corresponding decay time is about 10 ps. In Figure 6-9 we have plotted the absorption coefficient changes for 8-nm wide $In_{0.53}Ga_{0.47}As$ / $(In_{0.52}Al_{0.48})_z(In_{0.53}Al_{0.47})_{1-z}As$ wells with z composition varying from 0.3 to 0.6, corresponding to 119~256 meV barrier for electrons and 56~119 meV barriers for holes. Similarly, we observe that the absorption change increases as the barrier becomes higher. But the turning point appears at the higher barrier. Figure 6-9 shows long tails appear after the absorption change increase reaches about 800 cm^{-1}. This is more than 2 times higher than what $In_{0.53}Ga_{0.47}As$ / $In_{1-x}Ga_xAs_yP_{1-y}$ quantum wells can attain.

The dynamic behaviors in Figure 6-8 and Figure 6-9 can also be plotted as decay time versus maximum absorption coefficient changes as shown in Figure 6-10. Here the decay time is defined as the time interval between the point of maximum absorption change and the point when the absorption change falls to 1/e of its maximum value.

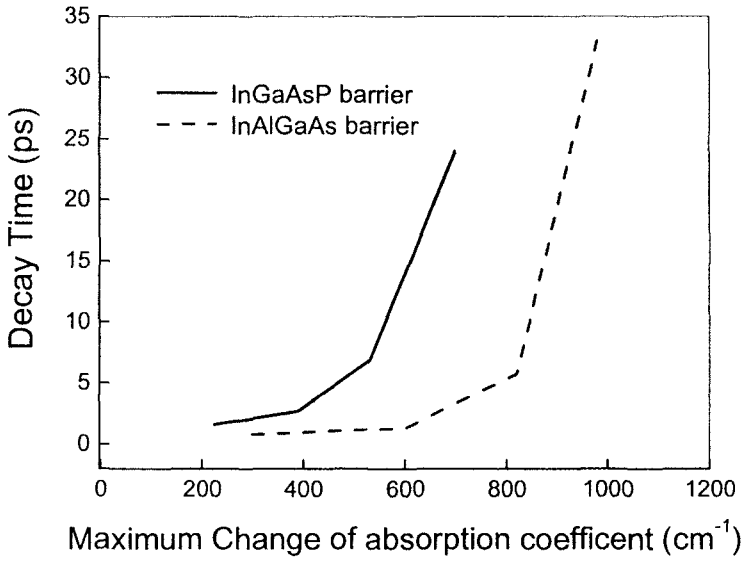

Figure 6-10 Decay time versus maximum absorption coefficients change

The above simulations clearly demonstrate that the high optical nonlinearity can be achieved through careful design of the dynamic behaviors of electrons and holes. The characteristics of $In_{0.53}Ga_{0.47}As / In_{1-x-y}Ga_xAl_yAs$ well shown here are very important for the high-speed applications of EAMs for optical processors such as wavelength converters.

6.4.2 Optimization of MQW

We have also simulated the dynamic behavior of multiple quantum wells (MQW). The saturation dynamics of MQW EAMs made of both $In_{1-x}Ga_xAs_yP_{1-y}$ and $In_{1-x-y}Ga_xAl_yAs$ barriers have been compared. The MQW structure consists of eight 8-nm $In_{0.53}Ga_{0.47}As$ quantum wells separated by 10-nm barriers. The SCH regions are 0.8um thick. Again, we vary the barrier height to achieve the best dynamic behavior. The optimized behaviors (the largest absorption coefficient changes without long tails) for both $In_{1-x}Ga_xAs_yP_{1-y}$ and $In_{1-x-y}Ga_xAl_yAs$ (solid line) barriers are plotted in Figure 6-11. The solid line is the material absorption coefficient averaged over all wells of $In_{0.53}Ga_{0.47}As / In_{1-x-y}Ga_xAl_yAs$ EAM and the dashed line for that of $In_{0.53}Ga_{0.47}As / In_{1-x}Ga_xAs_yP_{1-y}$ EAM. We observed that the maximum absorption change is more than 50% lager for the $In_{1-x-y}Ga_xAl_yAs$ barrier structure than for the $In_{1-x}Ga_xAs_yP_{1-y}$ barrier structure. The difference of the maximum absorption changes between $In_{1-x-y}Ga_xAl_yAs$ and $In_{1-x}Ga_xAs_yP_{1-y}$ structures is smaller in the MQW case than in the SQW case. This can be attributed to the electric field variation in different quantum wells. The electric field variation in different quantum wells are plotted in Figure 6-12 for z = 0.5 $(In_{0.52}Al_{0.48})_z(In_{0.53}Al_{0.47})_{1-z}As$ barrier. We see that the electric fields in the first three wells actually increase, whereas the electric fields in the other

wells decrease. It should be pointed out what we are discussing here is the changes to the optical absorption coefficients. The actual absorption is exponentially dependent on this coefficient. A 50% improvement in absorption coefficients will have significant impact on device performance.

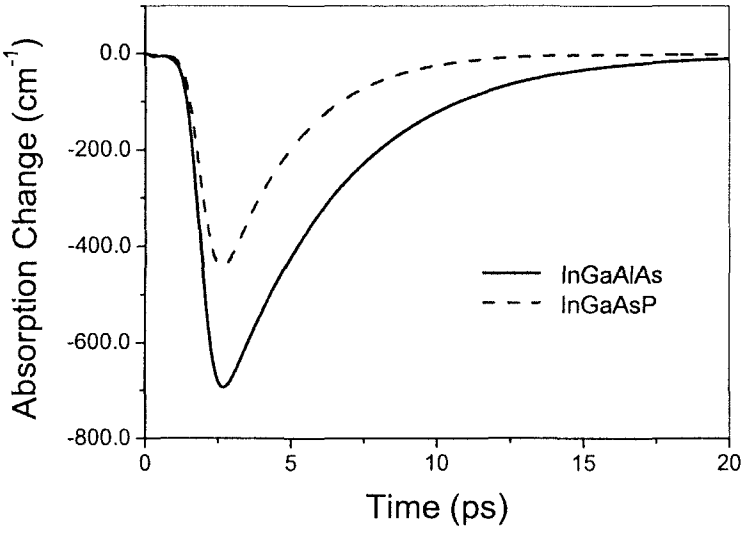

Figure 6-11 Optimized absorption change for eight 8-nm $In_{0.53}Ga_{0.47}As$ quantum wells with 10-nm $In_{1-x}Ga_xAs_yP_{1-y}$ barriers and $In_{1-x-y}Ga_xAl_yAs$ barriers

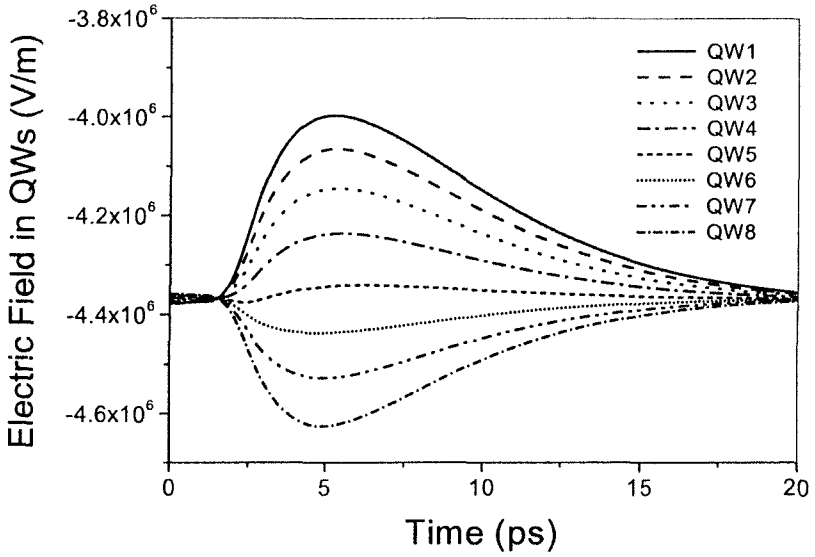

Figure 6-12 Electric field distribution in different quantum wells

6.5 Conclusions

The physics-based model, developed in Chapter 2 that includes two interrelated saturation mechanisms of exciton saturation and electric field screening in a self-consistent manner, has been applied to the study of electro-absorption modulators for nonlinear optics applications such as wavelength conversion and signal regeneration. The dynamic behaviors of electrons and holes under a strong optical pulse excitation in $In_{0.53}Ga_{0.47}As$ / $In_{1-x}Ga_xAs_yP_{1-y}$ and $In_{0.53}Ga_{0.47}As$ / $In_{1-x-y}Ga_xAl_yAs$ quantum wells have been investigated. For

$In_{0.53}Ga_{0.47}As$ / $In_{1-x}Ga_xAs_yP_{1-y}$ quantum wells, it is found that the slow hole sweep-out time in the quantum well impedes the device speed by creating a long time tail of absorption change and that larger hole concentrations in quantum wells is harmful for achieving large absorption changes, because holes are more difficult to saturate due to their large density of states. In contrast, for $In_{0.53}Ga_{0.47}As$ / $In_{1-x-y}Ga_xAl_yAs$ quantum wells, it is found that the electron and hole saturation dynamics are more balanced and there is more electron concentration in quantum wells. As a result, absorption coefficient change 2 times larger than that of $In_{0.53}Ga_{0.47}As$ / $In_{1-x}Ga_xAs_yP_{1-y}$ quantum wells can be achieved without sacrifice of device speed. Since the actual optical absorption is exponentially dependent on the absorption coefficient, the large change in absorption coefficient will significantly enhance the nonlinear behavior of the EAM. Strong optical saturation at high speed is essential for applications such as wavelength conversion and signal regeneration in 40GHz optical networks.

Chapter 7

EAM Design: TE and TM Polarization

We have just designed EA modulators for high speed and high saturation operation in the last chapter. Now we turn to another important issue: polarization dependence of EA modulators.

Different performance for the transverse electric (TE) mode and the transverse magnetic (TM) mode has caused problems for waveguide-based photonic and optoelectronic devices in many applications. Like other waveguide devices EA modulators inherently have a polarization dependence problem. In the past, however, relatively little work has been directed to the polarization issue in EA modulators. The reason may be that the EA modulators are either monolithically integrated with or closely connected to the signal source: the semiconductor laser diodes, and thus the polarization of input signal for these EA modulators can be well maintained. For in-line applications such as EA modulators for wavelength conversion, the polarization state of the input signal is random and difficult to control. Therefore polarization dependent characteristics have to be taken into consideration [3],[84]~[86].

In this chapter, we will address the polarization issue from two different perspectives. Firstly, we will look for the conditions under which EA modulators will have polarization insensitive operation. Secondly, we will exam how to enhance exciton saturation from the polarization perspective. In other words, which polarization is easier to saturate, TE or TM? How can we design EAM to achieve low saturation intensity?

7.1 TE and TM polarization independence

7.1.1 Lattice-matched quantum wells

We start with a typical lattice-matched quantum well structure. We consider a $In_{1-x}Ga_xAs / In_{1-x}Ga_xAs_yP_{1-y}$ quantum well. The well is 6-nm wide and x composition is 0.47. The barrier compositions x = 0.21 and y = 0.45. The band gaps of the well and barrier layer correspond to 1.55 μm and 1.2 μm, respectively. Both well and barrier layers are lattice-matched to the InP substrate. Based on the band structure model described in chapter 2, valence subbands (equation (2.5)) and the excitonic absorption spectrum (equation (2.19)) can be obtained for the lattice-matched quantum well and are shown in Figure 7-1 and Figure 7-2, respectively. From Figure 7-1 we notice that subbands HH1 and LH1 are far away from each other with inter-subband distance 40meV. Correspondingly, the excitonic absorption peaks associated with HH1 and LH1 are 70nm apart in the

spectrum shown in Figure 7-2. Since the TE mode primarily interacts with the excitons associated with HH1 and the TM mode with those associated with LH1, the absorption of TE and TM modes in a lattice-matched structure are quite different. For the normal working range of an EAM located around the first excitonic absorption peak, it is apparently impossible to achieve TE and TM independent operation in lattice-matched structures.

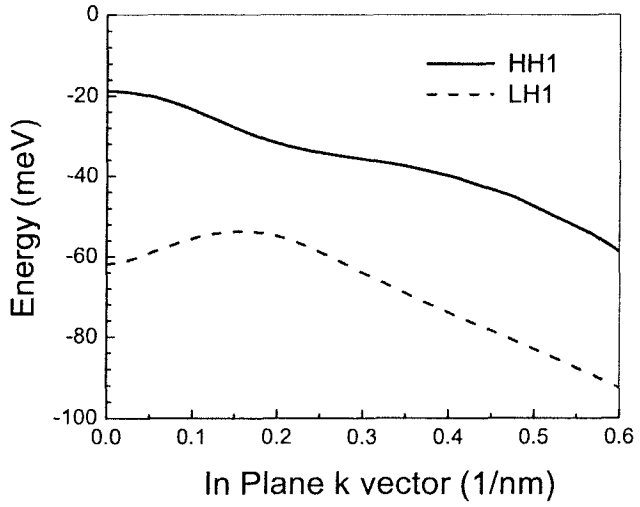

Figure 7-1 Band structure of lattice-matched 6-nm wide GaInAs/GaInAsP quantum well.

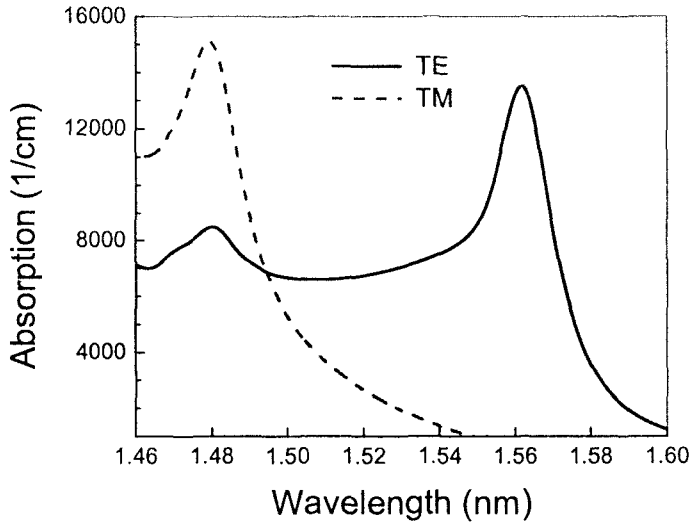

Figure 7-2 Absorption of lattice-matched 6-nm wide GaInAs/GaInAsP quantum well. Solid line: TE absorption; Dashed line: TM absorption

7.1.2 Strained quantum wells

To balance TE and TM absorption, it is natural to attempt to put the HH1 and LH1 bands close to each other so that the gap between TE and TM absorption peaks can be bridged. This can be readily done through utilization of strain and/or adjustment of quantum well width. For instance, we can introduce tensile strain into a quantum well by adjusting the x composition of $In_{1-x}Ga_xAs$ from 0.47 to 0.55. Then the HH1 and LH1 band-edge positions will align to each other as shown in Figure 7-3. It can be observed that HH1 and LH1 first sit close to each

other and then move away from each other. The characteristics are quite different from the parabolic shape that is assumed in the previous model that analyzes TE/TM operation of EAMs [86]. Actually, in the situation presented here, there a great deal of physics in play, and it is necessary to carefully access the applicability of various models with different physics approximations before we carry out the actual device design. The discussions of different models not only help us to understand the accuracy of various models but also shed some light on the physics processes involved.

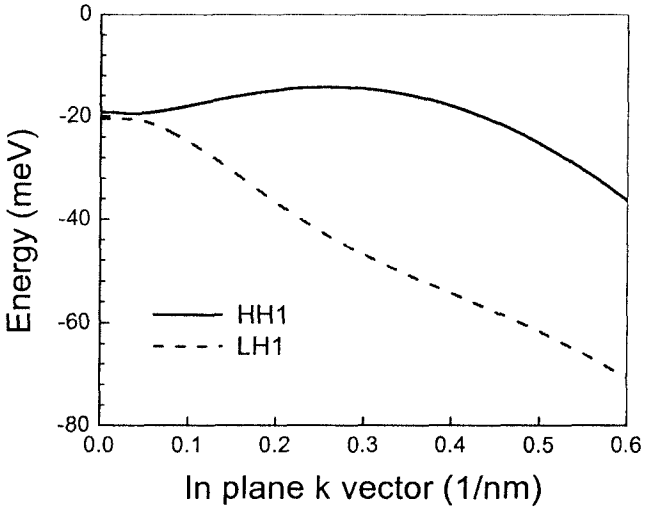

Figure 7-3 Non-parabolic dispersions of HH1 and LH1 when they are close to each other

Since the excitonic absorption is strongly dependent on the exciton binding energy, in the work which follows, we will evaluate the binding energy of

the ground state of excitons using different models and see how it changes as more and more physics details are taken into consideration. To facilitate the discussion, we also introduce two intermediate quantities: the effective mass of holes and the effective Coulomb potential between electrons and holes. As shown in equation (2.13), exciton states are determined by the kinetic energy and Coulomb potential. The kinetic energy is in turn determined by the energy dispersion relations of electron and holes (equations (2.1) and (2.5)), and the effective Coulomb potential is determined by the eigen functions of electrons and holes (equation (2.15)). We can use effective mass to roughly characterize the energy dispersion and an effective Coulomb potential to incorporate the wave functions imformation. Now we will exam how the binding energy changes when we include, step by step, valence-band mixing and exciton-state mixing into our discussions.

Models	Eb (HH1) (meV)	Eb (LH1) (meV)
Parabolic	4.12	4.64
Band mixing (non-parabolic dispersion)	8.8	7.39
Band mixing (mixed wave function)	5.32	5.29
Band mixing plus exciton coupling	5.32	7.89

Table 7-1 Binding energies of the first excitonic state associated with HH1 and LH1 calculated by different models

The first excitonic binding energies associated with HH1 and LH1 are calculated using four different models and the results are listed in Table 7-1. The structure considered is $In_{1-x}Ga_xAs$ well with x composition 0.55 and width 6.0nm. The simplest model is the parabolic model where no valance band mixing is included. In this model, the first excitonic state will be the 1s state. The binding energy of the 1s state of the HH1 exciton is 4.12meV and that of the 1s state of LH1 exciton is 4.64meV. The fact that the latter is bound slightly tighter than the former reflects primarily the fact that the in-plane effective mass of LH1 is larger than that of HH1. The hole effective masses used by the parabolic model [86] are given by Luttinger parameters $m_{hh} = 1/(\gamma_1 + \gamma_2)$ and $m_{lh} = 1/(\gamma_1 - \gamma_2)$.

Then we go one step further, including valence band mixing but excluding exciton state mixing. Thus the first excitonic state remains the 1s state. Valence band mixing can be incorporated in the exciton state through non-parabolic dispersions only as in Ref. [87]. The 1s binding energies under this condition increase to 8.8meV and 7.39meV for HH1 exciton and LH1 exciton, respectively. This can be explained by the changes of hole effective mass. From Figure 7-3 we can see that both HH1 and LH1 subbands are quite flat at the band edge. This is equivalent to saying that the effective masses are bigger than those used in the parabolic model.

If band mixing effects are incorporated also through the wave functions of HH1 and LH1 as the model in Ref. [59], the effective Coulomb potential in equation (2.15) will be reduced. The reason is as follows. The 1s state of HH1 is only associated with the 3/2 spinor component and the 1s state of LH1 only with – the 1/2 spinor component. For the structure we study here, due to strong band mixing, the 3/2 component in HH1 and -1/2 component in LH1 are significantly reduced as shown in Figure 7-4. This reduces the effective Coulomb potential in equation (2.15). Consequently, the binding energies of 1s states are reduced to 5.32 meV and 5.29 meV for HH1 and LH1 excitons, respectively.

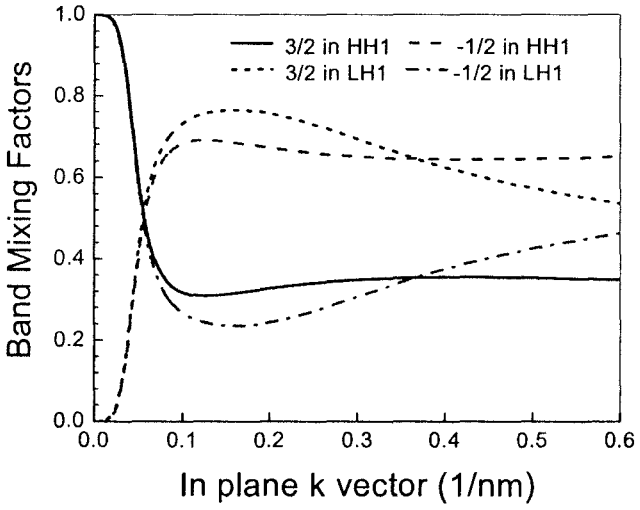

Figure 7-4 Valence band mixing in closely setting HH1 and LH1 subbands

But the picture of s-state only is not accurate and complete. When valence subbands are close to each other, as we discussed in Chapter 4, the first excitonic

states associated with HH1 and LH1 may not be pure s-state. They can be mixed state of different angular momentums [18]. Because of angular momentum conservation, the 1s state of HH1 will mix with p state of LH2, and the 1s state of LH1 will mix with the d state of HH1. Since the LH2 is far away from HH1, the 1s state of HH1 will largely remain s state with little mixing from p of LH2. But the 1s state of LH1 will mix strongly with d of HH1 as shown in Figure 7-5. When the exciton state mixing is included, we find that the binding energy for the first excitonic state associated with LH1 change again, from 5.29 meV of the previous model to 7.89 meV. This is because effective Coulomb potential reduction we have just discussed in the last paragraph is compensated by the presence of d component from HH1. As a result, the binding energies increase.

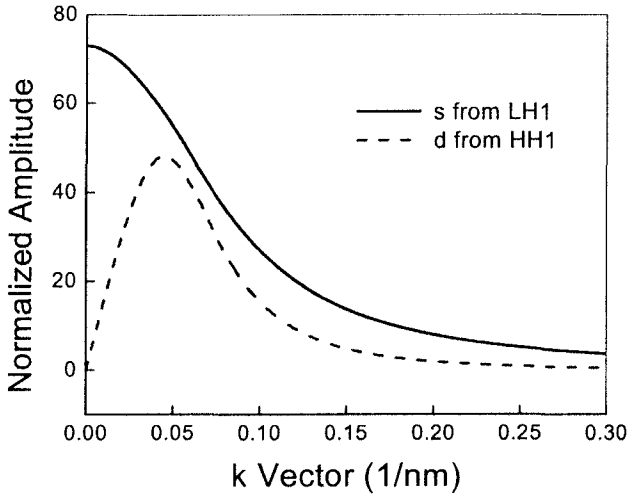

Figure 7-5 Exciton wave function for the mixed state of s state of LH1 and d state of HH1.

In the above steps, we clearly demonstrate that the complete model with full account of valence band mixing and exciton-state mixing is required to accurately evaluate the first excitonic states associated with HH1 and LH1. The rigorous exciton absorption model enables us to do reliable design simulations. We will analyze the TE and TM characteristics of the quantum well structures in which the HH1 and LH1 are close to each other, for instance, the energy level distance between the HH and LH subband edges within 1.0meV. We will vary the x composition of $In_{1-x}Ga_xAs$ well and correspondingly adjust the well width to keep the HH1 and LH1 aligned close to each other. The pairs of x composition and well width will correspond to different excitonic peak wavelengths. Through this parameter scan, we can survey the design window of wavelengths applicable to optical communications.

The absolute value of TE and TM absorption are shown in Figure 7-6 and the TE/TM ratio in Figure 7-7 for x from 0.5 to 0.55. It is observed that the absorption decrease and the TE/TM ratio increase as the x composition decreases. The decrease of absorption can be explained through a simple physics picture. To keep HH1 and LH1 close to each other, the well width will increase as x decreases. This is shown in the right y-axis in Figure 7-7. As the well width increases, the excitons are less confined in the z direction. They become more like 3D exciton and therefore less bound. We know the absorption is inversely related to the binding energy. So the absorption decreases.

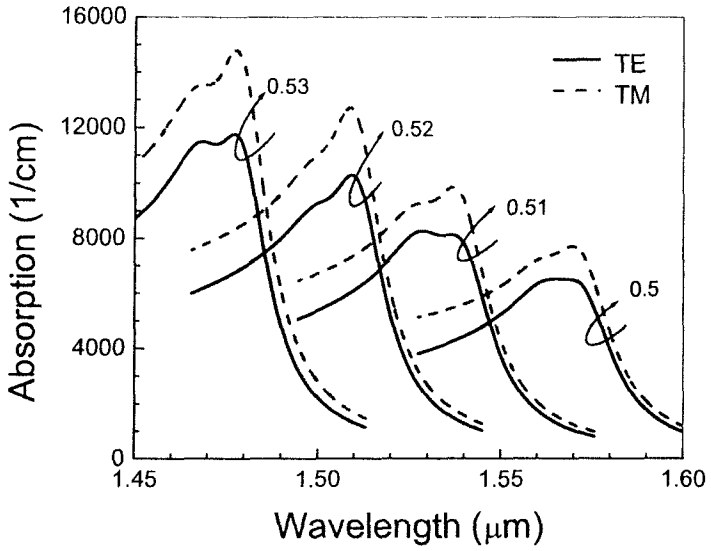

Figure 7-6: TE and TM absorption at various x composition. HH1 and LH1 are aligned

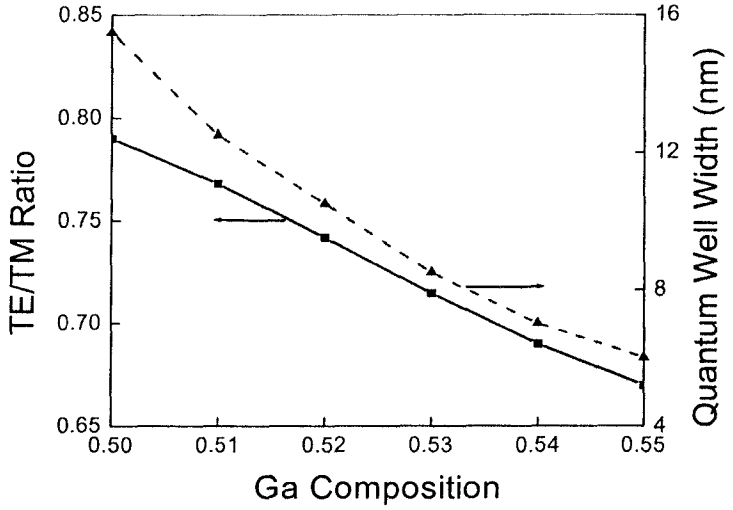

Figure 7-7 The ratio of TE over TM absorption at the first excitonic peak (Left y-axis). Quantum well width for different x compositions (Right y-axis)

In Figure 7-7 TE absorption is about 20~30% less than that of TM. The difference is smaller for wider quantum wells. These behaviors can be explained through the effective Coulomb potential as defined in equation (2.15). In the structure we are simulating, the largest contributions of optical absorption come from the first excitonic state associated with HH1 and the first excitonic state associated LH1. The former is the 1s state of HH1 and the latter the mixed state of LH1-1s and HH1-3d. Due to the contribution of the d component, the latter state will have a stronger binding energy and therefore larger optical absorption. Also the 1s state of HH1 is associated with 3/2 spinor component and therefore interacts with TE mode, and the mixed state of the 1s state of LH1 and the 3d state of HH1 is associated with the -1/2 spinor component and therefore mainly interacts with TM mode. This is why TM mode has stronger absorption. We also notice the effective Coulomb potential is also determined by the overlap integral between electron and holes as shown in equation (2.15). The simulation shows that the overlap difference between e-hh1 and e-lh1 will be reduced as the quantum well width increase, as is the TE/TM ratio.

Up to this point the discussion has been on material absorption. The TE/TM characteristics are ultimately determined by modal absorption. So we have to include the optical confinement factors. For the purpose of investigating the optical confinement behavior, we study the x=0.51 and w=12.5nm quantum

well since its wavelength is in the C-band to fiber optics communication as shown in Figure 7-6. For the material analysis, the single quantum well is often adequate since the coupling between neighboring quantum-wells can be neglected for most applications. For optical analysis here we will consider the case with different numbers of quantum wells. We will vary the number of quantum wells to optimize the optical structure. But the separate confinement hetero-structure (SCH) layer will be fixed at 40-nm thick and the barrier layer at 10-nm thick.

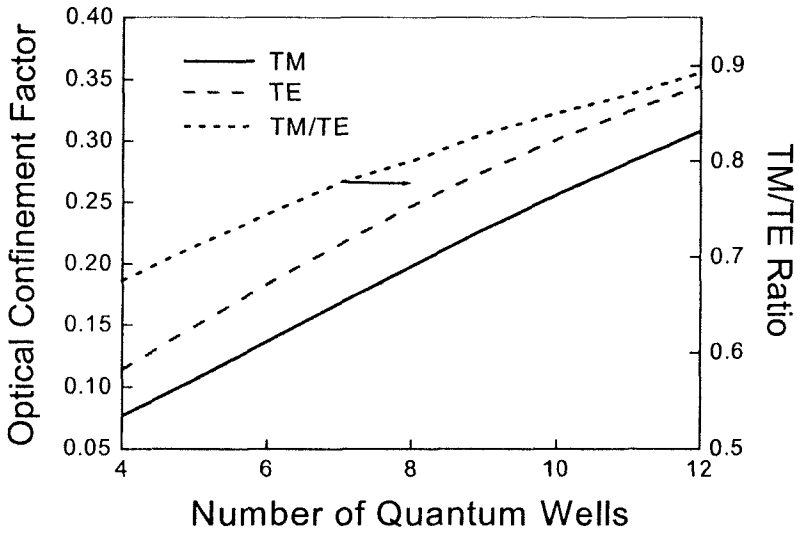

Figure 7-8 Optical confinement factor of TE and TM, the ratio of TM over TE for the quantum well structure of x composition 0.51 and 12.5 nm

The optical confinement factors for TE and TM modes as function of quantum well number are shown in Figure 7-8. The ratio of TM over TE

confinement factors is also plotted in Figure 7-8. The material absorption of TE over TM is about 77% as shown in Figure 7-7. Figure 7-8 show that the optical confinement of TM over TE is about 77% for the structure with 7 wells. Thus the material absorption difference of TE and TM can be compensated by the difference in optical confinement.

7.2 Low Saturation Intensity of TM polarization

In contrast to their applications in modulation where linear behavior is desirable, EA modulators as optical signal processors require a nonlinear response to the input optical signal. Low optical saturation intensity is the key for EA modulators to generate optical nonlinearity at low operation power, which enables the devices to work safely and efficiently in applications such as optical wavelength conversion and signal regeneration in optical networks [3][83]. For waveguide devices, in particular, high operation power may cause optical damage. In this section we study the saturation behaviors of optical transverse electric (TE) mode and optical transverse magnetic (TM) mode in waveguide to search for low optical power operation of EA modulators in optical wavelength conversion and signal regeneration.

7.2.1 Model formulation

Exciton phase-space filling is one primary mechanism responsible for absorption saturation in quantum well EA modulators. The exciton saturation density can be expressed as [10],[11]

$$\frac{1}{N_S} = 2\pi a_0^2 \frac{E_0}{kT} \tag{7.1}$$

Where a_0 is the exciton radius, E_0 is the exciton binding energy of the ground state. Exciton phase-space filling is based on the Pauli exclusion principle, which manifests itself here through the fact that two excitons cannot occupy the same space. Equation (7.1) indicates that the larger the exciton radius the smaller the saturation density, and the easier it is for the EA modulator to saturate. Absorption saturation is usually characterized by optical saturation intensity I_S as

$$\alpha = \frac{\alpha_0}{1 + I/I_S} \tag{7.2}$$

Where I_S is related to exciton saturation density as

$$I_S = \frac{N_S}{\alpha_0 \tau (L_w + L_b)} \tag{7.3}$$

Where α_0 is the exciton absorption coefficient, τ is the electron lifetime that is mainly the time for the electron to escape from the quantum well. L_w and L_b are the well width and barrier width, respectively. As equation (7.3) suggests, the optical saturation intensity is not only determined by the exciton saturation density (N_S) that represents how many electrons/excitons can be accommodated

in a given space. It is also affected by how fast electrons/excitons are generated through optical absorption (α_0) and how long electrons/excitons can stay in the quantum well (τ). According to (7.3), the obvious way to enhance the optical saturation is to increase the carrier lifetime. But the enhancement through this approach will be at the price of slow device speed. It is desirable to seek other means to strengthen the optical saturation. We note that equation (7.3) shows that the optical saturation intensity is also determined by the ratio of N_S/α_0, which can be obtained as follows

$$\alpha_0 = C_0 \frac{2}{L_W} M_b^2 I_{nm}^2 \frac{4M(0)\gamma}{\pi^2 a_0^2} \tag{7.4}$$

$$R = \frac{N_S}{\alpha_0} \propto \frac{kT/E_0}{I_{nm}^2 M(0)} \propto \frac{1}{I_{nm}^2 M(0) m_{\|}^r} \tag{7.5}$$

In equation (7.4), α_0 is the absorption coefficient at the first excitonic peak. C_0 is a term that lumps tegother several physics constants. $M(0)$ is the bulk matrix element. $m_{\|}^r$ is the reduced mass of the exciton and I_{nm} is the overlap integral of the electron and hole wave functions along the growth direction (z direction).

To understand the different saturation behaviors of TE and TM modes, we can apply the so-called mass reversal effect to our analysis. The commonly used terms of heavy-hole and light-hole refer the effective mass along the z direction m_z^{hh} and m_z^{lh}. Within the plane parallel to the quantum well surface, the heavy-

hole effective mass $m_{\|}^{hh}$ is in fact smaller than the light-hole effective mass $m_{\|}^{lh}$. $m_{\|}^{r}$ is given by $m_e m_{\|}^{h}/(m_e + m_{\|}^{h})$ and therefore is larger for light holes than for heavy holes. On the other hand, I_{nm} is determined by z direction effective masses and $m_z^{lh} < m_z^{hh}$. m_z^{lh} is closer to the electron effective mass m_e. Thus the wave function of a light hole will be closer to that of an electron. As a result, I_{nm} is larger for light holes as well. The matrix elements $M(0)$ for the e-hh transition for the TE mode is 1.5 and for the e-lh transition for the TM mode is 2.0. Adding these three factors together leads to the conclusion that the light-hole excitonic transition excited by a TM mode will have smaller R as defined in (7.5) and thus smaller optical saturation intensity.

It is worth having a closer look at the reduced mass $m_{\|}^{r}$ that is given by $m_e m_{\|}^{h}/(m_e + m_{\|}^{h})$. The electron effective mass m_e is nearly constant but the hole effective mass $m_{\|}^{h}$ can vary for different structures. The Hamiltonians of heavy-holes and light-holes in semiconductors can be expressed in terms of Luttinger parameters

$$H_{hh} = (\gamma_1 - 2\gamma_2)k_z^2 + (\gamma_1 + \gamma_2)k_{\|}^2 + W(k_{\|}) = \frac{\hbar^2}{2m_z^{hh}}k_z^2 + \frac{\hbar^2}{2m_{\|}^{hh}}k_{\|}^2 + W(k_{\|}) \quad (7.6)$$

$$H_{lh} = (\gamma_1 + 2\gamma_2)k_z^2 + (\gamma_1 - \gamma_2)k_{\|}^2 + W^{+}(k_{\|}) = \frac{\hbar^2}{2m_z^{lh}}k_z^2 + \frac{\hbar^2}{2m_{\|}^{lh}}k_{\|}^2 + W^{+}(k_{\|}) \quad (7.7)$$

The Hamiltonians show asymmetric effective masses along k_z and $k_{\|}$. For unstrained bulk material, the HH and LH sub-bands are degenerate at the band top and the asymmetry of effective mass will be washed out by the coupling term W. For highly strained bulk material, the asymmetry will be real since HH and LH sub-bands split far apart and the coupling term W can be ignored. For quantum well material, the effective masses behave in a similar but sometimes more complicated manner. The asymmetry of effective mass exists when the HH and LH are far apart and the complicated behavior occurs when HH and LH are close together.

Absorption saturation is ultimately measured by optical power. Equation (7.2) can be modified as

$$\alpha = \frac{\alpha_0}{1 + P/P_S} \tag{7.8}$$

With the optical saturation power defined as

$$P_S = \frac{N_S A/\Gamma}{\alpha_0 \tau (L_w + L_b)} \tag{7.9}$$

Where A is the active region area and Γ is the optical confinement factor. Γ for TM is smaller than that of TE. The difference is about ten percent for a typical waveguide.

7.2.2 Numerical results

In the following, we will evaluate R in (7.5) that characterizes the optical saturation of TE and TM modes. In equation (7.5), $m_{\parallel}^{r}$ can be estimated through hole effective mass that is extracted from the valance band dispersion obtained from equation (2.5). I_{nm} is obtained from the wave function of equations (2.1) and (2.5).

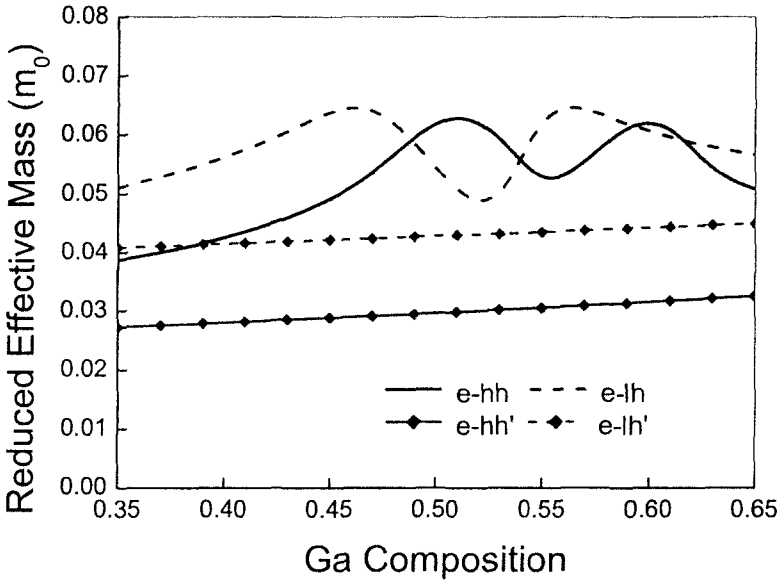

Figure 7-9 In-plane reduced effective masses of e-hh and e-lh excitons

The numerical simulation has been carried out for $Ga_x In_{1-x} As / InGaAsP$ quantum wells with 10.0nm wide wells and 10.0nm wide barriers. The in-plane reduced masses of e-hh and e-lh excitons are plotted in Figure 7-9. The solid-diamond line and the dashed-diamond line are obtained directly from Luttinger parameters without band mixing included. The solid line and the dashed line are

extracted from band structures with band mixing included. The effective masses of quantum wells with band mixing exhibit interesting behaviors. At low composition (x<0.48, compressive strain), HH1 is far above LH1, band mixing is weak and the effective mass reversal exists. At moderate composition (0.48<x<0.55, small strain), HH1 and LH1 are very close to each other and strong mixing of HH1 and LH1 occurs. The effective mass varies drastically (and may not even provide an accurate description of the band structure) and effective mass reversal may not occur. At higher composition (0.55<x<0.58, tensile strain), LH1 is far above HH1, band mixing is weak for LH1 and effective mass reversal occur for LH1. But at even higher composition (x >0.58) HH1 mixes with LH2, and its effective mass oscillates again. For the two regions where effective mass reversal clearly exists, at low composition (x <0.48) the first absorption peak will be an e-hh1 transition excited by TE, and at high composition (0.55<x<0.58) the first absorption peak will be an e-lh1 transition excited by TM. $m_{\|}^{r}$ of the former is smaller than that of the latter by about 1.5.

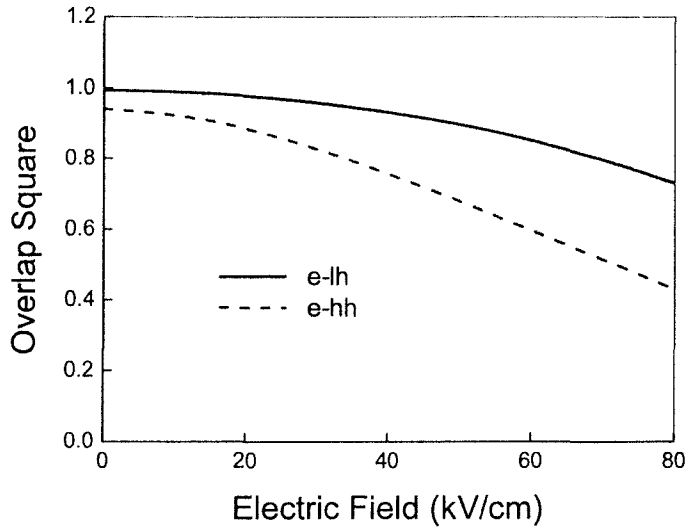

Figure 7-10 Overlap of electron wave function with heavy-hole and light-hole wave functions.

The square of overlap integrals of electron and hole wave functions I_{nm} are plotted in Figure 7-10 for both heavy-hole and light-hole as a function of electric field. Based on infinite the barrier quantum well model in text books, the distribution of electron wave functions is independent of the electron mass, which explains why the overlaps between the electron and both heavy-holes and light-holes are close to unity at zero electric field. The overlap of the light hole with electron, however, is larger than that of the heavy hole for nonzero electric field since the light hole is closer to electron in terms of the effective mass m_z. The difference of the overlaps is significant and has to be considered because electro-absorption devices either work under bias or have a built-in electric field.

As we mentioned, the matrix elements $M(0)$ are also different for e-hh for TE and e-lh for TM. All three factors together give a difference of a factor of about 2.5 in terms of the ratio R defined in equation (7.5). In other words, light-hole excitonic transitions excited by a TM mode can reduce the optical saturation power substantially.

It is desirable that the above analysis can be verified by experiments. The experimental device prototyping relevant to the discussion here will be report in next chapter.

7.3 Summaries

The TE and TM balancing issue for quantum-well EAMs has been studied using a simple parabolic model in which no band mixing and exciton state mixing are considered. We have shown here that both of these effects are important and have to be included in the TE and TM analysis of EA modulators. Based on a comprehensive absorption model, we have also designed quantum well EA modulators for TE and TM insensitive operation in optical communication systems. In the structures considered, the first heavy-hole subband and the first light-hole subbands are well aligned. And the material absorption of the TE mode is 20~30% less than that of the TM mode. The difference of material absorption

can be compensated by the difference of optical confinement factors of TE and TM modes.

To enhance the optical saturation in EAMs, we have used the excitonic absorption associated with light-holes and the TM mode, instead of the conventional excitonic absorption associated with thr heavy-hole and the TE mode. Because of differences in the quantum confinement of heavy-hole and light-hole along the growth direction, the in-plane reduced effective mass of HH and LH excitons, and the matrix elements for TE and TM modes, we show that EAM based on LH excitons excited by a TM mode exhibits much lower optical saturation intensity. This means that EA modulators can work at much lower optical power.

Chapter 8

Nonlinear EAM: Experimental prototyping

In the previous chapters, we have studied EA modulators for nonlinear applications from various perspectives, including physics, modeling and design. It is desirable to carry out some experimental prototyping of the devices to realize the design concept and to compare the theoretical simulation with experiment. In this chapter, we report the effort made on this front under the available fabrication and characterization conditions.

8.1 Design Considerations

One of our goals for device prototyping is to qualitatively verify the design concept of lower absorption saturation power using LH absorption excited by a TM mode as discussed in last chapter. The analysis in chapter 7 shows that the light-hole excitonic transition excited by optical transverse magnetic (TM) mode could have much lower saturation power than that of the conventional heavy-hole

excitonic transition excited by an optical transverse electrical (TE) mode. The TM mode scheme can be realized by proper use of tensile strain in quantum wells. Experimental data reported in Ref. [88] partially support this idea. Our goal here is to obtain a clear validation of the conception.

To implement the idea, we need to determine material compositions and geometric dimensions of the device. Based on the analysis in chapter 7 and reference to Ref. [88], a quantum well structure with compositions $In_{0.44}Ga_{0.56}As / InAs_{02}P_{0.8}$ well/barrier is proposed. These have 0.6% tensile strain in the wells and 0.6% compressive strain in the barriers. The net strain of the structure is zero. To determine the device dimension, we also evaluate the optical saturation intensity and electron lifetime in equation (7.3) and the results are shown in Figure 8-1 and Figure 8-2.

The optical saturation intensity of the quantum well is calculated for 6-nm, 9-nm, 12-nm wide wells. It can be seen that the narrower wells give higher saturation intensity. The reason is as follows. The narrower the wells, the closer the electron energy level to the barriers, the easier for electron to escape, the less electron concentration in wells, and the more difficult to saturate. In Figure 8-1 the optical saturation is characterized in term of optical saturation intensity, it can also be characterized by optical saturation power. For an EAM with typical optical waveguide structure, an optical saturation intensity of 10.0kW/cm2 in

Figure 8-1 corresponds to roughly 1.0mW optical saturation power. These values can be considered as low saturation intensity/power. In other words, EAM with these saturation characteristics will be effective in applications such as wavelength convention. It also can be pointed out that the saturation power can be adjusted through an applied field as shown in Figure 8-1, which provides a little extra freedom for the device to adopt to different applications.

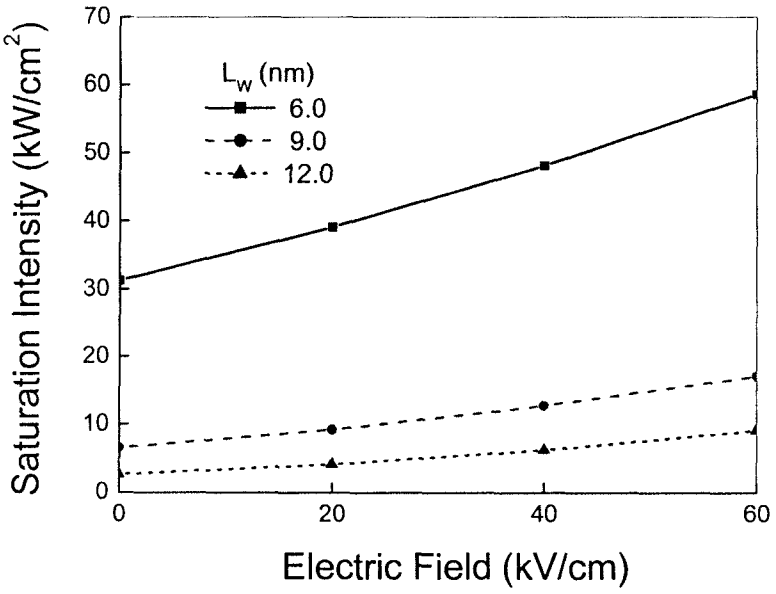

Figure 8-1 Optical saturation intensity as function of electric field.

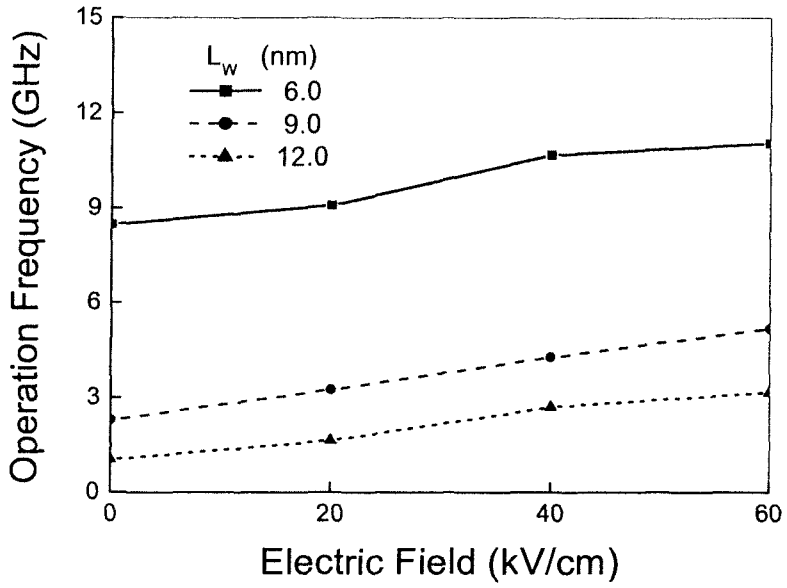

Figure 8-2 Operation frequency as function of electric field.

The device operation speed is estimated through the carrier escape time and the results are plotted Figure 8-2. Comparing Figure 8-1 and Figure 8-2, we note that the fastest structure of 6-nm QWs has the highest optical saturation intensity, which means the lower saturation power comes at the price of slower operation speed as we have discussed before. In the compromise of these two quantities, we will place our emphasis on low optical saturation power. In addition, to make EA modulators work at the wavelength range of 1530~1555nm, the C-band of optical communication, the quantum well width will be around 10.0~11.0 nm. The speed for the device of this range is not ideal (a few GHz). It

is believed that higher speed can be achieved in later stage of development through structure optimization.

8.2 Device Structure

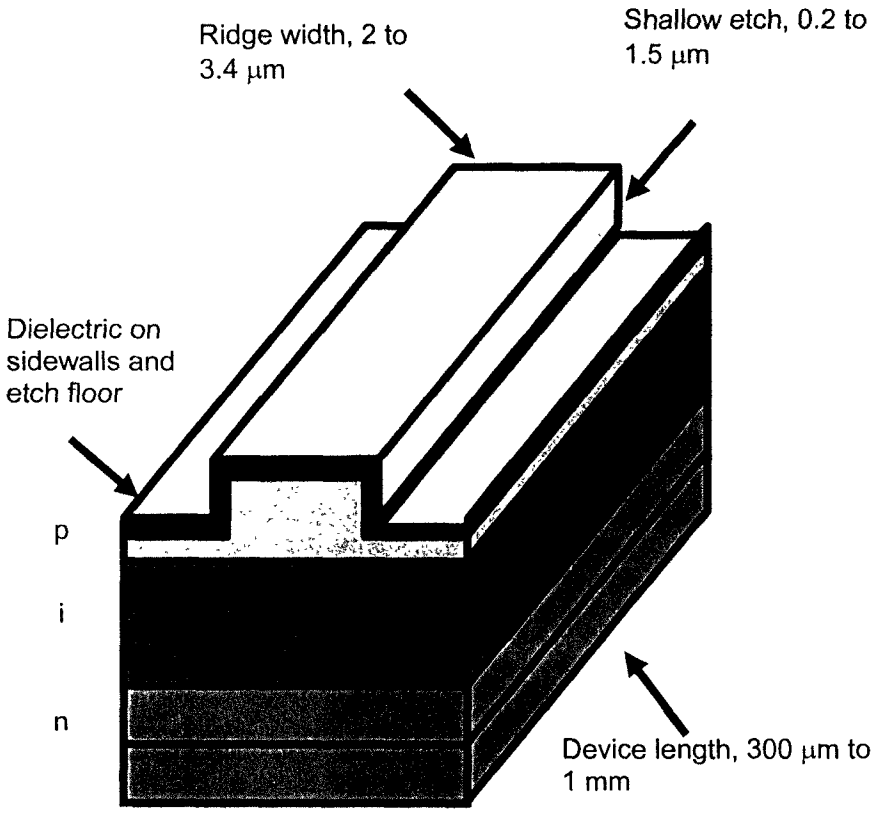

Figure 8-3 Schematics of EA modulator designed for wavelength conversion

Layer		Composition			Thickness	Doping	
Layer No	Layer Description	Material Composition	Eg (eV)	Strain (%)	Thickness (nm)	Doping level (cm^{-3})	Dopant Species
25	Contact	In(0.47)Ga(0.53)As	0.73	0.0	200	1.00E+19	Zn (p)
24	Cladding	InP	1.35	0.0	1500	1x10^18	Zn (p)
23	Barrier	InAs(0.2)P(0.8)	1.15	-0.6	25	intrinsic	
22	Well	In(0.44)Ga(0.56)As	0.81	0.6	10.5	intrinsic	
		repeat 9 times 2,3				intrinsic	
3	Barrier	InAs(0.2)P(0.8)	1.15	-0.6	10	intrinsic	
2	Well	In(0.44)Ga(0.56)As	0.81	0.6	10.5	intrinsic	
1	Barrier	InAs(0.2)P(0.8)	1.15	-0.6	25	intrinsic	
1	Buffer	InP	1.35	0.0	300	1.00E+18	Si (n)
0	Substrate	Substrate InP	1.35	0.0		4.00E+18	Si (n)

Table 8-1 Details of layer compositions and dimensions of EAM modulators designed for wavelength conversion

The structure of the designed EAM is schematically shown in Figure 8-3. Vertically, it is a PIN diode with multiple quantum wells in the intrinsic region. The cross section structure is a ridge waveguide with width from 2.0 to 3.4 um. The longitudinal length of the devices varies from 300um to 1000um. The detailed layer structures and compositions are listed in Table 8-1.

8.3 Device Characteristics

The EAM has been fabricated through CPFC (Canadian Photonics Fabrication Center). The finished devices are shown in Figure 8-4. Figure 8-4a shows the top

view of waveguide under microscope and Figure 8-4b shows the SEM picture of cross section of EAM.

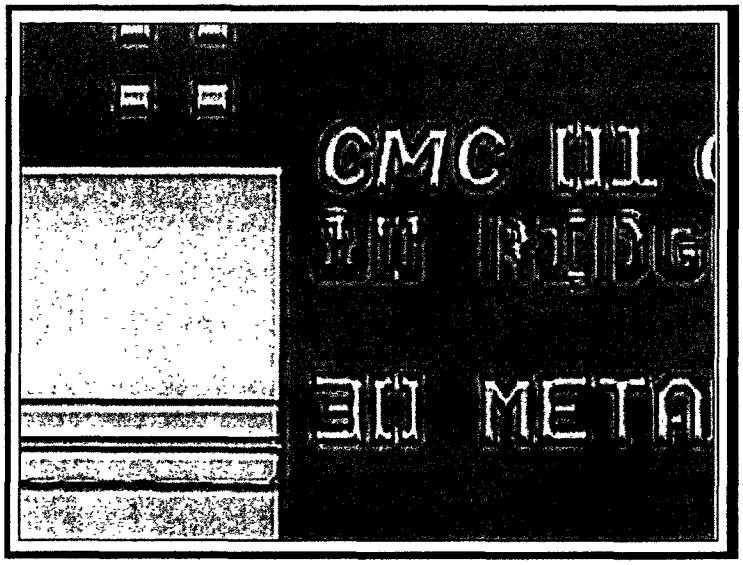

a

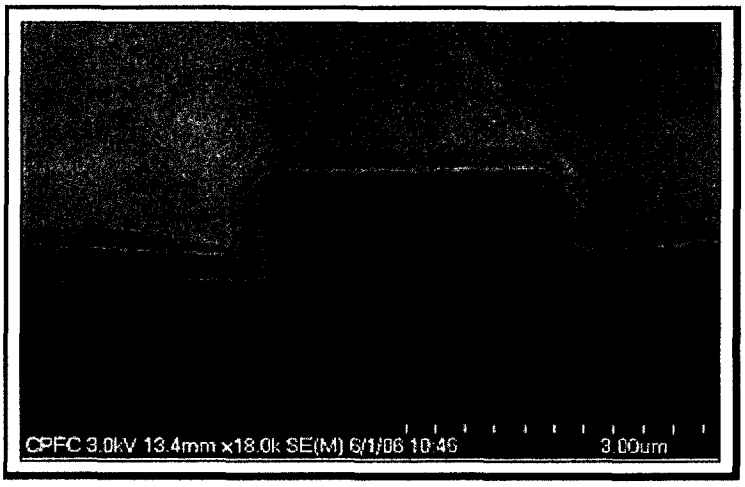

b

Figure 8-4 Fabricated EA modulators. a: top view; b: SEM of cross section

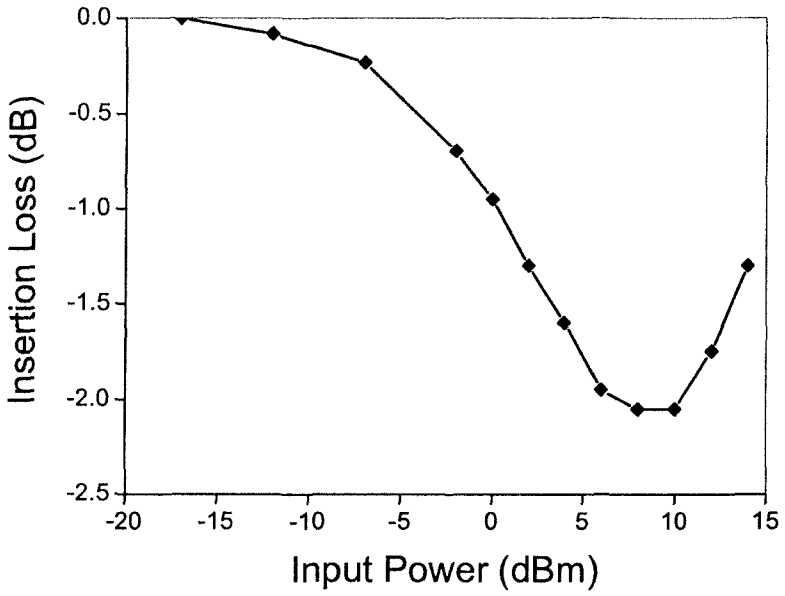

Figure 8-5 Optical absorption saturation characteristics of EA modulator

The fabricated EA modulators have been characterized by Prof. Cartledge's group in Queen's University. The basic measurements such as current versus voltage and absorption versus wavelength have been done to confirm that the devices work as EA modulators are supposed to. Here we are most interested in the characteristics of optical absorption saturation. Figure 8-5 shows the insertion loss (normalized to the insertion loss at low input power) at a wavelength of 1610nm. The device is inversely biased at -0.75V. And the measured die is coated and 300um long. We can see a relative absorption saturation of 2.0 dB around input power of 8.0 dBm. When the input power

exceeds 10.0 dBm, the saturation reduced again. This is attributed thermal effects at high optical power. The power level for the EAM to saturate is higher than the design targets. We also note that the excitonic peak is around 1610nm instead of the design value of 1550nm, which indicates that the basic parameters of the quantum well structure (either the composition or well width or both) have shifted from the design values.

The reasons the device does not work as designed are many fold. As any development of this nature, many runs often have to been attempted before a workable device can be made. In addition, the project is a pilot of CFPC that is intented to give more fabrication access to Canadian university researchers. There are still many aspects to be developed and improved from a project management point of view. For instance, better data tracking and thus better problem diagnosis is desired. Nonetheless, the effort of EAM prototyping is worth attempting. We believe, through more tries and as conditions improve, the effort will eventfully come to fruition in future.

Chapter 9

Conclusions and Suggestions for Future Work

9.1 Summary and Conclusions

In this thesis, we have systematically studied the subject of nonlinear EA modulators, including the development of probably the most comprehensive model for the device, the investigation of some fundamental physics relevant to EAM in nonlinear applications, and the exploration and experimentation of innovative design concepts. The major contributions of the thesis are summarized as follows and the corresponding publications can be found in Appendix B.

Firstly, on the model

1. A physics-based and self-consistent model has been developed for optical absorption saturation in quantum-well electroabsorption modulators, including both exciton saturation and electric field screening [17]. And we have shown that the comprehensive model is indispensable in the study of

EA modulators for high-speed nonlinear applications such as optical wavelength conversion and signal regeneration in optical networks.

2. The numerical boundary condition of the perfectly matched layer (PML) terminated by an infinite potential barrier has been applied to the state analysis of quantum-wells with tilted potentials [20]. The boundary condition extends the electron state analysis to the cases of shallow quantum wells and strong electrical field.

Secondly, on the physics

1. We have studied the effects of exciton state mixing on photo-induced conduction inter-subband transitions in un-doped quantum wells [18]. We have shown that an infrared laser near resonant with two conduction subbands in quantum wells can in fact excite intersubband excitations not only with zero orbital angular momentum attributions but also with other orbital angular momentum attributions (p, d, ...). Our results show that the inclusion of all the orbital angular momentum allows accurate evaluation of the dipole moment of the photo-induced intersubband transitions, which may have been drastically overestimated or underestimated by the previous models.
2. We have studied the excitonic nature of carrier capture and escape in shallow quantum wells including the effects of valence subband mixing

[19]. We show that such a mixing process has significant impact, yielding one order of magnitude smaller capture and escape times than the previous results.

Finally, on the design

1. The dynamic behaviors of electrons and holes under a strong optical pulse excitation have been investigated for two different quantum well systems: $In_{0.53}Ga_{0.47}As$ / $In_{1-x}Ga_xAs_yP_{1-y}$ and $In_{0.53}Ga_{0.47}As$ / $In_{1-x-y}Ga_xAl_yAs$ quantum wells [17]. For $In_{0.53}Ga_{0.47}As/In_{1-x}Ga_xAs_yP_{1-y}$ quantum wells, it is found that the slow hole sweep-out time in a QW impedes the device speed by causing a long tail and that larger hole concentrations in QWs harms to achieve large absorption changes. In contrast, for $In_{0.53}Ga_{0\,47}As$ $/In_{1-x-y}Ga_xAl_yAs$ quantum wells, the electron and hole saturation dynamics are more balanced, and more electron concentration in QW helps to enhance absorption changes. As a result, absorption saturation as 2 times as large as that of $In_{0.53}Ga_{0.47}As$ / $In_{1-x}Ga_xAs_yP_{1-y}$ quantum wells can be achieved under comparable device speed.
2. TE/TM insensitive operations of EA modulators have been analyzed and realized in tensile strained QW structures for application in optical

communication [24]. The effects of valance band mixing and exciton state mixing have been taken fully into account.

3. The excitonic excitation of light-holes by TM modes, instead of the conventional excitation of heavy-holes through TE mode has been utilized to enhance exciton saturation [24], which yields much lower optical power consumption for EAM.

9.2 Suggestions for Future Research

Based on the work presented in this thesis, some suggestions for future research can be made as follows:

9.2.1 2D model of EAM

Most of the device physics, such as quantum confinement and carrier transport happen along the growth direction. So that be the focus of the models developed in this thesis. Nevertheless, to completely describe the EA modulator, optical wave propagation along the longitudinal direction is needed. Two-dimensional models are desirable to connect the terminal characteristics of the EAM to the device parameters. This is important especially in the study of the device performance in optical systems.

9.2.2 Behavior models of EAM

The device models developed in this thesis are rich in physics. If we can leverage the work done here to extract the behavior models for EAM, they will be very useful for optical system applications [89].

9.2.3 Electron/exciton tunneling

The theoretical platform built in this thesis can also be used to investigate electron/exciton tunneling from quantum wells. Tunneling is an important mechanism for electrons/excitons to escape out of quantum wells. The current tunneling model is based on parabolic band structure of electrons and holes. PML boundary conditions implemented in Chapter 3 for parabolic band structures can be extended to the case of valence band mixing, which enables us to study the effects of valence band mixing and exciton state mixing on the tunneling.

9.2.4 Innovative design and experimental prototyping

It is desirable to have the experimental condition to work through the design concepts developed in the thesis. On the theoretical simulation and optimization side, more structures such as asymmetric quantum wells, coupled quantum wells, SCH with various profiles can be explored for the applications of optical wavelength conversion and signal regeneration [3],[83].

Bibliography

[1] R. Dingle, W. Wiegmann, and C. H. Herry, "Quantum states of confined carriers in very thin AlGaAs/GaAs/AlGaAs heterostructures," *Phys. Rev. Lett.* **33**, pp.827-830, 1974.

[2] H. Yu, J. B. Li, R. A. Loomis, L-W. Wang and W. E. Buhro, "Two-versus three-dimensional quantum confinement in indium phosphide wires and dots," Nature Material, **2**, 517, 2003

[3] N. El Dahdah et al. "New Design of InGaAs–InGaAlAs MQW Electroabsorption Modulator for High-Speed All-Optical Wavelength Conversion," *IEEE Photo. Tech. Lett.*, vol. 16, No. 10, pp. 2302-2304, Oct, 2004.

[4] S. Højfeldt, F. Romstad, and J. Mørk, "Absorption Recovery in Strongly Saturated Quantum-Well Electroabsorption Modulators" *IEEE Photo. Tech. Lett.*, vol. 15, No. 5, pp. 676-678, May, 2003.

[5] T. H. Wood, "Multiple quantum well waveguide modulator," *J. Light-wave Technol.*, vol. 6, No. 6, pp. 743-757, June, 1988.

[6] N. El Dahdah et al., "All-Optical Wavelength Conversion by EAM with Shifted Bandpass Filter for High Bit-Rate Network," *IEEE Photo. Tech. Lett.*, vol. 18, No. 1, pp. 61-63, Jan., 2006.

[7] M. Daikoku, N. Yoshikane, T. Otani, and H. Tanaka, "Optical 40 Gbit/s 3R regenerator with a combination of the SPM and XAM Effects for All-Optical networks," *J. Lightwave Technol.,* vol. 24, N0. 3, pp. 1142–1148, March. 2006.

[8] A. Labrousse, B. Dagens, R. Brenot, B. Lavigne, S. Squedin, B. Martin, S. Fabre, M. L. Nielsen, and M. Renaud, "Standard mode 40 Gb/s performance analysis of evanescent coupling 'active-passive' Mach–Zehnder interferometers for all-optical regeneration," *Electron. Lett.*, vol. 39, pp.1201–1202, 2003.

[9] J. Yu, X. Zheng, C. Peucheret, A. T. Clausen, H. N. Poulsen, and P. Pallen, "All-optical wavelength conversion of short pulses and NRZ signals based on a nonlinear optical loop mirror," *J. Lightw. Technol.*, vol.18, no. 6, pp. 1007–1017, Jun. 2000.

[10] S. Schmitt-Rink, D. S. Chemla, and D. A. B. Miller, "Theory of transient excitonic optical nonlinearities in semiconductor quantum-well structures," *Phys. Rev. B*, vol. 32, pp. 6601–6609, November, 1985.

[11] S. Schmitt-Rink, D. S. Chemla, and D. A. B. Miller, "Linear and nonlinear optical properties of semiconductor quantum wells," *Advances in Physics*, vol. 38, pp. 89–188, 1989.

[12] A. M. Fox, D. A. B. Miller, G. Livescu, J. E. Cunningham, and W. Y. Jan, "Quantum well carrier sweep out: Relation to electroabsorption and

excitonic saturation," *IEEE J. Quantum Electron.*, vol. 27, pp. 2281–2295, Oct. 1991.

[13] T. Sizer, II, T. K. Woodward, U. Keller, K. Sauer, T.-H. Chiu, D. L. Sivco, and A. Y. Cho, "Measurement of carrier escape rates, exciton saturation intensity, and saturation density in electrically biased multiple-quantum-well modulators," *IEEE J. Quantum Electron.*, vol. 30, pp. 399–407, Feb. 1994.

[14] T. H. Wood et al. "Electric field screening by photogenerated holes in multiple quantum wells: a new mechanism for absorption saturation," *Appl. Phys. Lett.,*, vol. 57, pp. 1081-1083, Sept. 1990.

[15] S. Hojfeldt, and J. Mork, "Modeling of Carrier Dynamics in Quantum-Well Elecrtoabsorption Modulators," *IEEE J. Selected Topics of Quantum Electron..*, vol. 8, pp. 1265–1276, Nov./Dec., 2002.

[16] J. A. Cavailles, D. A. B. Miller, J. E. Cunningham, P. L. K. Wa, and A. Miller, "Simultaneous measurement of electron and hole sweep-out from quantum well and modeling of photoinduced field screening dynamics," *IEEE J. Quantum Electron.*, vol. 28, pp. 2486–2497, Oct. 1992.

[17] Y. Chen and W. P. Huang, "Modeling and design of electroabsorption modulators: high speed and high nonlinearity," submitted to *IEEE J. Quantum Electron.*

[18] Y. Chen, S. M. Sadeghi, and W. P. Huang, "Exciton state mixing effects in photo-induced intersubband transitions in quantum well structures," *Phys. Rev. B*, vol. 75, 233409, June, 2007.

[19] Y. Chen, S. M. Sadeghi, and W. P. Huang, "Valence band mixing effects in the exciton capture and escape in quantum well structures," *J. Appl. Phys.* Vol. 102, 093716, November, 2007

[20] Y. Chen and W. P. Huang "Quasi bound states and electro-absorption in tilted quantum wells", SPIE Proceeding, Vol. 5971, 59711A, Oct, Toronto, 2005.

[21] C. Y. P. Chao and S. L. Chuang, "Analytic and numerical solutions for a two-dimensional exciton in momentum space," *Phys. Rev. B*, vol. 43, pp. 6530-6543, 1991.

[22] C. Y. P. Chao and S. L. Chuang, "Momentum-space solution of exciton excited states and heavy-hole-light-hole mixing in quantum wells," *Phys. Rev. B*, vol. 48, pp. 8210-8221, 1993.

[23] Z. M. Li, S. P. McAlister and C. M. Hurd, "Use of Fermi statistics in two-dimensional numerical simulation of heterojunction devices," *Semicond. Sci. Tech.*, vol. 5, p.408, 1990.

[24] Y. Chen, S. M. Sadeghi, and W. P. Huang, "High saturation design of electro-absorption devices," *Proceedings of Integrated Photonics Research and Applications* (IPRA2006), ITuE5, Uncasville, Connecticut, USA.

[25] Y. Chen and W. P. Huang, "Modeling and design of polarization insensitive electro-absorption modulators," to be submitted to *J. Appl. Phys.*

[26] O. Madelung, "Introduction to Solid-State Theory", Springer, 1996.

[27] S. Selberherr, "Analysis and simulation of semiconductor devices", New York, Springer-Verlag, 1984.

[28] J. Singh, "Electronic and optoelectronic properties of semiconductor structures", Cambridge University Press, 2003.

[29] J. M. Luttinger and W. Kohn, "Motion of electrons and holes in perturbed periodic fields," *Phys. Rev.* 97, pp. 869-883, 1955.

[30] S. L. Chuang, "Efficient band-structure calculations of strained quantum wells using a two-by-two Hamiltonian," *Phys. Rev. B,* vol. 43, pp. 9649-9661, 1991.

[31] C. Y. P. Chao and S. L. Chuang, "Spin-orbit-coupling effects on band-structure of strained semiconductor quantum wells," *Phys. Rev. B,* vol. 46, pp. 4110-4122, 1992.

[32] G. Bastard, E. E. Mendez, L. L. Chang, and L. Esaki, "Variational calculations on a quantum well in an electric field," *Phys. Rev. B,* vol. 28, pp. 3241-3245, 1983.

[33] S. L. Chuang, S. Schmitt-Rink, D. A. B. Miller, and D. S. Chemla, "Exciton's Green's-function approach to optical absorption in quantum well with applied electric field," *Phys. Rev. B,* vol. 43, pp. 1500-1509, 1991.

[34] N. Tessler and G. Eisenstein, "On carrier injection and gain dynamics in quantum well lasers," *IEEE J. Quantum Electron.*, vol. 29, pp. 1586–1595, June. 1993.

[35] M. Grupen and K. Hess, "Simulation of carrier transport and nonlinearities in quantum-well laser diodes," *IEEE J. Quantum Electron.*, vol. 34, pp. 120–140, Jan. 1998.

[36] Z. M. Li, K. M. Dzurko, A. Delage, and S. P. McAlister, "A self-consistent two-dimensional model of a GRIN-SCH structures," *IEEE J. Quantum Electron.*, vol. 28, pp. 792-803, April, 1992.

[37] H. Schneider and K. von Klitzing, "Thermionic emission and Gaussian transport of holes in a GaAs/Al Ga As multiple-quantum-well structure," *Phys. Rev. B*, vol. 38, no. 9, pp. 6160–6165, 1988.

[38] C. Y. Tsai, L. F. Eastman Y. H. Lo, and C-Y. Tsai, "Breakdown of thermionic emission theory for quantum wells," *Appl. Phys. Lett..*, vol. 65, No. 4, pp. 469-471, July, 1994.

[39] K. W. Goossen, L. M. F. Chirovsky, R. A. Morgan, J. E. Cunningham, and W. Y. Jan, "High-Power Extremely Shallow Quantum-Well Modulators," *IEEE Photo. Tech. Lett..*, vol. 3, No. 5, pp. 448-450, May, 1991.

[40] A. K. Ghatak, I. C. Goyal, and R. L. Gallawa, "Mean lifetime calculations of quantum well structures: A rigorous analysis," *IEEE J. Quantum Electron.*, vol. 26, pp. 305–310, Feb. 1990.

[41] P. Debernardi, and P. Fasano, "Quantum Confined Stark Effect in Semiconductor Quantum Wells Including Valence Band Mixing and Coulomb Effects," *IEEE J. Quantum Electron.*, vol. 29, pp. 2741-2755, Nov. 1993.

[42] E. Anemogiannis , E. N. Glytsis ,and T. K. Gaylord, "Quasi-Bound States Determination Using a Perturbed Wavenumbers Method in a Large Quantum Box", *IEEE J. Quantum Electron.*, vol. 33, pp. 742–752, May. 1997.

[43] T. Yamanaka, K. Wakita, and K. Yokoyama, "Field-induced broadening of optical absorption in InP-based quantum wells with strong and weak quantum confinement," *Appl. Phys. Lett.,* vol. 65, pp. 1540-1542, 1994.

[44] T. Ikeda and H. Ishikawa, "Analysis of the Attenuation Ratio of MQW Optical Intensity Modulator for 1.55 pm Wavelength Taking Account of Electron Wave Function Leakage," *IEEE J. Quantum Electron.*, vol. 32, No. 10, pp. 284-292, Feb., 1996.

[45] W. L. Bloss "Electric field dependence of quantum well eigen states," *J. Appl. Phys.* , vol. 65, pp. 4789-4794, June, 1989.

[46] K. Nakamura, A. Shimizu, M. Koshiba, and K. Hayata, "Finite–elements analysis of quantum wells of arbitrary semiconductors with arbitrary potential profiles," *IEEE J. Quantum Electron.*, vol. 25, pp. 889–895, May 1989.

[47] A. W. Snyder and J. D. Love, *Optical Waveguide Theory.* London, Capman and Hall, 1983.

[48] S. L. Lee, Y. C. Chung, L. A. Coldren and N. Dagli, "On leaky mode approximation for mode expansion in multilayer open waveguide," *IEEE J. Quantum Electron.*, vol. 31, No. 10, pp. 1790-1802, Oct., 1995.

[49] J. P. Berenger, "A perfectly matched layer for the absorption of electromagnetic waves," *J. Computational Phys.*, vol. 114, pp. 185–200, 1994.

[50] W. P. Huang, C. L. Xu, W. Lui, and K. Yokoyama "The perfect matched Layer Boundary Condition for the beam propagation method ," *IEEE Photon. Tech. Let.* , vol. 8, pp. 649-651, May. 1996.

[51] W. P. Huang, C. L. Xu, W. Lui, and K. Yokoyama "The perfect matched Layer Boundary Condition for Modal Analysis of Optical Waveguide: Leaky Mode Calculations," *IEEE Photon. Tech. Let.* , vol. 8, pp. 652-654, May. 1996.

[52] A. Ahland, D. Schulz, and E. Voges, "Accurate mesh truncation for Schrödinger equations by a perfectly matched layer absorber: Application to the calculation of optical spectra," *Phys. Rev. B,* vol. 60, no. 8, pp. R5109–5112, 1999.

[53] H. Derudder, F. Olyslager, D. De Zutter and Van De Berghe, "Efficient Mode-Matching Analysis of Discontinuities in Finite Planar Substrates

Using Perfectly Matched Layers," *IEEE Trans. Antennas and Propagation*, vol. 49, No. 2, pp. 185–195, Feb, 2001.

[54] S.L. Chuang, "Physics of optoelectronic devices", John Wiley and Sons, Inc., New York, 1995.

[55] D. A. B. Miller, D. S. Chemla, T. C. Damen, A. C. Gossard, W. Wiegmann, T. H. Wood, and C. A. Burrus, "*Electric field dependence of optical absorption near the bandgap of quantum well structures*", *Phys. Rev. B,* Vol. 32, pp. 1043-1060, 1985

[56] D. J. Binks "Quasi-Bound State Theory of Field-Dependent Photogeneration From Polymer-Embedded Nanoparticles," *IEEE J. Quantum Electron.*, vol. 40, No. 8, pp. 1140-1149, Aug., 2004.

[57] A. Neogi, H. Yoshida, T. Mozume, and O. Wada, "Enhancement of interband optical nonlinearity by manipulation of intersubband transitions in an undoped semiconductor quantum well," *Opt. Commun.*, 159, p.225,1999

[58] M. Olszakier, E. Ehrenfreund, E. Cohen, J. Bajaj, and G.J. Sullivan, "Photoinduced intersubband absorption in undoped multi-quantum-well structures," *Phys. Rev. Lett.* **62**, p.2997, 1989.

[59] S. M. Sadeghi and W. Li, "Hole Mixing and Strain Effects in the Conduction Intersubband Transitions of Undoped Quantum Wells," IEEE J. Quantum Electron. **40**, 343 (2004).

[60] S. M. Sadeghi and W. Li, "Excitonic effects in the photo-induced conduction intersubband transitions in un-doped quantum wells," Phys. Rev. B **70**, 195321 (2004)

[61] B. Zhu and K. Huang, "Effect of valence-band hybridization on exciton spectra in GaAs-GaAlAs quantum wells," Phys. Rev. B **36**, 8102 (1987).

[62] Jian-Bai Xia "Electronic structures of zero-dimensional quantum wells," Phys. Rev. B **40**, 8500 (1989)

[63] L. C. Andreani and A. Pasquarello, "Accurate theory of excitons in GaAs-GaAlAs quantum wells," Phys. Rev. B **42**, 8928 (1990).

[64] S. Noda, M. Ohya, T. Sakamoto, and A. Sasaki, "Interband-resonant light modulation by intersubband-resonant light in undoped quantum wells," IEEE J. Quantum Electron. **32**, 448 (1996).

[65] H. Schmidt and R. J. Ram, "All-optical wavelength converter and switch based on electromagnetically induced transparency," Appl. Phys. Lett. **76**, 3173 (2000)

[66] C. Gmachl, F. Capasso, D. L. Sivco, and A. Y. Cho, "Recent progress in quantum cascade lasers and applications," Rep. Prog. Phys. **64**, 1533, 2001.

[67] F. H. Julien, P. Vagos, J.-M. Lourtioz, D. Yang, and R. Planel, "Novel all-optical 10 μm waveguide modulator based on intersubband absorption in GaAs/AlGaAs quantum wells," Appl. Phys. Lett. **59**, 2645, 1991.

[68] B. F. Levine, "Quantum-well infrared photo-detectors," J. Appl. Phys. **74** R1(1993)

[69] S. M. Sadeghi, S. R. Leffler, and J. Meyer, "Quantum interference and nonlinear optical processes in the conduction bands of infrared-coupled quantum wells," Phys. Rev. B **59**, 15388 (1999)

[70] M. D. Frogley, J.F. Dynes, M. Beck, J. Faist and C.C. Phillips, "Gain-Without-Inversion in Semiconductor Nanostructures," Nature Material, **5**, 175 (2006)

[71] V. A. Fonoberov, E. P. Pokatilov, V. M. Fomin, and J. T. Devreese, "Photoluminescence of Tetrahedral Quantum-Dot Quantum Wells," Phys. Rev. Lett., **92** 127402 (2004)

[72] V. I. Klimov, "Mechanisms for Photogeneration and Recombination of Multiexcitons in Semiconductor Nanocrystals: Implications for Lasing and Solar Energy Conversion," J. Phys. Chem. B **110**, 16827(2006)

[73] N. Tansu and L. J. Mawst, "Current injection efficiency of InGaAsN quantum-well lasers," *J. Appl. Phys.* **97**, 054502, (2005).

[74] M. Mazzer et al. "Progress in quantum well solar cells," *Thin Solid Films*, **511**, 76, (2006)

[75] J. A. Brum and G. Bastard, "Resonant carrier capture by semiconductor quantum wells," *Phys. Rev. B*, **33**, 1420, (1986).

[76] O. Heller and G. Bastard, "Exciton capture by shallow quantum wells in separate confinement hetero-structures," *Phys. Rev. B*, **54**, 5629, (1996-II).

[77] R. Spiegel, G. Bacher, K. Herz, A. Forchel, T. Litz, A. Waag, and G. Landwehr, "Recombination and thermal emission of excitons in shallow CdTe/$Cd_{1-x}Mg_xTe$ quantum wells," *Phys. Rev. B*, **53**, 4544, 1996-II.

[78] Ph. Roussignol, J. Tignon, and G. Bastard, "Consequences of thermalization on the photoluminescence dynamics of shallow quantum well heterostructures," *J. Lumin.* **92**, pp.43-56, 2001.

[79] J. Feldmann, K.W. Goossen, D.A.B. Miller, A.M. Fox, J.E. Cunnigham, and W.Y. Jan, "Fast escape of photocreated carriers out of shallow quantum wells," *Appl. Phys. Lett.* **59**, 66, 1991.

[80] I.-K. Oh, J. Singh, A.Thilagam, and A. S. Vengurlekar, "Exciton formation assisted by LO phonons in quantum wells," *Phys. Rev. B*, **62**, 2045, 2000-I.

[81] S. W. Koch, M. Kira, G. Khitrova, and H. M. Gibbs, "Semiconductor excitons in new light," *Nature Material*, **5**, 523, 2006.

[82] A. Siarkos, E. Runge, and R. Zimmermann, "Center-of-mass properties of the exciton in quantum wells," Phys. Rev. B, **61**, 10854, 2000-II.

[83] M. Hayashi, H. Tanaka, K. Ohara, T. Otani, and M. Suzuki, "OTDM transmitter using WDM–TDM conversion with an electroabsorption wavelength converter," *J. Lightwave Technol.*, vol. 20, N0. 2, pp.236–242, Feb., 2002.

[84] H. V. Demir, V. A. Sabnis, O. Fidaner, J. S. Harris, Jr., and D. A. B. Miller and J-F. Zheng, "Dual-diode quantum-well modulator for C-band wavelength conversion and broadcasting," *Optics Express*, Vol.12, pp. 310-316, Jan. 2004.

[85] K-H. Chung and J-I. Shim, "A New Polarization-Insensitive 1.55-um InGaAs(P)–InGaAsP Multiquantum-Well Electroabsorption Modulator Using a Strain-Compensating Layer," *IEEE J. Quantum Electron.*, vol. 35, No. 5, pp. 730-736, May, 1999.

[86] S. Chelles, R. Ferreira and P. Volsin, "On the design of polarization-insensitive optoelectronic devices," *Semicond. Sci. Technol.*, vol. 10, pp. 105-109, 1995

[87] G. D. Sanders and Y-C. Chang, "Effects of band hybridization on exciton states in GaAs/GaAlAs quantum wells," *Phys. Rev. B*, **32**, 5517, 1985.

[88] R. Mottahedeh et al. "Carrier lifetime and exciton saturation in a strain-balanced InGaAs/InAsP multiple quantum well," *J. Appl. Phys.*, vol. 83, pp. 306-309, Jan., 1998.

[89] N. Cheng and J. C. Cartledge, "Measurement-based model for cross-absorption modulation in an MQW electroabsorption modulator," *J. Lightwave Technol.*, vol. 22, N0. 7, pp.1805–1810, July. 2004.

Appendix A

Excitonic Absorption in Quantum Wells

The general formulation of optical absorption can be obtained by the theory of electron-photon interaction as [54]

$$\alpha(\hbar\omega) = C_0 \frac{2}{V} \sum_{i,f} \left| \langle f | e^{i\mathbf{k}_0 \cdot \mathbf{r}} \hat{\mathbf{e}} \cdot \mathbf{p} | i \rangle \right|^2 \delta(E_f - E_i - \hbar\omega)[f(E_i) - f(E_f)] \qquad \text{(A.1)}$$

Where C_0 is constant. $|i\rangle$ and $|f\rangle$ are the initial state and the final state with corresponding energy E_i and E_f, respectively. $f(E)$ is Fermi distribution function.

The key in equation (A.1) is the matrix element $\langle f | \hat{O} | i \rangle$. To evaluate the matrix elements, we first need to have the wave functions of initial and final states, which lead us to the discussion of wave functions of two-particle system. The wave function of two-particle system consisted of an electron and a hole $\psi(\mathbf{r}_e, \mathbf{r}_h)$ can be expressed as a linear composition of single (uncorrelated) electron and hole Bloch functions $\psi_{c\mathbf{k}_e}(\mathbf{r}_e)$ and $\psi_{v-\mathbf{k}_h}(\mathbf{r}_h)$ as

$$\psi(\mathbf{r}_e, \mathbf{r}_h) = \sum_{\mathbf{k}_e, \mathbf{k}_h} A(\mathbf{k}_e, \mathbf{k}_h) \psi_{c\mathbf{k}_e}(\mathbf{r}_e) \psi_{v-\mathbf{k}_h}(\mathbf{r}_h) \qquad \text{(A.2)}$$

The great simplification can be achieved in semiconductor theory by invoking the effective mass approximation, in which he fast-varying Bloch periodic functions

$u_c(\mathbf{r}_e)$ and $u_v(\mathbf{r}_h)$ can be dropped from the basis function and be incorporated into effective masses. This allows us to focus on envelope function only. The envelope function two-particle can be expanded in terms of the envelope function of single electron as

$$\Phi(\mathbf{r}_e,\mathbf{r}_h)=\frac{1}{V}\sum_{\mathbf{k}_e,\mathbf{k}_h}A(\mathbf{k}_e,\mathbf{k}_h)e^{i\mathbf{k}_e\cdot\mathbf{r}_e}e^{i\mathbf{k}_h\cdot\mathbf{r}_h} \tag{A.3}$$

Since Coulomb potential between electrons and holes depends only on the difference between the electron and hole position vectors $V(\mathbf{r}_e,\mathbf{r}_h)=V(\mathbf{r}_e-\mathbf{r}_h)$, we can change coordinate system into the difference and center-of-mass system. Define the new coordinates in real space as

$$\mathbf{r}=\mathbf{r}_e-\mathbf{r}_h,\qquad \mathbf{R}=\beta\mathbf{r}_e+(1-\beta)\mathbf{r}_h \tag{A.4}$$

Or in momentum space as

$$\mathbf{k}=(1-\beta)\mathbf{k}_e-\beta\mathbf{k}_h,\qquad \mathbf{K}=\mathbf{k}_e+\mathbf{k}_h \tag{A.5}$$

For parabolic band structure, $\beta=m_e/(m_e+m_h)$.

The wave function of two-particle system can be expressed as

$$\Phi(\mathbf{r}_e,\mathbf{r}_h)=\Phi(\mathbf{R},\mathbf{r})=\frac{e^{i\mathbf{K}\cdot\mathbf{R}}}{\sqrt{V}}\phi(\mathbf{r})=\frac{e^{i\mathbf{K}\cdot\mathbf{R}}}{\sqrt{V}}\frac{1}{\sqrt{V}}\sum_{\mathbf{k}}a(\mathbf{k})e^{i\mathbf{k}\cdot\mathbf{r}} \tag{A.6}$$

And the optical matrix elements can be expressed as

$$\begin{aligned}\langle f|e^{i\mathbf{k}_0\cdot\mathbf{r}}\hat{\mathbf{e}}\cdot\mathbf{p}|i\rangle &= \sum_{\mathbf{k}_e,\mathbf{k}_h} A^*(\mathbf{k}_e,\mathbf{k}_h) < c,k_e\,|< v,-k_h\,|e^{i\mathbf{k}_0\cdot\mathbf{r}}\hat{\mathbf{e}}\cdot\mathbf{p}\,|\,v,k_h>|\,v,-k_h> \\ &= \sum_{\mathbf{k}_e,\mathbf{k}_h} A^*(\mathbf{k}_e,\mathbf{k}_h) < c,k_e\,|e^{i\mathbf{k}_0\cdot\mathbf{r}}\hat{\mathbf{e}}\cdot\mathbf{p}\,|\,v,k_h> \\ &= \sum_{\mathbf{k}} A^*(\mathbf{k},-\mathbf{k})\,\hat{\mathbf{e}}\cdot\mathbf{p}_{cv}(\mathbf{k})\end{aligned} \tag{A.7}$$

Here the final state is exciton state that is a wave packet in moment space and a localized distribution in real space. The initial state is plane wave states in moment space with equal distribution for all k. The following conditions have also been used in the above derivation. The optical vector potential operator change the symmetry of valence band Bloch functions, therefore the matrix element of p_{vv} is zero. In addition, the following selection rule has been used.

$$\mathbf{k}_e + \mathbf{k}_e = \mathbf{k}_{\text{photon}} \approx \mathbf{0} \tag{A.8}$$

Since the wavelength of photon is much longer than that of electron, the photon momentum has been considered as negligible.

Comparing equations (A.3) and (A.6), we obtain

$$\begin{aligned}&\sum_{\mathbf{k}} A^*(\mathbf{k},-\mathbf{k})\,\hat{\mathbf{e}}\cdot\mathbf{p}_{cv}(\mathbf{k}) \\ &= \hat{\mathbf{e}}\cdot\mathbf{p}_{cv}\sum_{\mathbf{k}} A^*(\mathbf{k},-\mathbf{k}) \\ &= \hat{\mathbf{e}}\cdot\mathbf{p}_{cv}\sum_{k} a^*(\mathbf{k}) = \hat{\mathbf{e}}\cdot\mathbf{p}_{cv}\sqrt{V}\phi^*(0)\end{aligned} \tag{A.9}$$

$\phi^*(0)$ is the wave function at the center which represents the probability to find

the electron and hole in the same cell. The formulation of exciton absorption in (A.9) can apply to exciton wave function obtained in real space (the last equation) and momentum space (the second last).

For the wave function in quantum wells, the envelop function of an electron-hole pair can be expressed as

$$\Phi(\mathbf{r}_e,\mathbf{r}_h)=\frac{e^{i\mathbf{K}_t\cdot\mathbf{R}_t}}{\sqrt{A}}F(\boldsymbol{\rho},z_e,z_h)=\sum_{\mathbf{k},nm}a_{nm}(\mathbf{k})\frac{1}{\sqrt{A}}e^{i\mathbf{k}\cdot\boldsymbol{\rho}}f_n(z_e)\sum_{\nu}g_{m,\nu}(z_h) \tag{A.10}$$

Where $f_n(z_e)$ and $g_{m,\nu}(z_h)$ are the one-dimensional electron and hole wave functions along the growth direction. Finally the excitonic absorption in quantum well can be written as

$$\begin{aligned}
&\langle f|e^{i\mathbf{k}_0\cdot\mathbf{r}}\hat{\mathbf{e}}\cdot\mathbf{p}|i\rangle=\sum_{nm}\sum_{\mathbf{k}_e,\mathbf{k}_h}A_{nm}^{*}(\mathbf{k}_e,\mathbf{k}_h)<c,n,k_e|<\nu,-k_h|e^{i\mathbf{k}_0\cdot\mathbf{r}}\hat{\mathbf{e}}\cdot\mathbf{p}|\nu,m,k_h>|\nu,-k_h>\\
&=\sum_{nm,\nu}\sum_{\mathbf{k}_e,\mathbf{k}_h}A_{nm}^{*}(\mathbf{k}_e,\mathbf{k}_h)<c,k_e|e^{i\mathbf{k}_0\cdot\mathbf{r}}\hat{\mathbf{e}}\cdot\mathbf{p}|\nu,k_h>I_{nm}^{\nu}\\
&=\sum_{nm}\sum_{\mathbf{k}}A_{nm}^{*}(\mathbf{k}_e,-\mathbf{k})\hat{\mathbf{e}}\cdot\mathbf{p}_{cv}(\mathbf{k})I_{nm}^{\nu}\\
&=\hat{\mathbf{e}}\cdot\mathbf{p}_{cv}\sum_{nm,\nu}[\sum_{\mathbf{k}}a_{nm}^{*}(\mathbf{k})]I_{nm}^{\nu}\\
&=\hat{\mathbf{e}}\cdot\mathbf{p}_{cv}\sum_{nm,\nu}\phi_{nm}^{*}(\boldsymbol{\rho}=0)I_{nm}^{\nu}
\end{aligned} \tag{A.11}$$

Appendix B

List of Publications

[1] Y. Chen and W. P. Huang "Quasi bound states and electroabsorption in tilted quantum wells", SPIE Proceeding, Vol. 5971, 59711A, Oct, Toronto, 2005.

[2] Y. Chen, S. M. Sadeghi, and W. P. Huang, "High saturation design of electro-absorption devices," *Proceedings of Integrated Photonics Research and Applications* (IPRA2006), ITuE5, Uncasville, Connecticut, USA.

[3] Y. Chen, S. M. Sadeghi, and W. P. Huang, "Exciton-state mixing effects in photo-induced intersubband transitions in quantum well structures," *Phys. Rev. B*, vol. 75, 233409, June, 2007.

[4] Y. Chen, S. M. Sadeghi, and W. P. Huang, "Valence band mixing effects in the exciton capture and escape in quantum well structures," *J. Appl. Phys.* vol. 102, 093716, November, 2007.

[5] Y. Chen and W. P. Huang, "Modeling and design of electroabsorption modulators: high speed and high nonlinearity," submitted to *IEEE J. Quantum Electron.*

[6] Y. Chen and W. P. Huang, "Modeling and design of polarization insensitive electro-absorption modulators," to be submitted to *J. Appl. Phys.*